NON-DEGENERATE TWO PHOTON GAIN IN BULK GALLIUM ARSENIDE

by

BRENDAN TURNBULL
B.S University of South Florida, 2011

A thesis submitted in partial fulfillment of the requirements
for the degree of Master of Science
in CREOL - College of Optics & Photonics
at the University of Central Florida
Orlando, FL

Spring Term
2013

Major Professors: Eric W. Van Stryland and David J. Hagan

ABSTRACT

The purpose of this thesis is to investigate the nonlinear phenomena known as doubly-stimulated, non-degenerate two-photon emission (ND-2PE) in Gallium Arsenide (GaAs). 2PE refers to the simultaneous emission of two-photons as electrons move from the conduction band in a direct gap semiconductor to the valence band. Following the same path for describing one-photon emission (1PE) we describe 2PE as a product of the irradiance, I, and the negative of the loss which in this case is two-photon absorption, α_2, the negative coming from the population inversion. We attempt to observe 2PE by using a frequency non-degenerate pump-probe experiment in which a third beam optically excites a 4 μm thick GaAs sample. We use non-degenerate beams in hopes of utilizing the 3-orders of magnitude enhancement seen in two-photon absorption (2PA) by going to extreme nondegeneracy (END) to enhance 2PE. GaAs is chosen due to the availability of the appropriate wavelengths, the maturity of the GaAs technology, its use in optoelectronic devices and its ability to be electrically pumped.

During the experimental development we learn how to effectively etch and manipulate thin GaAs samples and model the transmission spectrum of these samples using thin film transmission matrices. We are able to match the measured transmission spectrum with the theoretical transmission spectrum. Here we etch the bulk GaAs left on the sample leaving only the 4 μm thickness of molecular beam epitaxial grown GaAs plus additional layers of aluminum gallium arsenide (AlGaAs). These samples were grown for us by Professor Gregory Salamo of the University of Arkansas.

Using the pump-probe experiment on the 4 μm GaAs sample, we measure the change of the 2PA due to the presence of optically excited carriers. The goal is to reduce the 2PA signal to zero and then invert the 2PA signal indicating an increase in transmission indicative of 2PE when the population is inverted. Our results show that we achieve a 45% reduction in the 2PA signal in a 4 μm thick GaAs sample due to the excited carriers. Unfortunately, we currently cannot experimentally determine whether the reduction is strictly due to free-carrier absorption (FCA) of our pump or possibly due to a change in the two-photon absorption coefficient.

We measure the transmission of various wavelengths around the bang gap of GaAs as a function of excitation wavelength and achieve a transmittance of ~80% which we attribute to possibly be one photon gain (1PG) at 880 nm.

We also go to cryogenic temperatures to concentrate the carriers near the bottom of the conduction band and improve the theoretical gain coefficient for 2PE. Unfortunately, we do not observe a measurable change in 2PA with the addition of optically excited carriers.

Along with FCA of our infrared pump we suspect that the difficulties in this first set of experiments are also a result or radiative recombination due to amplified spontaneous emission reducing our free carrier density along with the fact that 4 μm is too thick for uniform excitation. We now have 1 μm samples from Professor Gregory Salamo which we hope will give better and more definitive results.

ACKNOWLEDGMENTS

I would first like to thank my professors Dr. Eric Van Stryland and Dr. David Hagan for giving me the opportunity to work with them and the guidance they provided through the course of these experiments.

I would like to thank Dr. Gregory Salamo for providing us with our GaAs samples.

I would like to thank the NLO group in no particular order, Honghua "Hu Daddy" Hu, Matt "Commander Riker" Reichert, Trenton "T-Dogg" Ensley, Davorin "The Hulk" Peceli and Manny "BD Wong" Ferdinandus, Himansu "Bromansu" Pattanaik, Matthias "Where's Matthias?" Muennich and Peng "Stop doing favors for Trenton" Zhao for all the help with this experiment and the good times we had. In particular I would like thank my cohort in this madness, Matt, who I am sure was, by the end, very sick of my questioning. Hopefully, the fall Woodchuck was worth it all.

I would like to thank my brothers, whether they like it or not, Ben Brekhus, Tarrell Cunningham, Zeke Bravo and Josh McCammey for being there over the course of these many years. I would also like to thank Liz Hulme for understanding that being with me through this would be boring for about two years.

Lastly, and perhaps most importantly I would like to thank my family. My mother for the constant encouragement and my father for understanding that sometimes I couldn't visit. I would like to thank Steven, Sarah, Brittany and Justin for being the best brothers and sisters I could ever ask for. In particular I would like to thank Justin for dealing with me for his entire life and not hating me too much.

TABLE OF CONTENTS

LIST OF FIGURES

LIST OF TABLES

LIST OF ACRONYMS/ABBREVIATIONS

2PA	Two-photon absorption
2PG	Two-photon gain
2PE	Two-photon emission
2PL	Two-photon laser
3PA	Three-Photon Absorption
AlGaAs	Aluminum gallium arsenide
ASE	Amplified Spontaneous Emission
BBO	(Beta-BaB_2O_4)
cm	centimeter ($= 10^{-2}$ m)
CPA	Chirped Pulse Amplification
cw	Continuous-wave
D-	Degenerate (equal energy)
Er^{3+}	Erbium Doped
ESA	Excited state Absorption
eV	Electron-volt ($\approx 1.602 \times 10^{-19}$ J)

FGR	Fermi's Golden Rule
fs	femtosecond ($= 10^{-15}$ s)
ft	foot
GaAs	Gallium arsenide
GVD	Group Velocity Dispersion
GW	gigawatt ($= 10^{9}$ W)
HH	Heavy Hole
Hz	hertz
IR	Infrared
K	Kelvin
kHz	kilohertz ($= 10^{3}$)
LH	Light Hole
MCT	Mercury Cadmium Telluride
µF	microfarad ($= 10^{-6}$ F)
µJ	microjoules ($= 10^{-6}$ J)
µm	micrometer, micron ($= 10^{-6}$ m)

μs	microseconds ($= 10^{-6}$ s)
mJ	millijoules ($= 10^{-3}$ J)
mL	milliliter
MΩ	megaohm ($= 10^{6}$ Ω)
mTorr	millitorr ($= 10^{-3}$ Torr ≈ 0.133 Pa)
mW	milliwatt ($= 10^{-3}$ W)
nA	nanoamp ($= 10^{-9}$ A)
ND-	Nondegenerate (unequal energy)
NLO	Nonlinear Optics
NLR	Nonlinear Refraction
nm	nanometer ($= 10^{-9}$ m)
nW	nanowatt ($= 10^{-9}$ W)
p-i-n	p-type, intrinsic, n-type
pA	picoamp ($= 10^{-12}$ A)
PC	Pockels Cell
pJ	picojoules ($= 10^{-12}$ J)

PPLN	Periodically Poled Lithium Niobate
pW	picowatt ($= 10^{-12}$ W)
s, p, d	Atomic subshells
SVEA	Slowly-Varying-Envelope-Approximation
Ti:Sapphire	Titanium doped Sapphire
UV	Ultraviolet
W	Watt
WLC	White Light Continuum
ZnO	Zinc oxide
ZnS	Zinc Selenide

CHAPTER 1: INTRODUCTION

1.1 Research Motivation

Early in the 1930's Maria Göppert-Mayer [1] laid the foundation of multi-photon processes through her research in both the simultaneous absorption and emission of two energy quanta by an electron. The simultaneous absorption of two energy quanta has become known as two-photon absorption (2PA). The inverse process of 2PA is known as two-photon emission (2PE), where an electron concurrently loses energy through an emission of two-photons. 2PE, while similar to that of single photon emission in terms of the stimulated photons having the same properties as the stimulating photons, has some innate differences. Perhaps the most major of these differences is that the energy quanta released in a 2PE process can contain any sum of two energies equal to the transition energy, i.e. $\hbar\omega_a + \hbar\omega_b = \hbar\omega_0$. There are several types of 2PE processes; spontaneous 2PE, singly-stimulated 2PE and doubly-stimulated 2PE. Spontaneous 2PE is the spontaneous emission of two-photons. Singly-stimulated 2PE occurs when a photon of energy less than the energy of the transition stimulates a photon of the same energy while spontaneously emitting a photon with complimentary energy such that the sum is equal to the transition energy. Doubly-stimulated 2PE is where two-photons with an energy sum equal to the transition energy, but each with energy less than the transition, stimulate the emission of a pair of photons, each with the characteristics of the stimulating photon,. Figure 1 shows a diagram of each of these processes.

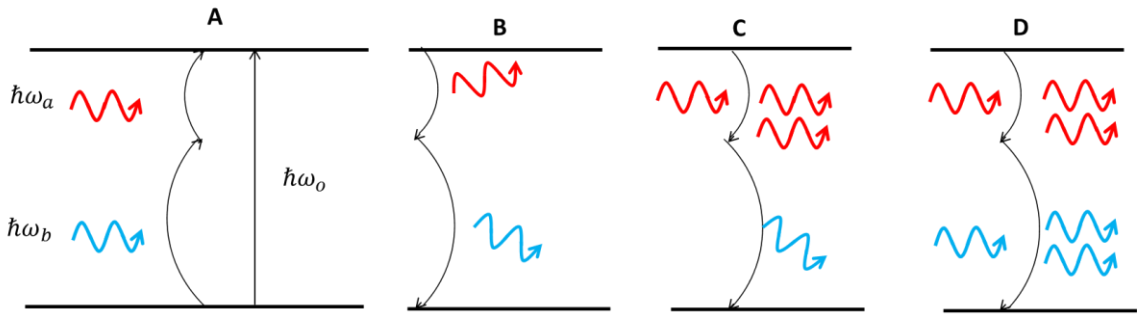

Figure 1- 2PA (A), Spontaneous 2PE (B), singly- stimulated 2PE (C), doubly-stimulated 2PE (D)

Consequently, 2PE can release an entire spectrum of frequencies so long as each individual frequency is less than ω_0 and the sum is equivalent to ω_0, i.e. the process allows for tunability [2, 3]. If the frequencies of the photons in the multi-photon process are the same, i.e. $\omega_a = \omega_b$, it is referred to as a degenerate photon process. However, if the frequencies are different, $\omega_a \neq \omega_b$, the process is referred to as a non-degenerate photon process.

Multi-photon processes have been of interest in the research community particularly for optical switching [4], optical limiting [5] and frequency conversion [6, 7]. 2PE became of interest in 1940s when Breit and Teller [8] theorized that the lifetime of the metastable 2s state of hydrogen was dominated by the spontaneous 2PE process. This was important at the time for explaining the spectrum of nebulae that were comprised mostly of hydrogen. Like most other nonlinear phenomena, 2PE could not be reproduced until the advent of the laser in 1960 [9]. After the development of the one photon laser in the 1960's, Sorokin and Braslau [10] and Prokhorov [2] both suggested the development of a two-photon laser (2PL). Currently, the 2PE process is under investigation to create a solid state two-photon gain (2PG) amplifier and eventually a solid state 2PL. Previous research has shown that the 2PG amplifier would demonstrate a variety of traits

including pulse compression [11, 12], entangled photons [13] and the requirement of an injection signal to initiate lasing [10, 14] all as a result of the nonlinearity of the 2PE process.

Up until recently, most of the work in creating a two-photon amplifier and two-photon laser has utilized metastable hydrogen and helium energy states [15, 16] and dressed state gases including barium [14] and potassium [17]. Recently, however, there has been a significant push to use semiconductors as a 2PG media, one in particular, Gallium Arsenide (GaAs) [18]. GaAs's large inherent nonlinear properties, the maturity of the GaAs technology, use in optoelectronic devices and the ability to be electrically pumped are some of the particular reasons why GaAs was chosen for this experiment. The intention of this work is to observe non-degenerate, doubly-stimulated 2PE in bulk GaAs. The method of observation is a three beam pump-probe experiment discussed in Chapter 3. Experimental results including single photon gain and two-photon gain in GaAs are discussed in Chapter 4; conclusions and future work are discussed in Chapter 5.

1.2 History

Maria Göppert-Mayer [1] developed the theory for 2PE when she constructed her theory on mulitphoton transitions. Not long after this 2PE was considered by Breit and Teller [8] as the explanation for the emission spectrum of nebulae. They conjectured that the metastable 2s state of hydrogen was dominated by the 2PE process which would lead to a peak in the emission spectrum over the range of 390-480 nm [19]. Since then spontaneous, singly-stimulated and doubly-stimulated two-photon emission processes have been observed. In 1968 Yatsiv, Rokni and Barak observed singly-stimulated 2PE between the 6s to 4s states of Potassium [17]. The

electrons were excited to the 6s state through 2PA using a ruby laser and stimulated Raman emission from nitrobenzene. 2PE was induced by subjecting the potassium vapor to Raman scattered radiation from a Ruby laser of a frequency close to that of the transition from 6s to $4s_{3/2}$, radiation of the stimulating frequency was subsequently emitted, ω_a, along with radiation of the complimentary frequency, ω_b, such that $\omega_b = \omega_0 - \omega_a$ where ω_0 is the frequency of the transition from 4s to 6s. Figure 2a depicts this system.

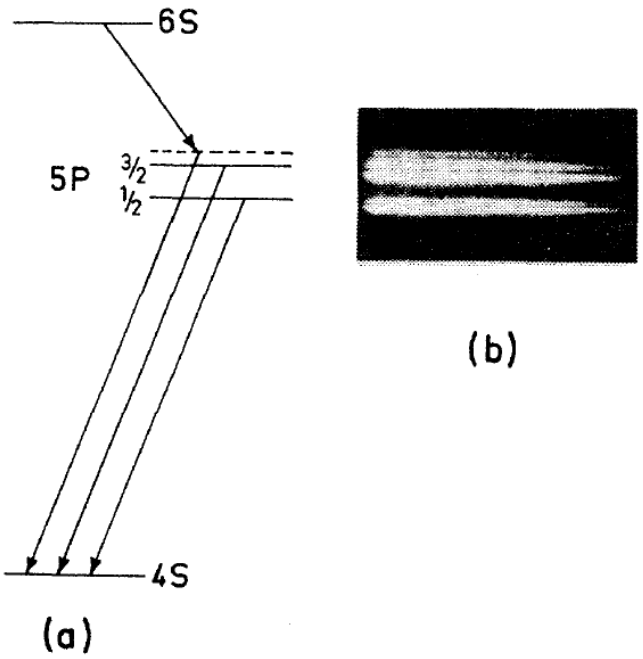

Figure 2 - Singly-stimulated 2PE in potassium [17]

Figure 2b shows three distinct emission lines: emission from the $5P_{1/2}$ to the 4S state, from the $5P_{3/2}$ to the 4S state and from 10 cm^{-1} above the $5P_{3/2}$ state to the 4S state corresponding to the complimentary frequency ω_b. The author proved that this was indeed due to 2PE by replacing the nitrobenzene with bromonaphthalene which did not satisfy the two-photon excitation of the 6S state and consequently ω_b was not observed. The doublet structure observed in the spectrally

resolved transition in figure 2b from the $5P_{3/2}$ to the 4S state was apparently due to high vapor pressure and disappeared when the pressure was reduced.

Subsequently, singly-stimulated 2PE was also observed by Braünlich and Lambropoulos from the metastable 2s state of deuterium atoms [15]. Stimulated anti-Stokes Raman scattering was also observed in the experiment and it was shown that it is a competing process of 2PE [16]. Not long after the observations of singly-stimulated 2PE, doubly-stimulated non-degenerate 2PE (ND-2PE) was observed through adiabatic inversion by Loy [20]. Loy used an asymmetric external electric pulse (Stark-pulse) to Stark shift the two-photon resonance of ammonia (NH_3) and sweep it through the sum of two laser frequencies. The stimulating beams were an intense beam at the $P34$ line of a CO_2 TEA laser and a weaker counter-propagating beam at the $P18$ line, approximately 10.6 μm each. The $P34$ and $P18$ while technically different beams are nearly degenerate, since the energy difference is approximately 1.6 % [21]. The sum of these two frequencies lies close to the two-photon transition in ammonia. Figure 3 shows the transmission of the weak beam as the electric field was applied. When the Stark-pulse is rising and the two-photon transition frequency is Stark shifted through resonance, a large 2PA feature appears. As the Stark-pulse is falling, the two-photon transition frequency is tuned back through resonance yielding another 2PA feature in figure 3 (a). This measurement was done at 100 mTorr, where due to the "high" pressure, collisions dominated the decay time and the stark pulse was longer than the lifetime of the final state.

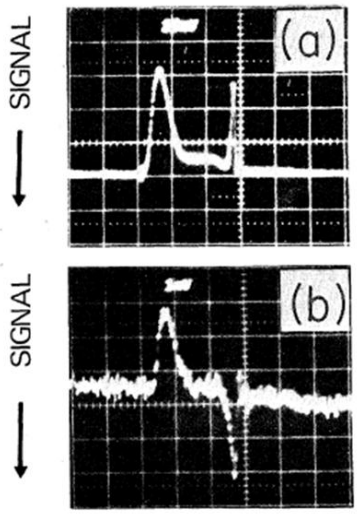

Figure 3 -Rising stark pulse induces a reduction of transmission due to 2PA, and a falling Stark pulse induces 2PA in 100 mTorr NH_3 (Top), rising Stark pulse induces 2PA and falling stark pulse yields 2PE in 9 mTorr NH_3 (bottom) [20]

The pressure of the system was then lowered to 9 mTorr, thereby increasing the decay time, since there were fewer collisions. As a result of this increase in lifetime the falling edge of the Stark-pulse yields doubly-stimulated ND-2PE of only about 0.2% gain shown in figure 3 (b). Loy proved it was in fact 2PG by showing that the signal disappeared in either the absence of a strong beam on the system or if the Stark pulse did not probe the NH_3 in a time shorter than the lifetime of the carriers in the two-photon transition state.

Fourteen years later Gauthier, Wu, Morin and Mossberg demonstrated the degenerate continuous wave (CW) two-photon laser (2PL) in dressed state Barium atoms [14]. The dressed states are shown in figure 4 where degenerate 2PG (D-2PG) occurs at $\omega_d - \Omega_d'/2$ between states $|-, \mathrm{n}+1\rangle$ and $|+, \mathrm{n}-1\rangle$ where Ω_d' is the generalized Rabi frequency of the system. The experimental setup shown in figure 5 uses an atomic beam of Barium atoms primed by the pump beam at 553.5 nm ${}^1S_0 \rightarrow {}^1P_1$ transition. The gain in these dressed states arises from hyper-Raman

scattering shown in figure 4**,** where in one photon lasing, two pump photons are annihilated and one probe beam photon is created in the transition from state |g⟩ to state |e⟩ , see figure 4a. In the case of two-photon lasing, three pump photons are absorbed and two probe photons are created shown in figure 4b.

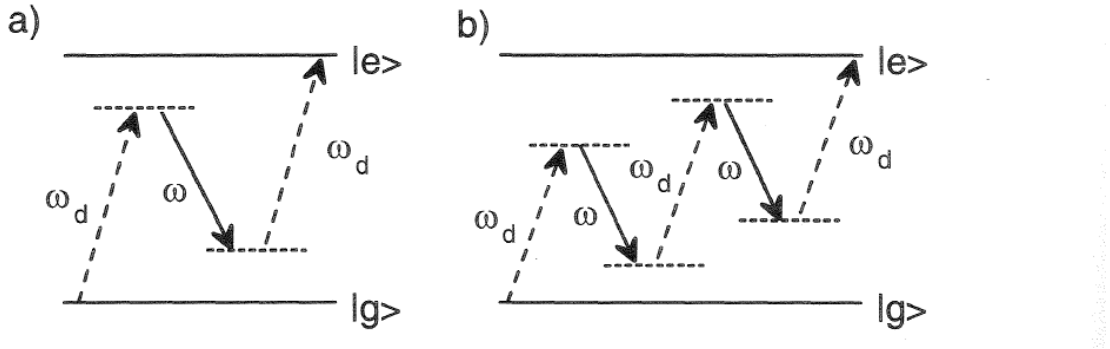

Figure 4- Photon emission (1PE) with annihilation of two pump photons (Left), 2PE with annihilation of three pump photons (right) [22]

A mutually orthogonal cavity axis, pump beam axis and atomic beam axis is utilized so wave-mixing processes are not phase matched.

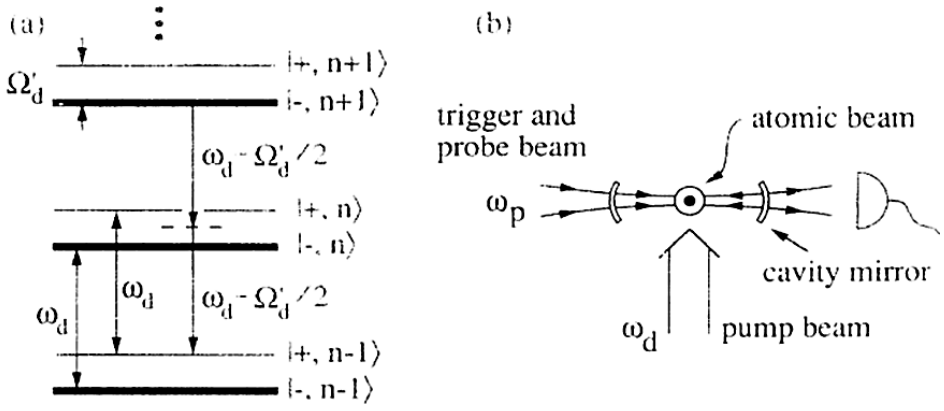

Figure 5– Dressed states of barium atoms where ω_d is the driving term (Left), experimental setup with mutually orthogonal beam, cavity, and optic axis [14]

Spontaneous two-photon emission in the cavity was not enough to trigger doubly-stimulated 2PE so a trigger pulse was added provide the cavity with enough photons to induce 2PE. The results of this experiment are shown in figure 6. Figure 6 (a) shows the output power spikes when the trigger pulse is turned on but decays to zero when the trigger pulse is turned off indicating that the trigger did not provide sufficient photons to the cavity to induce two-photon lasing. Part b shows the output power of the cavity with a higher intensity trigger pulse. A spike in the output power occurs and decays slightly before achieving a steady state output power, indicating two-photon lasing. This result is indicative of what theorized by Sorokin and Braslau [10], that in order to induce two-photon lasing a critical number of photons are required to be in the cavity. Figure 6 (c) displays the two-photon lasing on longer time scales and part d shows two-photon lasing at a different cavity resonant frequency.

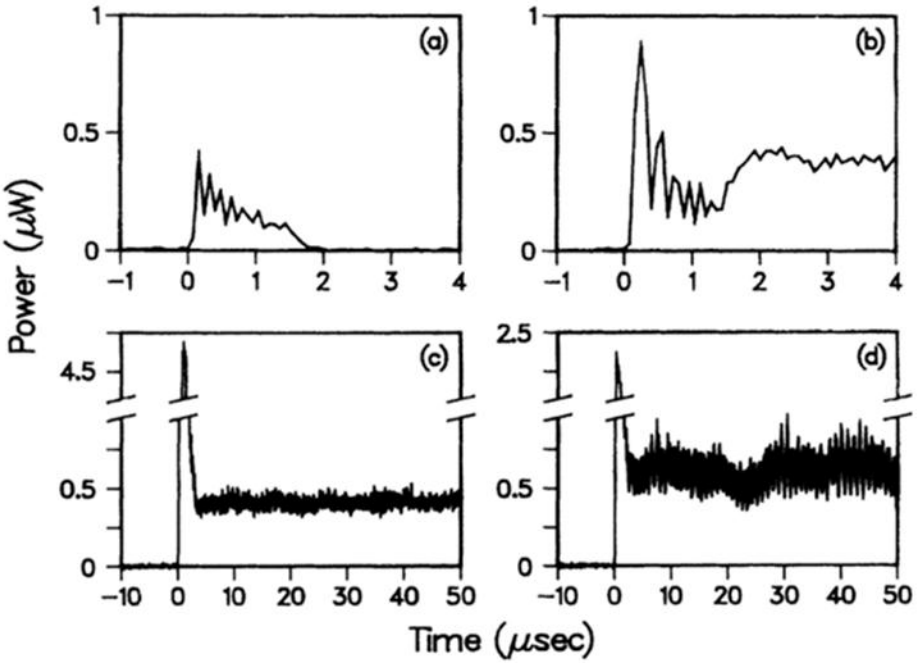

Figure 6– With a low intensity trigger pulse, output power spikes and decays (part A), with a high intensity trigger pulse, output power spikes and achieves steady state 2PL power output (part B), 2PL on longer time scales (part C), 2PL at a different cavity frequency (part D)

Gauthier determined the critical number of atoms and photons to be a function of the fundamental linewidth Γ_c, the spontaneous emission linewidth 2γ, the resonant Rabi frequency Ω_d and the effective fundamental mode volume $V_{eff} = \pi w_o^2 L_c$, where L_c is the cavity length. The minimum number of atoms in the cavity is approximately

$$N_{th}^{min} \approx 25.4\Omega_d\Gamma_c/\left(6\,\gamma\lambda^2 c/\pi\, V_{eff}\right)^2 \tag{1.0}$$

And the minimum number of photons in the cavity is approximately

$$m_{th}^{min} \approx 4.7\Omega_d\gamma/\left(6\,\gamma\lambda^2 c/\pi\, V_{eff}\right) \tag{1.1}$$

The feasibility of using semiconductors as a 2PG media as opposed to dressed state atoms was considered by Charles Ironside [18]. He suggested that semiconductors could make viable D-

2PG media since semiconductor two-photon effects were well understood, and the maturity of semiconductor technology would allow for easier development of a D-2PG device. Using the electron transition rate for 2PA [23], Ironside developed the D-2PG coefficient in a semiconductor assuming an intrinsic semiconductor in thermal equilibrium at low temperature, $E_g \gg kT$, while also ignoring some competing affects. The low temperature approximation assumes that all the energy levels in the conduction bands up to E_{F_c} are full of electrons and all the energy levels above E_{F_c} are empty. Due to this approximation some of the spectral dependence was lost but it allowed for the D-2PG coefficient to be simply expressed as,

$$\gamma_2 = 3.1 \times 10^3 \frac{\sqrt{E_p}}{n^2 E_g^3} F\left(\frac{2\hbar\omega_p}{E_g}\right) \tag{1.2}$$

Where E_p is the Kane energy parameter, E_g is the bandgap energy, n is the refractive index and E_{F_c} and E_{F_c} are quasi Fermi levels.

$F(x)$ is a spectral function and is determined by the band structure of the semiconductor. For direct-gap semiconductors with approximately parabolic bands such as GaAs,

$$F(x) = \frac{(x-1)^{3/2}}{x^5} \tag{1.3}$$

Following this theoretical study of 2PE in the semiconductors, Orenstein and collaborators made several publications dealing with spontaneous, singly-stimulated [24], and doubly-stimulated [25] 2PE in semiconductors. The first of their experiments uses a 100 mW continuous-wave 514 nm argon laser focused to 30 μm in order to optically excite a 200 μm thick piece of bulk GaAs. Spontaneous 2PE and singly-stimulated 2PE were measured with stimulating beams of 1630 nm

and 1600nm at 0.2mW. These input beams generated peaks in the spectrum corresponding to the complimentary wavelength at 1451 nm and 1476 nm, respectively. Figure 7a depicts these results.

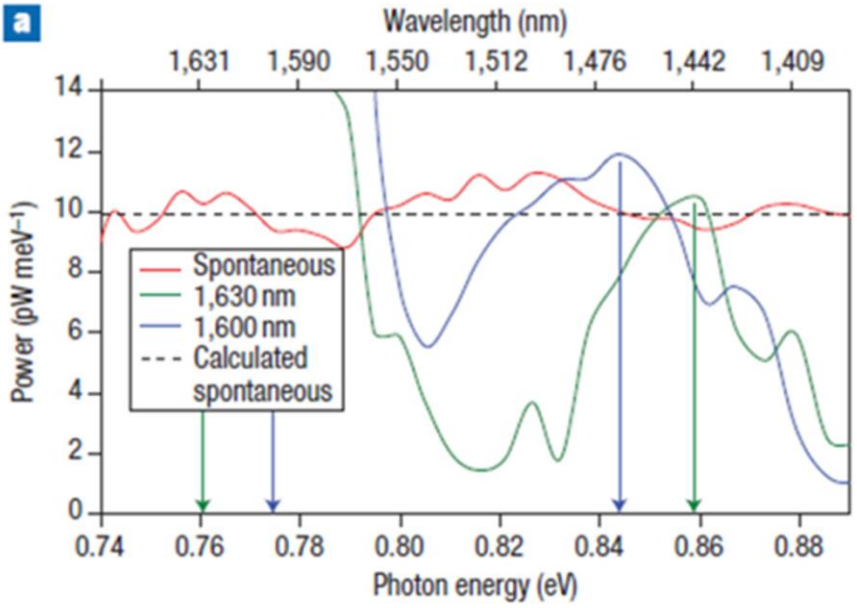

Figure 7– Optically pumped GaAs shows peaks at 1451 nm and 1476 nm when irradiated by 1630 nm and 1600 nm, respectively, indicative of singly-stimulated 2PE.

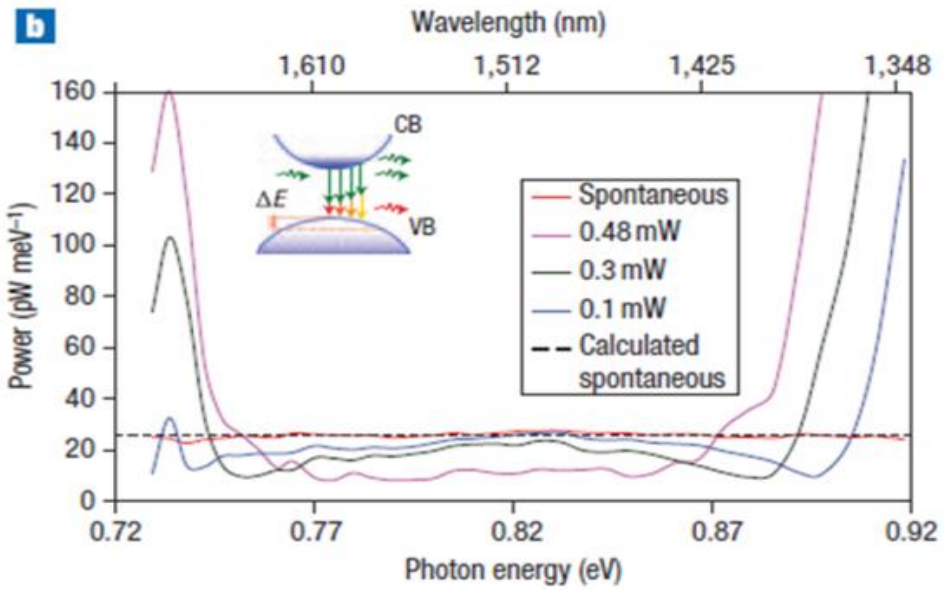

Figure 8– Increasing input power at 1,310 nm (0.946 eV) linearly increases output power at 1,691nm (0.733 eV)

Another experiment was done to study the relation between stimulating power and the output power at the complimentary wavelength. Using a 1,310 nm (0.946 eV) beam and increasing the power of the beam, the complimentary wavelength, 1,691 nm (0.733 eV), power was shown to be linearly dependent on the input power. The results are displayed in figure 8.

Orenstein and collaborators then observed D-2PG in an electrically pumped AlGaAs *p-i-n* heterostructure [25]. 2PG was observed in two different ways; the first, a stimulating pulsed beam at 1,560 nm, with a photon energy slightly larger than $E_g/2$, was coupled into the guiding layer of the structure. When the current passing through the device was low, the stimulating pulse underwent 2PA, the excited carries would then spontaneously one photon emit at about 800 nm. When the injection current reached $1300\ \mathrm{A/cm^2}$, α_2 became zero and as the current increased, $\alpha_2$went negative corresponding to 2PG. As 2PG increased the emission of 800 nm

would decrease. The relationship between OPE and 2PA/2PG behaves according to $\alpha_2 I^2$. The results are shown in the figure below

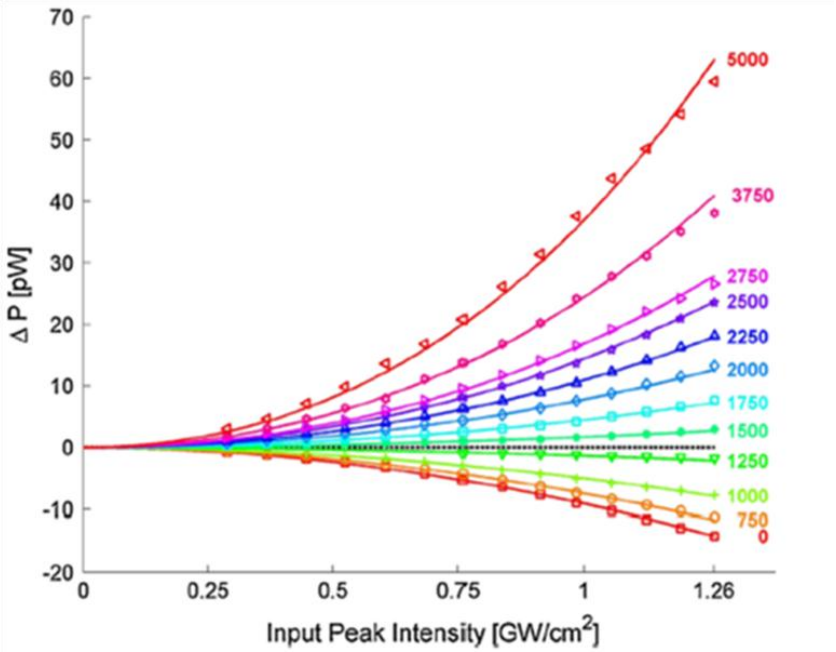

Figure 9–2PA reduces quadratically as injection current is increased, once 1300 A/cm^2 is reached 2PE increases quadratically with increasing injection current

As shown in figure 9, the reduction of the 800 nm fluorescence (ΔP) changes quadratically as the input power increases. Depending on the current density, ΔP is either positive or negative with negative ΔP corresponding to an increase in the number of photons at 800 nm and positive ΔP corresponding to a reduction of the 800 nm fluorescence. At the highest current density $\gamma_2 =$ 3.15 cm/GW after corrections for the linear loss. An interesting phenomenon that can be noticed here is the effect of 2PG on the output irradiance is greater than the effect of 2PA with zero injection current. This illustrates that $\gamma_2 > -\alpha_2$, γ_2 is the 2PG coefficient, which the Nevet *et al.* attributes to band gap renormalization. Band gap renormalization would cause a decrease in the

band gap energy with increasing carrier concentration and since γ_2 has a E_g^{-3} dependence, γ_2 would increase dramatically.

CHAPTER 2: THEORETICAL BACKGROUND

2.1 Nonlinear Optics Introduction

In a physical sense nonlinear optics is the change light experiences passing through a material due to light. Nonlinear effects can be caused by a single high intensity beam that is altered while passing through a material, which is the premise of a Z-Scan [26] for example, or, where an intense beam causes a change in a material that another beam observes, such as pump-probe. There are several types of interactions that the field of nonlinear optics covers; however, here in this work we limit the interactions to mostly "instantaneous" and local nonlinearities with the exception of free carrier absorption or FCA. Instantaneous nonlinearities usually deal with bound electrons where the interactions are on the order of femtoseconds in time and where the motion of the nucleus is neglected using the Born-Oppenheimer approximation due to the nucleus's large mass in comparison to the electron. Considering only local nonlinearities we will neglect any nonlinearity that is due to the redistribution of generated carriers far from the incident beam. In the case of 2PE, much of the theory can be described through 2PA since the processes are inverses of one another.

2.2 Two–Photon Absorption (2PA)

Electronic nonlinearities in materials arise from the way an electron reacts to the incident electric field. If the electron is considered as a mass on a spring the nonlinearities arise in correction terms to the linear equation of motion. Another way these nonlinearities can be dealt with mathematically is through Maxwell's equations and the expansion of the polarization density $\vec{P}$. Concerning ourselves with the interaction of two different frequency inputs ω_a and ω_b we begin

with the evolution of the electric field propagating through a lossless material in the absence of any sources, with negligible magnetic effects and infinite plane waves.

$$\nabla^2\vec{E} - \frac{n^2}{c^2}\frac{\partial^2\vec{E}}{\partial t^2} = \mu_o\frac{\partial^2\vec{P}_{NL}}{\partial t^2} \tag{2.0}$$

An incident electric field comprised of two copolarized monochromatic plane waves of frequencies $\omega_a$and ω_b is defined as

$$\begin{aligned}\vec{\mathrm{E}}(\vec{\mathrm{r}},\mathrm{t}) = &\left(\frac{1}{2}\mathcal{E}_a(z)e^{-i(\omega_a t-\mathrm{k}_a\cdot\mathrm{r})} + \frac{1}{2}\mathcal{E}_\mathrm{b}(z)e^{-i(\omega_b t-\mathrm{k}_b\cdot\mathrm{r})}\right)\hat{\mathrm{s}} \\ &+\left(\frac{1}{2}\mathcal{E}_a^*(z)e^{i(\omega_a t-\mathrm{k}_a\cdot\mathrm{r})} + \frac{1}{2}\mathcal{E}_b^*(z)e^{i(\omega_b t-\mathrm{k}_b\cdot\mathrm{r})}\right)\hat{\mathrm{s}}\end{aligned} \tag{2.1}$$

Where $\mathcal{E}_a(z)$ defines the envelope of the electric field and $\hat{\mathrm{s}}$ is the propagation vector. Inserting the field from equation 2.1 propagating in the z-direction into equation 2.0 yields

$$\begin{aligned}\frac{1}{2}\Bigg[&\left(\frac{\partial^2\mathcal{E}_a}{\partial z^2} + 2ik_a\frac{\partial\mathcal{E}_a}{\partial z} + \left(\frac{n_a}{c}\right)^2\left(\frac{\partial^2\mathcal{E}_a}{\partial t^2} - 2i\omega_a\frac{\partial\mathcal{E}_a}{\partial t}\right)\right)e^{-i(\omega_a t-k_a z)} + \\ &\left(\frac{\partial^2\mathcal{E}_b}{\partial z^2} + 2ik_b\frac{\partial\mathcal{E}_b}{\partial z} + \left(\frac{n_b}{c}\right)^2\left(\frac{\partial^2\mathcal{E}_b}{\partial t^2} - 2i\omega_a\frac{\partial\mathcal{E}_b}{\partial t}\right)\right)e^{-i(\omega_b t-k_b z)} + c.c\Bigg] \\ &= \mu_o\frac{\partial^2\vec{P}}{\partial t^2}\end{aligned} \tag{2.2}$$

where $\mathcal{E}_a$ and $\mathcal{E}_b$ are functions of *z.* The second derivative terms with respect to z and t can be neglected if it is assumed that the envelope governing the electric field varies slowly in both space and time. This approximation is known as the slowly-varying-envelope-approximation (SVEA) [27]. This leads to

$$\frac{1}{2}\left[\begin{array}{c}\left(2ik_a\,\frac{\partial\mathcal{E}_a}{\partial z}+\left(\frac{n_a}{c}\right)^2\left(-2i\omega_a\,\frac{\partial\mathcal{E}_a}{\partial t}\right)\right)e^{-i\,(\omega_a t-k_a z)}\;+\\ \left(2ik_b\,\frac{\partial\mathcal{E}_b}{\partial z}+\left(\frac{n_b}{c}\right)^2\left(-2i\omega_a\,\frac{\partial\mathcal{E}_b}{\partial t}\right)\right)e^{-i\,(\omega_b t-k_b z)}\;+c.c\end{array}\right]=\mu_o\frac{\partial^2\vec{P}}{\partial t^2} \tag{2.3}$$

The polarization density $\vec{P}$ can now be expanded in terms of the order of the material susceptibility and electric field

$$\frac{\vec{P}}{\varepsilon_0}=\chi^{(1)}\cdot\vec{\mathrm{E}}+\chi^{(2)}\cdot\vec{\mathrm{E}}^2+\chi^{(3)}\cdot\vec{\mathrm{E}}^3+\cdots\chi^{(\mathrm{n})}\cdot\vec{\mathrm{E}}^{\mathrm{n}} \tag{2.4}$$

where ε_0 is the permittivity of free space, $\chi^{(n)}$ represents the material nth order susceptibility to the electric field $\vec{\mathrm{E}}$. The linear case refers to $\vec{P}=\varepsilon_0\chi^{(1)}\cdot\vec{\mathrm{E}}$, however, nonlinearities only appear in the subsequent terms beginning with $\chi^{(2)}$, the second order susceptibility. The second order polarization can be expressed in terms of the sum of the incident electric fields and the second order susceptibility.

$$\vec{\mathrm{P}}_J^{(2)}(\omega)=\;\varepsilon_0\iint_{-\infty}^{\infty}\chi_{jkl}^{(2)}(\,\omega;\omega_1,\omega_2)\vec{\mathrm{E}}_k(\omega_1)\vec{\mathrm{E}}_l(\omega_2)\delta(\omega-\omega_1-\omega_2)d\omega_1 d\omega_2 \tag{2.5}$$

Where $\vec{\mathrm{E}}_k$ and $\vec{\mathrm{E}}_l$ are the incident electric fields of angular frequency ω_1 and ω_2 respectively and the tensor and vector indices, *j*, *k*, *l* are dummy variables that refer to any position vector in Cartesian space *x*, *y*. The notation used defining $\chi^{(2)}(\omega;\omega_1,\omega_2)$ denotes $\omega=\omega_1+\omega_2$. $\chi^{(2)}$ governs parametric processes such as optical rectification [28], sum and difference frequency generation and second harmonic generation [29].

The 3rd order susceptibility, $\chi^{(3)}$, governs many of the phenomena of interest, such as such as third harmonic generation, four-wave mixing, nonlinear refraction (NLR) and 2PA [30]. Similar

to $\chi^{(2)}$, $\chi^{(3)}$ can be also be expanded with regard to the permutations arising from the incident electric fields

$$\vec{\mathrm{P}}_j^{(3)}(\omega) = \varepsilon_0 \iiint_{-\infty}^{\infty} \chi_{jklm}^{(3)}(\omega;\omega_1,\omega_2,\omega_3)\vec{\mathrm{E}}_k(\omega_1)\vec{\mathrm{E}}_l(\omega_2)\vec{\mathrm{E}}_m(\omega_3) \\ \delta(\omega-\omega_1-\omega_2-\omega_3)d\omega_1 d\omega_2 d\omega_3 \tag{2.6}$$

where k_j and $\mathcal{E}_j$ are the wave vector and complex amplitude, respectively, of the j^{th} wave.

If we are strictly looking at 2PA at ω_a then

$$\vec{\mathrm{P}}_j^{(3)}(\omega) = \frac{1}{2}\mathcal{P}_j^{(3)}(\omega_a)e^{-i(\omega_a t - k_a z)}\hat{\mathrm{s}} + c.c \tag{2.7}$$

Where $\mathcal{P}_j^{(3)}(\omega_a)$ is the complex polarization density amplitude and is given by

$$\mathcal{P}_j^{(3)} = \frac{\varepsilon_0}{4}\Big\{3\chi_{xxxx}^{(3)}(\omega_a;\omega_a,-\omega_a,\omega_a)|\mathcal{E}_a|^2\mathcal{E}_a \\ + 6\chi_{xxxx}^{(3)}(\omega_a;\omega_a,-\omega_b,\omega_b)|\mathcal{E}_b|^2\mathcal{E}_a\Big\} \tag{2.8}$$

Where $\mathcal{P}_j^{(3)}(\omega_a)$ is the sum of the self-nonlinearities, where a wave of frequency ω_a acts upon itself, and cross-nonlinearities, where a frequency ω_b acts upon a wave of frequency ω_a. It should be noted that equation 2.8 has been reduced due to *intrinsic permutation symmetry* [27]. This symmetry is was leads to the factors of three and six in the first and second terms, respectively. Inserting equation 2.7 into equation 2.3 and looking at the response at the input frequency ω_a yields

$$e^{-i\,(\omega_a t - k_a z)}\left(2ik_a\,\frac{\partial \mathcal{E}_a}{\partial z} + 2ik_a\frac{n_a}{c}\,\frac{\partial \mathcal{E}_a}{\partial t}\right) + c.c \tag{2.9}$$

$$= -{\omega_c}^2 \mu_o \mathcal{P}_j^{(3)}(\omega_a, \mathrm{z}) e^{-i(\omega_a t - k_a z)} + c.c$$

Assuming a long pulse with a spatial width far larger than the sample thickness, the term $\frac{n}{c}\frac{\partial \mathcal{E}}{\partial t}$ can be neglected. In cases where the spatial width of the pulse is shorter than the sample, $\mathcal{E}_a(z)$ can transform into another reference frame that moves with the pulse. This leads to

$$\frac{\partial \mathcal{E}_a(\omega_a, \mathrm{z})}{\partial z} = \frac{i\omega_a \mathcal{P}_j^{(3)}(\omega_a, \mathrm{z}) e^{-i\Delta k z}}{2cn_a\epsilon_0} \tag{2.10}$$

Where Δk is the difference between the wavevector of the generated polarization and the wavevector of the incident wave which in this case is zero since we are strictly looking at 2PA.

Substituting equation 2.7, $\mathcal{E}_a(z) = \sqrt{\frac{2\mathrm{I}_a(z)}{n_a c\epsilon_0}}\exp(i\Delta\phi_a(z))$ and $\mathcal{E}_b(z) = \sqrt{\frac{2\mathrm{I}_b(z)}{n_b c\epsilon_0}}\exp(i\Delta\phi_b(z))$ into equation 2.10 above, and separating the real and imaginary terms, we can develop the evolution of the irradiance as pulse propagates, ${dI_a}/{dz}$, as well as the evolution of the phase ${\partial\Delta\phi_a(z)}/{dz}$. From these irradiance and the phase which we will develop expressions for α_2, the nonlinear absorption coefficient and n_2, the nonlinear refraction coefficient. The evolution of the irradiance at ω_a is

$$\frac{\partial I_a(z)}{\partial z} = -\alpha_2(\omega_a;\omega_a)I_a^2(z) - 2\alpha_2(\omega_a;\omega_b)I_b(z)I_a(z) \tag{2.11}$$

Where

$$\alpha_2(\omega_a;\omega_b) = \frac{3\omega_a}{2\varepsilon_0 n_a n_b c^2}\chi_{\mathcal{I}}^{(3)}(\omega_a;\omega_a,-\omega_b,\omega_b) \tag{2.12}$$

Now taking the real terms of the derivatives of $\mathcal{E}_a(z)$, $\mathcal{E}_b(z)$ and $\chi^{(3)}$ leads to

$$\frac{\partial\Delta\phi_a(z)}{\partial z} = k_{0,a}n_2(\omega_a;\omega_a)I_a(z) + 2k_{0,a}n_2(\omega_a;\omega_b)I_b(z) \tag{2.13}$$

Where

$$n_2(\omega_a;\omega_b) = \frac{3}{4\varepsilon_0 n_a n_b c}\chi_{\mathcal{R}}^{(3)}(\omega_a;\omega_a,-\omega_b,\omega_b) \tag{2.14}$$

Where k_0 is the free space wavenumber. The subscripts $\mathcal{R}$ and $\mathcal{I}$ respectively refer to the real and imaginary components of $\chi^{(3)}$. The change of $I_a(z)$ is dependent on both degenerate 2PA represented by $-\alpha_2(\omega_a;\omega_a)I_a^2(z)$ and non-degenerate 2PA $-2\alpha_2(\omega_a;\omega_b)I_b(z)I_a(z)$. The factor of two difference is a result of the cross-nonlinearity between fields ω_a and ω_b. Solving the differential equation 2.11 for a single beam at ω_a, results in a z-dependent irradiance of

$$I_a(z) = \frac{I_a(0)}{1+\alpha_2(\omega_a;\omega_a)I_a(0)z} \tag{2.15}$$

In the case of a substantial carrier population in the ground state, i.e. no population inversion, 2PA will occur and thus the irradiance decreases as the beam propagates through a material following the inverse relationship with z (see Eq. 2.15) which is dramatically different than linear absorption where the irradiance decreases by an exponential decay. When there is some carrier population $\alpha_2(\omega_a;\omega_a)$ may become zero referring to two-photon transparency. If population inversion is reached, 2PA will become negative thus becoming 2PG, and the irradiance will rapidly diverge as the beam passes through the sample as shown in figure 10. Plotting equation 2.15 shows this divergence of 2PE as the propagation distance increases.

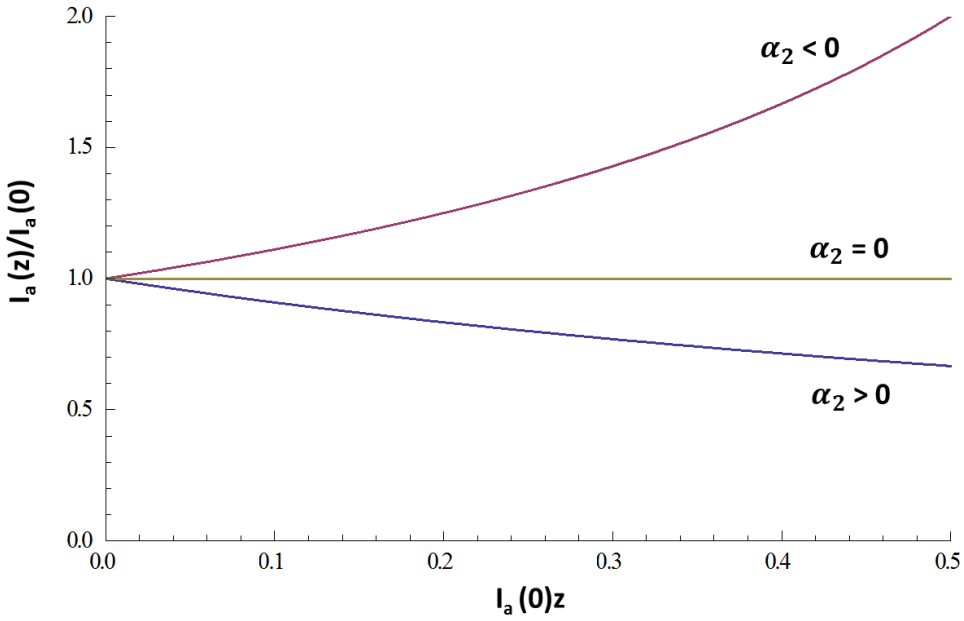

Figure 10- Normalized irradiance D-2PA (blue) and D-2PE (violet) as a function of propagation distance.

For two beams, if we assume the case where the irradiance of one beam, say I_b, is far larger than the second beam, I_a, like in a pump-probe experiment, I_b can alter the effective linear coefficient that the first beam observes. Thus equation 2.15 changes in the low depletion limit i.e. I_b has no z dependence, to

$$I_a(z) = I_a(0)e^{-\alpha_2(\omega_a;\omega_a)I_b z} \tag{2.16}$$

As a result, the magnitude of 2PA or 2PE can be tuned by the irradiance of the second beam, in this case, I_b.

2.3 Perturbation Approach to Two-Photon Transition Rate

Since a large majority of this work deals with two-photon processes it is both useful and necessary to calculate the two-photon transition rate; one method of achieving this is through second order perturbation theory. Beginning with an unperturbed system, the time-independent

Schrödinger equation, $\hat{H}_o|\psi_n\rangle = E_n|\psi_n\rangle$ can be satisfied with the unperturbed time-independent Hamiltonian $\hat{H}_o$, where $|\psi_n\rangle$ represents the energy eigenstates of the system and E_n represents the energy eigenvalues. Now consider a time varying quantum state $|\Psi(t)\rangle$, which satisfies the time-dependent Schrödinger equation

$$i\hbar\frac{\partial}{\partial t}|\Psi(t)\rangle = \hat{H}|\Psi(t)\rangle \tag{2.17}$$

Where $|\Psi(t)\rangle = \sum_n a_n(t)|\psi_n\rangle e^{-iE_n t/\hbar}$, and $a_n(t)$ refers to the time dependent, normalized, complex probability amplitudes, where the probability of finding the system in the *n*th state is $|a_n|^2$. The unperturbed system will now be perturbed with a small time varying perturbation so let $\hat{H} = \hat{H}_0 + \hat{H}_p(t)$. The time-dependent Schrödinger equation is then

$$\sum_n (i\hbar\dot{a}_n(t) + a_n E_n)|\psi_n\rangle e^{-iE_n t/\hbar} = \sum_n a_n(t)\left(\hat{H}_0 + \hat{H}_p(t)\right)|\psi_n\rangle e^{-iE_n t/\hbar} \tag{2.18}$$

where $\dot{a}_n(t)$ is the first order time derivative of $a_n(t)$. Using the time-independent Schrödinger equation to replace $\hat{H}_o|\psi_n\rangle$ with $E_n|\psi_n\rangle$, $E_n|\psi_n\rangle$ can thus be canceled. Multiplying each side by $\langle\psi_q|$, yields

$$i\hbar\dot{a}_n(t)e^{-\frac{iE_q t}{\hbar}} = \sum_n a_n(t)\langle\psi_q|\hat{H}_p(t)|\psi_n\rangle e^{-\frac{iE_n t}{\hbar}} \tag{2.19}$$

Equation 2.19 will allow us to determine the temporal evolution of the perturbed system. Expanding a_n as a power series yields,

$$a_n = a_n^{(0)} + \gamma a_n^{(1)} + \gamma^2 a_n^{(2)} + \cdots \tag{2.20}$$

where γ is housekeeping term used in the perturbation approach. Inserting equation 2.20 into the equation 2.19 and replacing $\widehat{H}_p(t)$ with $\gamma\widehat{H}_p(t)$, and equating the powers of γ on each side, a zeroth, first order term and second order term can be extracted.

$$\dot{a}_q^{(0)}(t) = 0 \tag{2.21}$$

$$\dot{a}_q^{(1)}(t) = \frac{1}{\mathrm{i}\hbar}\sum_n a_n^{(0)}(t)\langle\psi_q|\widehat{H}_p(t)|\psi_n\rangle e^{-i\omega_{qn}t} \tag{2.22}$$

$$\dot{a}_q^{(2)}(t) = \frac{1}{\mathrm{i}\hbar}\sum_n a_n^{(1)}(t)\langle\psi_q|\widehat{H}_p(t)|\psi_n\rangle e^{-i\omega_{qn}t} \tag{2.23}$$

$a_q^{(0)}(t)$ is simply the unperturbed solution and is zero since there is no change in the states in the lack of a perturbation. $\dot{a}_q^{(1)}(t)$, the first order term, obtained by equating γ^1 terms on both sides of the expanded equation, represents the correction to the first order solution where ω_{qn} is equivalent to $\left(E_q - E_n\right)/\hbar$. Higher order terms such as $\dot{a}_q^{(2)}(t)$ all give higher order corrections to the zeroth order solution.

In our case, the perturbation on this system is caused by photons, such that $a_q^{(1)}(t)$ corresponds to a single photon induced electronic transition and the term $a_q^{(2)}(t)$ refers to transitions induced by two-photons. The probability of a transition per unit time from an initial state $|\psi_i\rangle$ to a final state $|\psi_f\rangle$ for one photon or two-photons, can be formulated by Fermi's Golden Rule (FGR). The transition rate for a two-photon process can be determined [1] from the time derivative of $\left|a_q^{(2)}(t)\right|^2$, yielding

$$W_{2P}^{if} = \frac{2\pi}{\hbar}\left|\sum_{n}\frac{M_{fj}^{b}M_{ji}^{a}}{E_{ji}-\hbar\omega_{a}}+\frac{M_{fj}^{a}M_{ji}^{b}}{E_{ji}-\hbar\omega_{b}}+\frac{M_{fj}^{b}M_{ji}^{a}}{E_{fj}-\hbar\omega_{b}}+\frac{M_{fj}^{a}M_{ji}^{b}}{E_{fj}-\hbar\omega_{a}}\right|^{2}\times \tag{2.24}$$

$$\delta\left(E_{fi}-\hbar\omega_{b}-\hbar\omega_{a}\right)$$

where a and b represent the individual photons involved in the transition, the term, $\langle\psi_q|\widehat{H}_p(t)|\psi_n\rangle = M_{qn}$, is the matrix elements of the interaction and the transition rate summed is over all intermediate states $|\psi_j\rangle$. Furthermore, the denominators of W_{2P}^{if} shows that as one of the photon energies approaches either E_{ji} or E_{fj}, the two-photon transition rate will increase dramatically which is known as intermediate state resonance enhancement (ISRE) [31].

The transition rate W_{2P}^{if} can describe any type of two-photon transition between two states; meaning if the energy of the initial state is greater than the final state, W_{2P}^{if} refers to 2PE. In contrast, if the initial state is of lower energy than the final state, W_{2P}^{if} refers to 2PA. One can solve for 2PA/2PE from FGR by using the irradiance rate equation

$$\frac{\partial I_a}{\partial z} = -2\alpha_2(\omega_a;\omega_b)I_aI_b = -N\hbar\omega_a W_{fi}^{(2)} \tag{2.25}$$

Where $\alpha_2(\omega_a;\omega_b)$ is the absorption of ω_a photons due to the presence of ω_b photons, N is the density of absorbers per unit volume. α_2 can be described as

$$\alpha_2(\omega_a;\omega_b) = \frac{N\hbar\omega_a W_{fi}^{(2)}}{2I_aI_b} \tag{2.26}$$

The 2PE equation is the same except that $\alpha_2(\omega_a;\omega_b)$ is now negative.

2.4 Two-Photon Absorption in Semiconductors

Since the experiments in this work all are on GaAs it is useful to look at how 2PA behaves in semiconductors. Semiconductors, in comparison to the discrete states described in the previous section, contain quasi-continuum bands of energy levels. The two bands that we will be primarily dealing with, the valence and conduction bands are separated by a region known as the energy gap where no real states exist. In the case of 2PA, this means that the initial and final states are the valence and conduction band respectively. From FGR, the intermediate states, $|\psi_j\rangle$, become either the valence or conduction band, depending on the type of transition. Therefore, in semiconductors a 2PA process is described by an inter-band transition i.e. valence to conduction band, followed by an intra-band (self) transition, conduction to conduction, or vice versa (see figure 11). Therefore, FGR for ND-2PA becomes

$$W_{2P}^{if} = \frac{2\pi}{\hbar}\left|\sum_{vc}\frac{M_{vc}^{b}M_{vv}^{a}}{-\hbar\omega_a} + \frac{M_{vc}^{a}M_{vv}^{b}}{-\hbar\omega_b} + \frac{M_{cv}^{b}M_{cc}^{a}}{\hbar\omega_b} + \frac{M_{cv}^{a}M_{cc}^{b}}{\hbar\omega_a}\right|^2 \times \delta(E_{cv} - \hbar\omega_b - \hbar\omega_a) \tag{2.27}$$

Where subscripts c and v refer to the conduction band and valence band respectively.

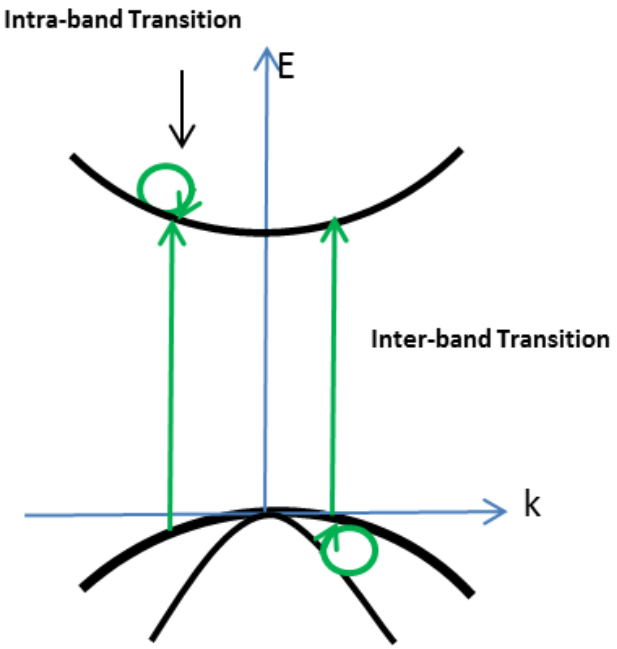

Figure 11 – Two-photon absorption in a semiconductor

Since we now have bands and not discrete states, equation 2.26 changes. If we assume the bands to be parabolic, the 2PA [32, 33] coefficient can be expressed as

$$\alpha_2(\omega_a;\omega_b) = K\frac{\sqrt{E_p}}{n_a n_b E_g^3}F_2\left(\frac{\hbar\omega_a}{E_g};\frac{\hbar\omega_b}{E_g}\right) \tag{2.28}$$

Where E_p is the Kane energy parameter, K is a material independent constant

3100 $GW\ cm^{-1}\ eV^{-\frac{5}{2}}$ [34] and in units such that the E_p, and the band gap energy, E_g, are in eV, and $\alpha_2(\omega_a;\omega_b)$ is in cm/GW, and the spectral function F_2 is given by

$$F_2(x_1;x_2) = \frac{(x_1 + x_2 - 1)^{3/2}}{2^7 x_1 {x_2}^2}\left(\frac{1}{x_1}+\frac{1}{x_2}\right)^2 \tag{2.29}$$

For decreasing values of x_2 in equation 2.29, which corresponds to increasing nondegeneracy there is a several orders of magnitude enhancement over the degenerate case $x_2 = x_1$. In GaAs,

using 3100 $GW\ cm^{-1}\ eV^{-\frac{5}{2}}$ for K and 25.7 eV [35] for E_p, $\alpha_2$can be enhanced as the interacting beams become more nondegenerate, as figure 12 shows. The plot shows and increase of α_2 by a factor of 130 from degeneracy, represented by $\hbar\omega_b = \hbar\omega_a$, to where $\hbar\omega_b$ has energy that is a tenth of the energy gap, $0.1E_{gap}$. This enhancement agrees well with both the results and predictions made by Fishman [33] who observed a factor of 127 enhancement. Once again this is due to both photons becoming resonant with transitions in the semiconductor; the high energy photon becomes resonant with the inter-band transition and the low energy photon becomes resonant with the intra-band transition.

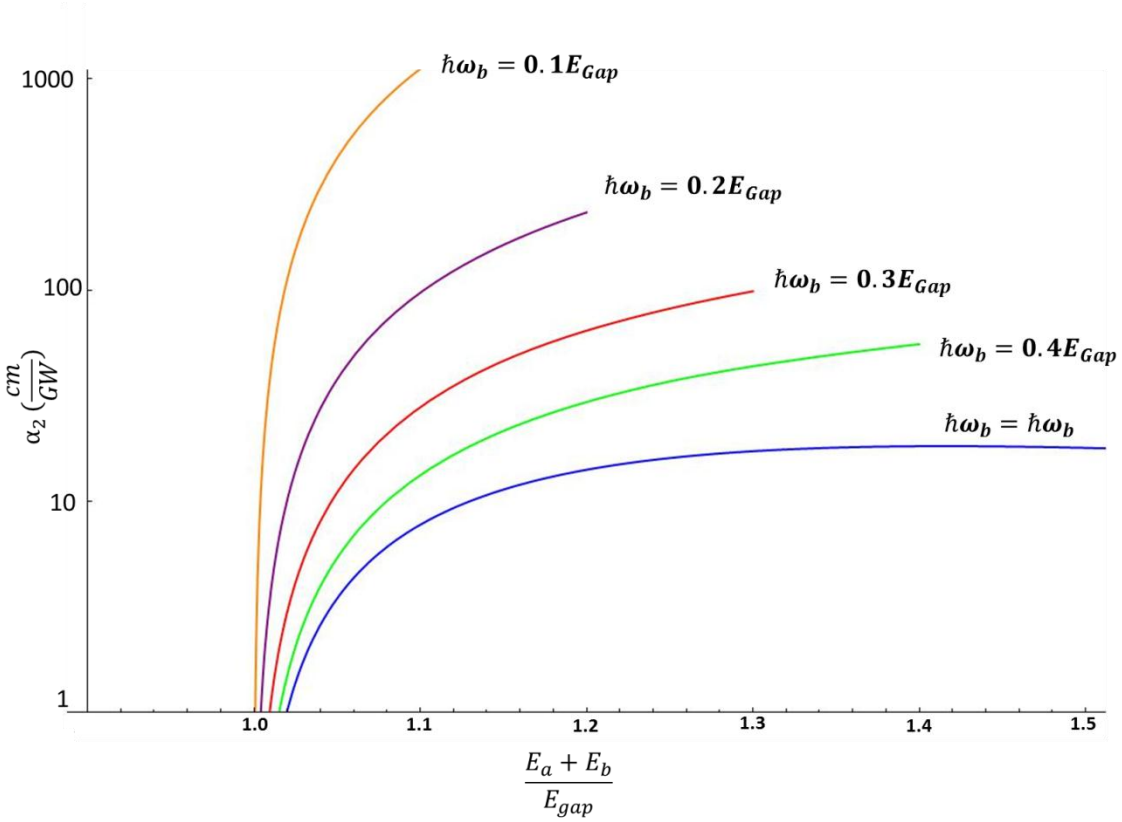

Figure 12 – Theoretical plot of α_2 in GaAs for various values of $\hbar\omega_a$ and variable $\hbar\omega_b$ energies.

Cirloganu *et al.* [36] examined this phenomena experimentally for a variety of direct-gap semiconductors. Cirloganu found that in ZnO with a photon of energy of $\hbar\omega_b = 0.08E_{gap}$, α_2 was 270 times greater than the value yielded by the degenerate case. This enhancement has hence been utilized in endeavors requiring the photodetection of infrared pulses [33].

Since 2PA exhibits this enhancement, it has been theorized by Pattanaik [37] that 2PG would also exhibit this same type of enhancement. Following Ironside [18], he calculated that the gain, to be

$$\gamma_2(\omega_a;\omega_b) = \alpha_2(\omega_a;\omega_b)\cdot\left(f_c(\hbar\omega_a,\hbar\omega_b) - f_v(\hbar\omega_a,\hbar\omega_b)\right) \tag{2.30}$$

Where $\alpha_2(\omega_a;\omega_b)$ can be seen in equation 2.28 and where f_c and f_v are the nonequilibrium Fermi functions

$$f_{c,v}(\hbar\omega_a,\hbar\omega_b) = \frac{1}{1+e^{\frac{E_{c,v}\pm\frac{m_r}{m_{c,v}}(\hbar\omega_a+\hbar\omega_b-E_g)-E_{F_{c,v}}}{k_BT}}} \tag{2.31}$$

Where E_v and E_c are the maximum energy of the valence band and minimum of the conduction band respectively, E_{F_c} is the quasi Fermi level of the conduction band and E_{F_v} is the quasi Fermi level of the valence band, m_r is the reduced mass given by

$$\frac{1}{m_r} = \frac{1}{m_c} + \frac{1}{m_v} \tag{2.32}$$

Where m_c and m_v are the effective masses of an electron in the conduction band a hole in the valence band respectively. $E_{F_{c,v}}$ were computed using

$$E_{F_c} - E_{F_v} = E_g + (3\pi^2)^{2/3} \frac{\hbar^2}{2m_r} \Delta N^{2/3} \tag{2.33}$$

Where we have assumed a fixed carrier concentration of $\Delta N = 5 \times 10^{18}$ cm^{-3} carriers at room temperature.

Plotting the $\gamma_2$function (Eq. 2.30) at 300 K (solid, red curve) the two-photon gain coefficient is approximately 60 cm/GW with $\hbar\omega_b$ photon energy of $0.2E_{gap}$ at a photon energy sum of $1.1E_{gap}$. The two-photon gain coefficient for $\hbar\omega_b = 0.2E_{gap}$ is shown here because one of the beams in our experiments, the infrared pump, has a wavelength of 4.4 μm which is approximately 20% of the band gap of GaAs. For a degenerate photon pair (green curves) the maximum gain at room temperature (solid, green curve) is about 6 cm/GW at $1.1E_{gap}$ which means that there is an order of magnitude increase between photon energies of $\hbar\omega_b = 0.2E_{gap}$ and $\hbar\omega_b = \hbar\omega_a$.

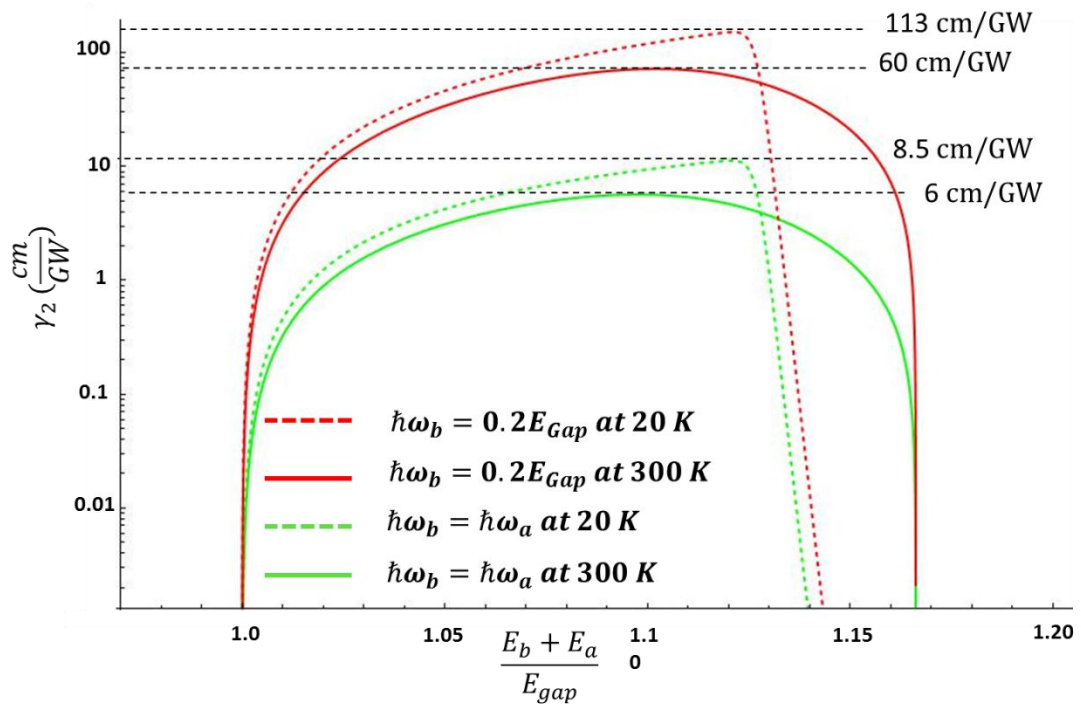

Figure 13- Plot of the 2PG coefficient as a function of signal energy for different $\hbar\omega_b$ energies, 0.2 E_{Gap} and $\hbar\omega_b = \hbar\omega_a$ at 300 K and 20 K for a fixed carrier concentration

Once again assuming a fixed carrier concentration and reducing the temperature to 20 K shows a similar plot of the two-photon gain coefficient, however, with a much sharper drop which is due to the "sharp" Fermi distribution of the excited state carriers. At low temperatures, the carriers are more concentrated near the band edge than at room temperature simply because there is less thermal excitation to other states in the band. At 20 K a peak two-photon gain coefficient of approximately 113 cm/GW is achieved when $\hbar\omega_b = 0.2E_{gap}$ at an energy sum of $1.11E_{gap}$. The degenerate photon pair yields a maximum gain of approximately 8.5 cm/GW for the same energy sum, which means there is an enhancement of a factor of 13 over the degenerate case.

Comparing the gain between the two temperatures, the theoretical gain at 20 K temperature is slightly higher than room temperature which is why in the experiments conducted in this paper we will move from room temperature to 20 K through the addition of a cryostat.

2.5 Free Carrier Absorption (FCA)

The transition from an initial state $|\psi_i\rangle$ to a final state $|\psi_f\rangle$ leads to a population distribution between the involved states. This distribution may induce changes to both the refractive index and absorption properties of the material proportional to the carrier density in state $|\psi_f\rangle$, also known as the excited state. In the case of semiconductor the transition will yield an electron in the conduction band and a hole in the valence band. Electrons in the conduction band can still interact with incident photons by transitioning to a yet higher energy state usually with the simultaneous absorption of a phonon. Holes can also be promoted to higher energy states, predominantly between the heavy-hole (HH) and light-hole (LH) bands as shown in figure 14. The transitions for heavy-hole, light-hole transitions, are more probable than transitions involving electrons in the conduction band because the holes lack the requirement of a phonon to complete the transition and therefore are more likely to interact with incident radiation.

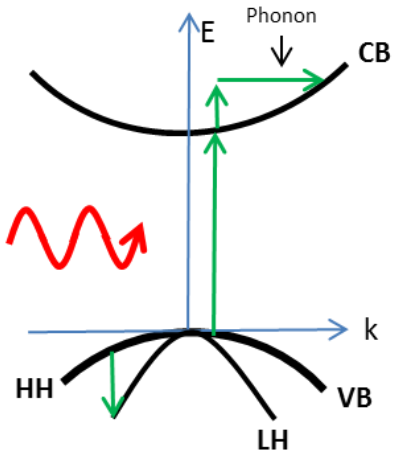

Figure 14 – Hole contribution to FCA, Heavy Hole (HH) to light hole (LH) and the electron contribution to FCA with the simultaneous absorption of a phonon.

Free carrier effects are cascaded $\chi^{(1)}$ processes so they can be modeled classically using the Lorentz-Drude model [38] where the material susceptibility is

$$\chi(\omega) = {\omega_p}^2 \frac{1}{(\omega_0^2 - \omega^2 - i\omega\Gamma)} \tag{2.34}$$

Where the plasma frequency, ${\omega_p}^2 = {Ne^2}/{\varepsilon_0 m}$. Separating out the imaginary susceptibility and assuming that $\omega_0 = 0$ since the resonance frequency for free electrons is zero produces

$$\chi''(\omega) = {\omega_p}^2 \frac{\Gamma/\omega}{(\omega^2 + \Gamma^2)} \tag{2.35}$$

Where at high frequencies $\chi''(\omega) \approx {\omega_p}^2\Gamma/\omega^3$. Solving for $\alpha(\omega)$ results in

$$\alpha(\omega) = \frac{2\pi}{\lambda}\frac{\chi''(\omega)}{n} \approx \frac{\Gamma}{c}\frac{\lambda^2}{\lambda_p^2} \tag{2.36}$$

The relation 2.36 shows that the FCA coefficient has a square dependence on the wavelength, therefore long wavelength photons, such as the ones that will be used in this experiment, suffer

from free carrier absorption. This derivation of the absorption coefficient for FCA is very much an approximation and is only meant to demonstrate the general trend. For a more accurate result many factors need to be included such as the band structure, temperature and momentum conservation [39]. In the case of GaAs the trend is, to some degree, quadratic between 6 and 14 microns for 77 K, and 4 and 7 microns at 300K. Figure 15 shows theoretical plot from Krishnamurthy [39] of the FCA cross section due to both holes (left) and electrons (right).

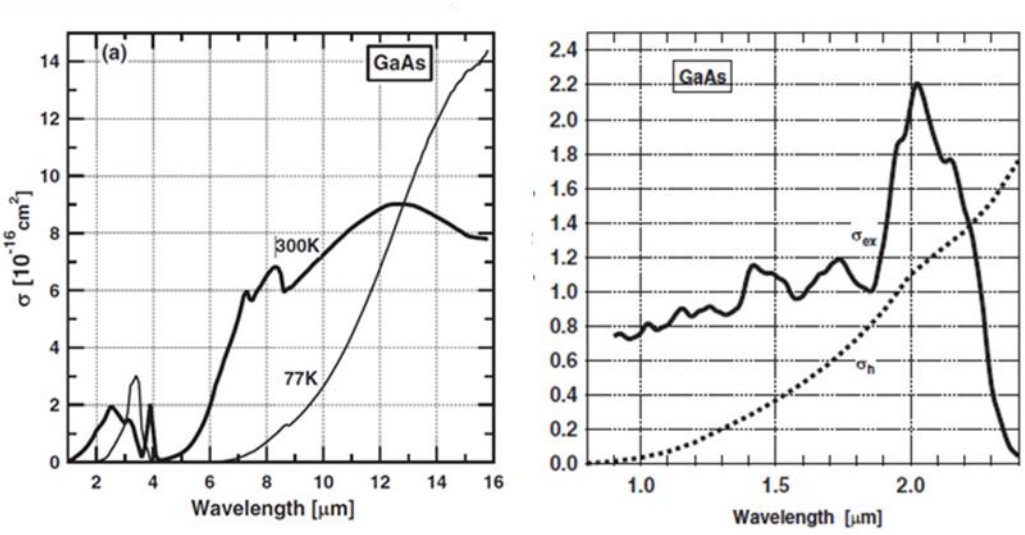

Figure 15 – Theoretical hole contribution to free carrier absorption (Left), theoretical electron contribution to free carrier absorption (Right)[39].

Recently, Peceli [40] measured the FCA cross section in GaAs using both degenerate 2PA and three-photon absorption (3PA) from the Z-Scan method [26] to excite the carriers. Peceli's data corroborates the theory published by Krishnamurthy, showing a somewhat static cross section until at about a wavelength of 2 μm where a spike occurs similar to the hole contribution to FCA plot on the left in figure 15. Figure 16 displays the data measured by Peceli.

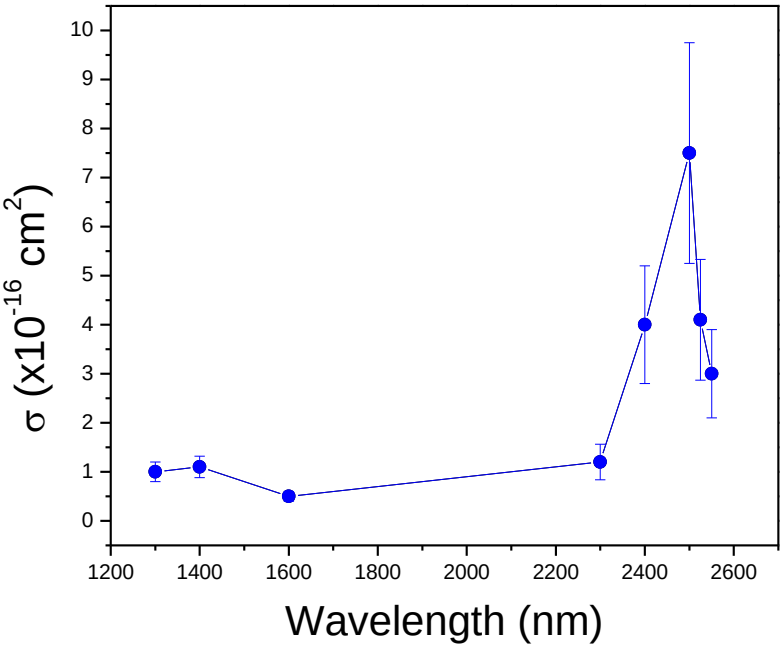

Figure 16 – Measure of the FCA cross section in GaAs by Peceli [40]

FCA induced by 1PA is two cascaded $\chi^{(1)}$ process which is an effective $\chi^{(3)}$ process which means free carrier effects can appear to be 2PA or NLR. Since carriers can be induced from mulitphoton absorption processes, careful thought must be put into the wavelengths such that they are not resonant with energy transitions of the material so that 2PA or even 3PA are mitigated, as this could create substantial carrier concentrations if the irradiance is high. In the case of these experiments smaller FCA will improve the probability of obtaining two-photon emission.

CHAPTER 3: TWO-PHOTON GAIN EXPERIMENT

3.1 Pump-probe Experiment

As mentioned at the beginning of Chapter 2, one of the aspects of nonlinear optics is the interaction between two beams, one beam, the pump, induces a change in the material that the other beam, the probe, experiences. The probe beam is "weak" such that it does not have enough energy to induce any change comparable to the change made by the pump. Possible nonlinear interactions that can be resolved from a pump-probe experiment are ND-2PA [41], reflection [42] and FCA can also be measured due to a population in the excited state from 1PA of the pump.

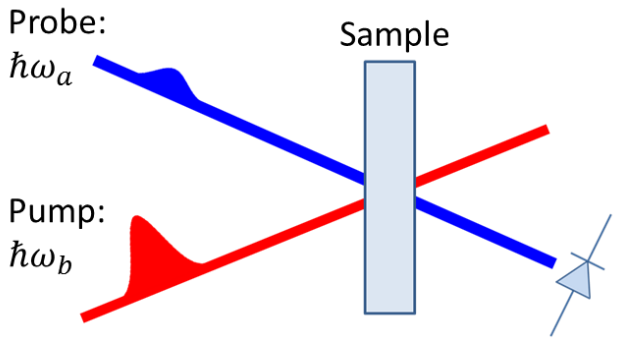

Figure 17 – Pump-probe experiment using pulsed beams, "strong" pump and "weak" probe

For pulsed systems a temporal dimension is added to the experiment since now the probe can be delayed, in time, with respect to the pump. This added time dynamic allows one to measure both instantaneous and long lived effects such as free carrier relaxation times when the probe trails the pump pulse. Of course the maximum temporal resolution depends on the pulsewidth of the beam, meaning the shorter the pulse the more nonlinear effects that can be resolved.

From the equation for the change of irradiance due to 2PA in chapter two, equation 2.11, the rate equations for a two beam pump-probe in a material exhibiting 2PA, 1PA and FCA are

$$\frac{dI(z)}{dz} = -2\alpha_2(\omega;\omega_p)I(z)I_p(z) - \alpha_2(\omega;\omega)I(z)^2 - \alpha(\omega)I(z) - \sigma_{FCA}(\omega)NI(z) \tag{3.0}$$

$$\frac{dI_p(z)}{dz} = -2\alpha_2(\omega_p;\omega)I(z)I_p(z) - \alpha_2(\omega_p;\omega_p)I_p(z)^2 - \alpha(\omega_p)I_p(z) - \sigma_{FCA}(\omega_p)NI_p(z) \tag{3.1}$$

Where the subscript p refers to the pump and no subscript refers to the probe, $\alpha(\omega)$ is the 1PA coefficient, σ_{FCA} is the FCA cross section and N is the number of generated carriers per unit volume.

Assuming no broadening during propagation through the system, Gaussian temporal shaped pulses and an undepleted pump beam with a uniform distribution, Eq. 3.0 can be solved [43] to yield the normalized transmittance of the probe Q, where the energy of the probe after the sample, is normalized by the energy of the probe measured before the sample.

$$Q(\sigma,\tau_d,W,\rho,\Gamma) = \frac{e^{-2\sigma}}{W\sqrt{\pi}}\int_{-\infty}^{\infty} exp\left(\begin{matrix} -\left(\frac{\tau+\tau_d-\rho}{W}\right)^2 \\ -\frac{\Gamma\sqrt{\pi}}{\rho}(erf(\tau)-erf(\tau-\rho)) \end{matrix}\right)d\tau \tag{3.2}$$

σ is the 1PA cross section, $\Gamma = LI_p\alpha_2$ is the two-photon absorption parameter, τ is the time, $W = \tau/\tau_p$ is the ratio of the probe pulse width τ to the pump pulse width τ_p, and ρ is the group velocity mismatch (GVM) defined as

$$\rho = \frac{L}{\tau_p c}\left(n - n_p + \lambda_p \frac{dn}{d\lambda}\Big|_{\lambda_p} - \lambda \frac{dn}{d\lambda}\Big|_{\lambda}\right). \tag{3.3}$$

L is the sample thickness. GVM is due to different phase velocities of different wavelengths due to linear dispersion in a material.

In a two beam pump-probe experiment measuring 2PA, if the probe pulse is delayed with respect to the pump pulse, the transmittance of the probe will follow a cross-correlation between pump and the probe as shown in figure 18. At zero delay the two interacting beams are overlapped leading to a maximum in the 2PA signal, the reduction of transmission due to 2PA, and a minimum in the transmittance. Zero delay refers to the point in time when the pump and probe beams are temporally overlapped at the sample.

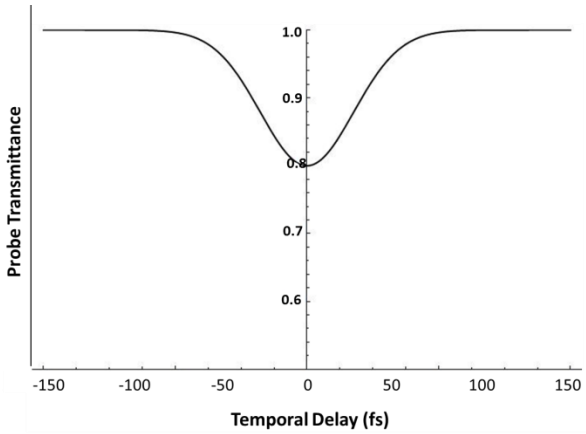

Figure 18-Theoretical pump-probe with a 20% reduction in transmittance due to 2PA.

In a pump-probe experiment the two pulses can, if the sample is thick enough and if the dispersion varies significantly between the two beams, walk off each other inside the sample since each beam has a different phase velocity. The effect GVM has in Zinc Selenide (ZnSe), is shown for three different wavelengths with a pump beam of 750 nm in figure 19 [43].

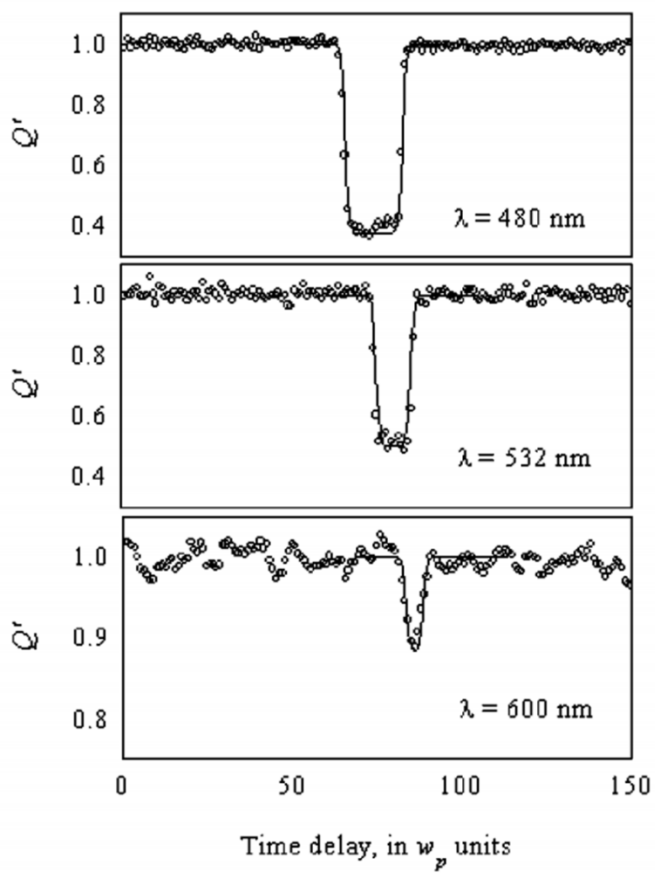

Figure 19-Group velocity mismatch (GVM) in ZnSe [43]

From figure 19, Q' is the nonlinear transmittance normalized by the linear transmittance and w_p is the probe pulse width (HW1/eM of irradiance) which is used to normalize time T where $T = t/w_p$. As shown the transmission is reduced over larger temporal delays as the probe wavelength is tuned farther from the pump wavelength. The 450 nm probe pulse moves slower through the ZnSe slab, this allows the pump pulse to "catch up" to the probe pulse at negative delays and interact with the probe pulse at different spots within the ZnSe sample leading to what appears to be a flattened 2PA signal. The 600 nm probe pulse's group velocity is similar to that of the 750 nm pump pulse and therefore little to no walk off occurs.

The experiment presented in this work utilizes the pump-probe experiment to observe non-degenerate 2PA in bulk GaAs and with the addition of a third beam to create population inversion and observe 2PE. The three beams in this experiment are the mid-infrared pump, ω_p, a near infrared probe, ω and a visible excitation beam, ω_e. Even though this experiment utilizes three beams instead of the standard two, the pump-probe theory remains the same since we are simply using a pump-probe experiment (two beams) on a sample with optically excited carriers.

3.2 Femtosecond Laser

For this experiment, a Clark MXR CPA Series (Model 2010) 140 fs pulsed laser with a repetition rate of 1 kHz was used to supply the necessary beams. The Clark MXR, at 140 fs pulse duration, has an average energy of 1.6 mJ, or 1.6 W in average power, at a wavelength of 780 nm. This corresponds to a peak power of about 10.7 GW**.** The laser contains a resonator that operates at 1550 nm and consists of an erbium doped (Er^{3+}) fiber, pumped by a 980 nm diode operating at 27 MHz. Using periodically poled Lithium Niobate (PPLN) the pulse from the resonator is converted to its 2nd harmonic value of 780 nm. The oscillator is mode-locked through stretched-pulse polarization rotation additive mode-locking [44]. After exiting the cavity, the pulse is then stretched in time using reflection diffraction grating in order to prevent damage of the Titanium doped Sapphire (Ti:Sapphire) gain medium and other optical components. Thereafter, the Pockels cell allows one pulse into the amplifier cavity. There is also an exit port on the case of the laser than can be used to dump out the remaining 780 nm pulses in the cavity, which is what we use to be our excitation in this experiment.

The Ti:Sapphire gain medium is pumped by a frequency doubled, Q-switched, Nd:YAG laser, outputting 532 nm and at a 1 kHz repetition rate. The energy in the Ti:Sapphire media is extracted in about ten passes reaching the 1.6 mJ. Once this level is reached the same Pockels cell that allowed the pulse to enter the cavity now switches the pulse out of the cavity. The pulse is then compressed using a diffraction grating to achieve a pulse width of 140 fs. The method by which a pulse is stretched, amplified and then compressed is known as chirped pulse amplification or CPA [45]. Figure 20 displays the basic layout of the femtosecond laser.

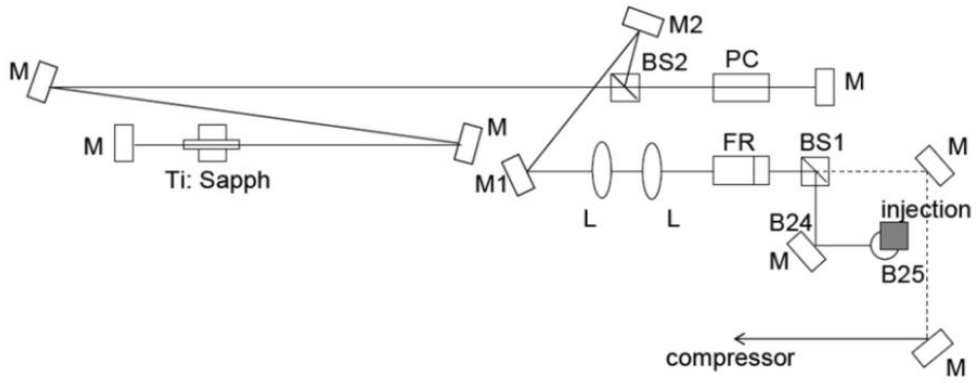

Figure 20 - Layout of the Ti:Sapphire amplifier. L-lens, BS-beamsplitter, PC-Pockels cell, FR-Faraday rotator [36, 46]

3.3 Optical Parametric Amplifier

Two of the beams that are used in this experiment, the infrared pump and probe, are supplied by two optical parametric amplifiers from Light Conversion where the model is the TOPAS 800. Each TOPAS is tunable from 275 nm to 13 μm with an added crystal module to generate the sum and difference frequencies of the signal and the idler. In order to generate this type of tunability the TOPAS splits the 780 nm input beam from the Clark-MXR into three beams, two low energy and one high energy, all at 780 nm, and uses a BBO (Beta-BaB_2O_4) crystal to generate

superfluorescence from one of the low energy beams. In the first stage the superfluorescence passes on to a grating or frequency separator where the signal, ω_s, is selected. The second stage has the signal then pass back through the BBO crystal where it is preamplified and then mixed with the second low energy beam of the 780 nm, ω_p, creating the idler, ω_i such that

$$\omega_p = \omega_s + \omega_i \tag{3.4}$$

In the third stage the signal and the idler pass through the BBO crystal where the high energy beam of 780 nm amplifies the power of both the signal and idler.

BBO is a birefringent crystal so phase matching is controlled by the refractive index of the extraordinary polarized light. In order to control the refractive index the crystal is rotated such that the wave vectors of the pump, signal and the idler sum to zero and it is considered Type-II phase matching since the signal and the idler are two different polarizations. All movements of the delay lines, gratings and crystals are controlled by step motors which the user can control through the TOPAS user software.

To generate the mid infrared wavelengths another crystal is used at the output of the TOPAS 800 that produces the difference frequency of the signal and the idler.

3.4 Complete Setup

Due to the nature of these experiments there were several changes made to the setup. As mentioned in the pump-probe section we use three beams in this experiment. Our excitation beam has a wavelength of 780 nm, our infrared pump is either a wavelength of 4.4 μm or 1.9 μm and our probe is a wavelength of 1050 nm or 1.378 μm depending on the experiment. The complete version of the experiment is shown in figure 21.

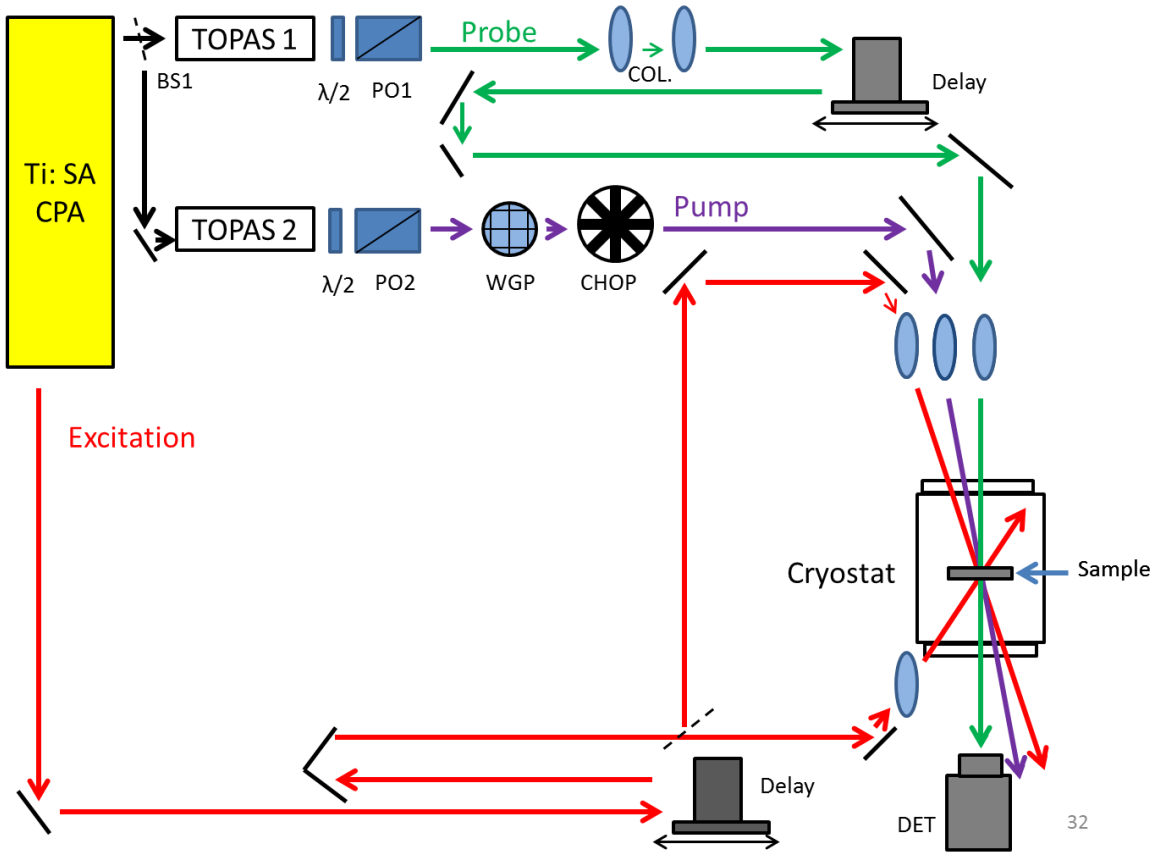

Figure 21 – Ti:Sapphire CPA – Clark MXR Laser Systems, TOPAS 1 and TOPAS 2 – Optical Parametric Amplifiers, λ/2 – Half Wave Plate, PO1 and PO2 – Polarizer, Delay – Corner Cubes on Translation Stages, WGP – Wire Grid Polarizer, CHOP – Chopper Blade, , Sample – GaAs, DET - Detector

The near infrared (NIR) probe beam (Green), exits TOPAS 1 and is passed through a half wave plate and polarizer combination, useful from 700 nm to 1550 nm, to variably attenuate energy of the beam. A long pass filter with cutoff wavelength of 900 nm is placed after the wave plate and polarizer to eliminate the sum frequency of the idler which is nearly collinear with the NIR probe beam, along with some residual energy of the pump. The beam is then passed through a protected silver corner cube set up on a translation stage. This is known as the delay line and the translation stage is moved so that the probe beam can be overlapped in time with the mid

infrared pump beam (Purple) on the sample. The probe beam is then focused onto the GaAs sample.

The mid infrared pump beam, exiting TOPAS 2, first passes through a 1500 nm long pass filter to eliminate the signal. The beam then passes through a KRS-5 Specac GS57000 wire grid polarizer to filter out the second harmonic of the idler, with a wavelength of approximately 2 μm, also exiting TOPAS 2. The wire grid polarizer does filter about 30% of the energy of the pump beam but it eliminates the idler. The pump beam is then focused onto the sample.

The excitation beam exits the MXR laser through an exit port on the side of the laser chassis. The beam is filtered using a 715 nm long pass filter due to the 532 nm also exiting. The 780 nm beam passes through UV enhanced aluminum corner cube mirror on a translation stage. The translation stage is used to help change the path length of the 780 nm excitation beam so that the pulse arrives approximately 200 ps before the probe beam and mid-IR pump beam. The 780 nm beam is focused onto the sample. The point of having the excitation beam arrive 200 ps earlier is to give the carriers enough time to relax to the bottom of the conduction band. However, it must also be shorter than the lifetime of those carriers which is on the nanosecond time scale. More description is given to this in Chapter 4.

The beam splitter in the path of the excitation beam is implemented in order to pump both sides of the sample with the 780 nm beam since the skin depth, at 780 nm is only about 674 nm, see section 3.5, thereby creating more population inversion throughout the sample.

Following the addition of the beam splitters, a cryostat is added to house the GaAs sample and bring it down to cryogenic temperatures. The cryostat is a Cryo Systems head with a Model 22

Helix refrigerator. A CTI Croygenic 8001 controller and 8003 compressor are used to reduce the temperature in the cryostat along with a The Pump Works vacuum pump to pump down the cryostat to the mTorr level. The compressor compresses the helium into a high-pressure state where it is then pushed through the cold head in the cryostat. Once in the cold head the high-pressure helium abruptly expands, cooling the cold head and the flange where the sample is mounted to between 10 K and 20 K. The heated, low pressure helium is then pushed back through the compressor to complete the cycle. A DRC-91C temperature controller was used to control the temperature inside of the cryostat head.

In order to detect the small signals we expect to see in this experiment and eliminate noise from other sources such as the 780 nm wavelength output of the Clark MXR, we use a method known as lock-in detection. In this method we use a chopper system to modulate a beam at some desired frequency. A lock-in amplifier references this frequency so that the only signals that it is sensitive to, are the signals received from a photodetector that are modulated at this particular frequency, which in our case is predominantly the change experienced by the probe due to the infrared pump. However, in these experiments we also modulate the excitation beam so that we are sensitive to changes due to the excitation beam. This method of detection helps to virtually "lock in" on the signal we want to measure. Another advantage is that with lock-in detection, the data can be averaged over some user defined interval which also helps further reduce the noise. For detecting the probe we place a collecting lens behind the exit window on the cryostat to focus the radiation onto a silicon detector with a CREMAT 150 evaluation board and a CR-110 amplifier chip. To detect the mid-infrared pump, a liquid nitrogen cooled Mercury Cadmium Telluride (MCT) detector is used. The detectors connect to a Stanford Research SRS 830 DSP

lock-in amplifier to detect the small signals in these experiments. An MC2000 Thorlabs optical chopper is used to chop the desired beam for detection and provide a reference frequency for the lock-in amplifier. The chopper modulates the beam at $2/7$ of the laser frequency, 1 kHz, which is approximately 285 Hz.

3.5 Sample Production

One of the issues facing this experiment is the creation of a useable sample of GaAs. One of the key goals that needs to be addressed to see lasing, either two-photon or single photon, is population inversion. The pump wavelength of 780 nm, used to create population inversion, has a skin depth of 674 nm, calculated using Beer's Law with an absorption coefficient of 14830 cm^{-1} [47]. In order to see the most 2PE, population inversion has to occur throughout the entire sample which means that the sample has to be approximately a few microns thick if not thinner. Thanks to Dr. Gregory Salamo, from the University of Arkansas we have a 4 μm thick sample of GaAs. The structure of the sample is shown in the following figure

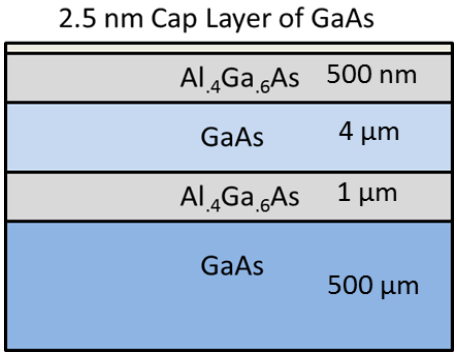

Figure 22 – 4 μm thick GaAs sample structure provided by Dr. Gregory Salamo.

As shown, there is approximately 500 μm of bulk GaAs used as a substrate for the structure which included 500 nm of Aluminum Gallium Arsenide ($Al_{.4}Ga_{.6}As$), 4 μm of GaAs, another 1

μm of AlGaAs and a 2.5 nm GaAs cap layer. The primary purpose of this structure is to protect the 4 4 μm GaAs while remaining transparent to any of the wavelengths we may choose to use for these experiments. The cap layer of GaAs is used to prevent the AlGaAs layer from oxidizing.

In order to etch the bulk GaAs down to the $Al_{.4}Ga_{.6}As$ layer, wet etching is introduced thanks to the help of Dr. Patrick Li Kim Wa. Dr. Li Kim Wa provided Microposit S1805 G2 photoresist to use in order to prevent the GaAs etchant from etching the structure side and only the substrate. The sample is coated in photoresist except for a portion of the bulk GaAs used for the substrate. We decide that in order to maintain some rigidity, we should etch a window into the sample instead of etching the entire sample. There are several benefits about this technique, first, the whole sample is not etched which will make the sample more rigid and easier to handle. Secondly, the window should also make it easier to spatially overlap the three beams in the experiment because the reduction of the probe due to 2PA with the pump will be larger in a thicker area of the material and smaller in the 4 μm window. Once the 2PA signal is found on the thick portion of the sample, we can then translate the sample so that the 4 μm window is at the beam overlap. We make this window by covering the bulk GaAs substrate with photoresist except for a small portion of the GaAs which we leave exposed; our window. The sample is then given a soft bake at 115 °C and is etched using 20 mL of Hydrogen Peroxide, 10 mL of water and 2 mL of Ammonia [48, 49] . Since we are etching 500 microns, the etch rate needs to be high, but also somewhat selective, particularly as the etch continues in order to prevent the etching of the AlGaAs layer. Using the plots in figure 23 is has been determined that the fastest etch rate occurs between a ratio between 5 and 10 of peroxide to ammonia (H_2O_2/NH_4OH) and

the best ratio for selectivity occurs at a ratio of 30. At the beginning of the etching process a ratio of ten is used, but as the bulk GaAs is removed we make new solutions with an increasing ratio of peroxide to ammonia to increase the selectivity.

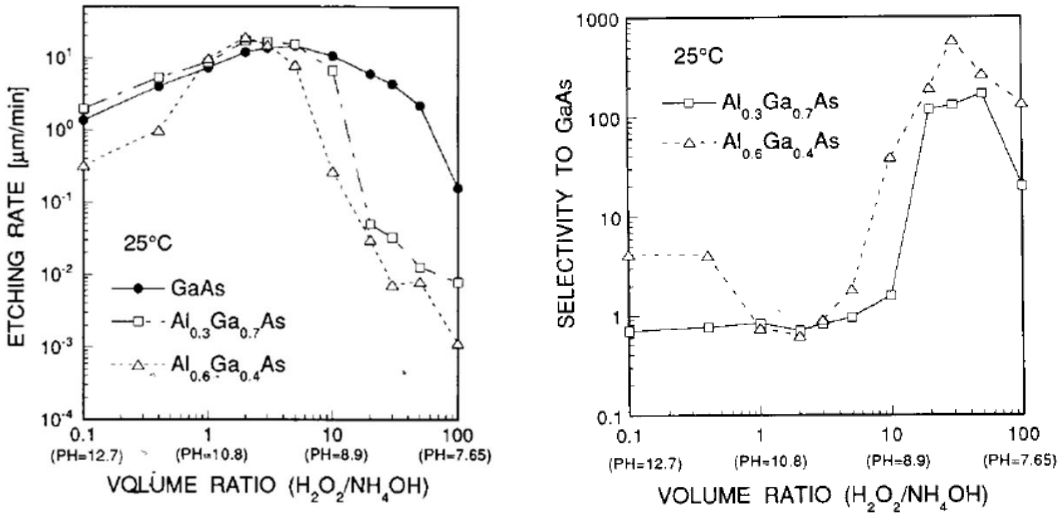

Figure 23 – Etch rate of GaAs (Right), selectivity of etchant to AlGaAs (Left) for given ratios of peroxide to ammonia [49]

At first the etchant works well but what becomes increasingly apparent is the etchant also slowly etches the photoresist. At first this is not a large problem, since the photoresist can easily be dissolved and reapplied. However, as the solution etches deeper in the bulk GaAs it becomes harder to reapply the photoresist to maintain the window. This is due to the non-uniformity of the etched bulk GaAs over several hundred microns and since there is some slope associated with the etching which accumulates over a the course of a deep etch, therefore, the surface tension in the photoresist begins to fail in preventing the liquid photoresist from flowing into window during reapplication. Figure 24 gives a visualization of process.

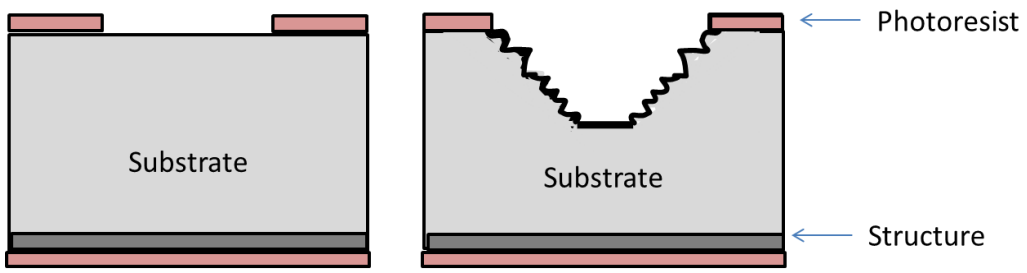

Figure 24 – Etchant undercutting photoresist regions in the bulk GaAs (exaggerated)

This is a direct result of the large thickness that needed to be etched by the solution. To combat this procedural failure, a combination of dry and wet etching is incorporated. The sample is polished down to about 100 μm, then photoresist is applied and a wet etchant is used to etch a window in the sample.

Once the sample is etched we glue the sample to sapphire and then mount it to a copper plate. Norland Optical Adhesive 81 is used for gluing the sample to the sapphire and Lakeshore G-Varnish (VGE-7031) is used to mount the sapphire and GaAs to the copper plate. However, one detriment to using sapphire is the use of the optical adhesive. The optical adhesive and sapphire transmission curves are shown below.

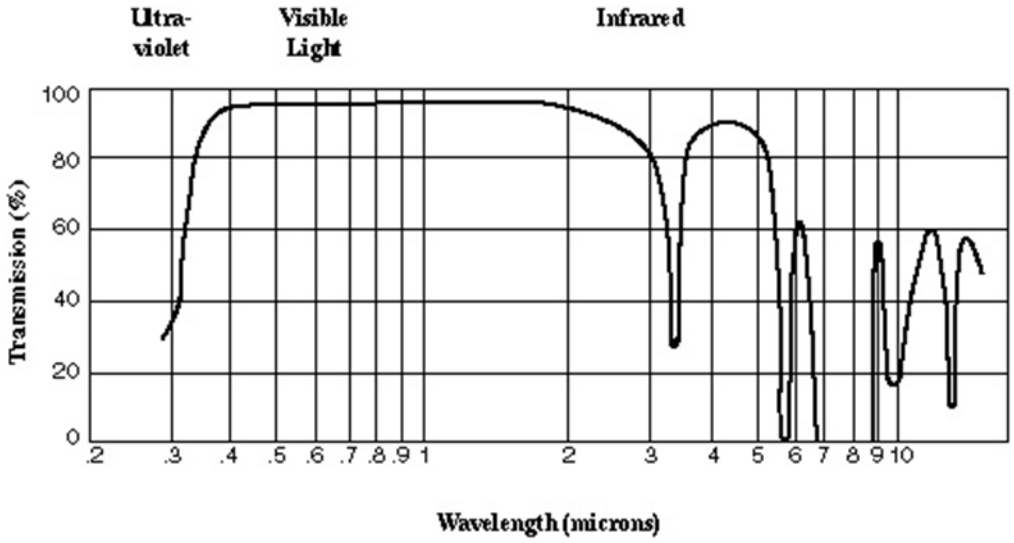

Figure 25 – Norland optical adhesive transmission spectrum [50]

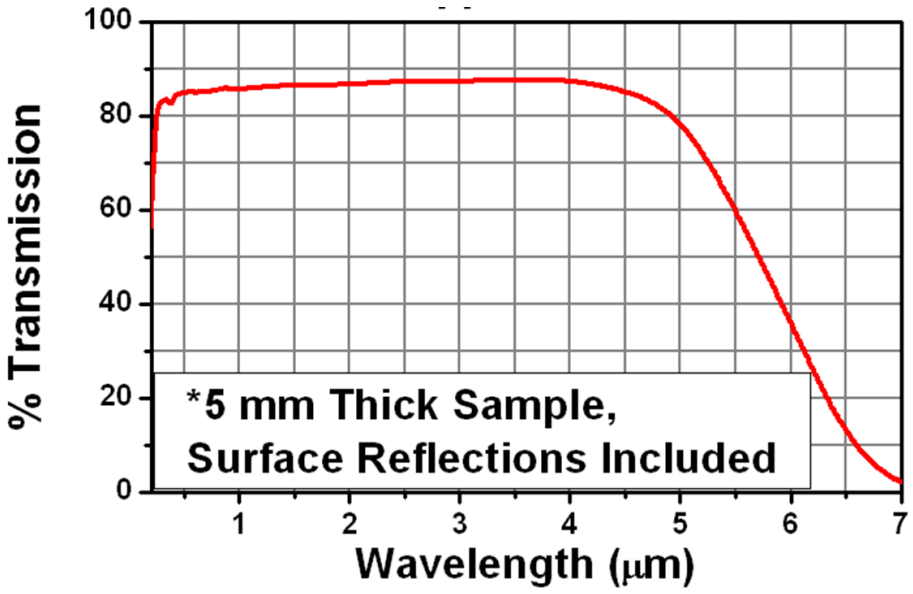

Figure 26 – Transmission spectrum of sapphire with surface reflections [51]

While the sapphire is quite transparent in the region from 500 nm to 4.5 μm, the glue is not. This is one of the ultimate reasons we will settle on a pump wavelength of 4.4 μm, since it was the farthest we can go into the infrared without losing much of the pump energy due to absorption in

the glue and sapphire. Later, we will change to a wavelength of 1.9 μm due to power constraints at the 4.4 μm wavelength, but this too is also chosen with respect to the transparency of the glue.

Considering this, we spent a substantial time developing standalone GaAs samples. We achieve this through virtually the same method described above but instead, before the approximate 100 μm GaAs sample is wet etched, we mount it to a ring using the Lakeshore G-Varnish to glue the edges of the sample to this ring. Then we apply photoresist to form the window and wet etch. Once the etch is completed we use the ring to handle the sample, however, more Lakeshore G-Varnish is added to the edges to solidify the sample to this ring. . In our case the ring was a simple metal washer. Since the sample is standalone, at least in the area of the window, absorption resonances of the substrate or glue do not have to be taken into account, only the absorption resonances of the GaAs and AlGaAs which will allow us to go far beyond the 4 μm pump wavelength, for instance, out to a 10 μm wavelength. This would increase the non-degeneracy and enhance both 2PA and 2PE even more. The one downside to this method is that, while we are not sure of the mechanism, the sample is destroyed when it is put into the cryostat and is cooled. This mechanism could either be due to thermal compression or due to vibrations in the cryostat caused by both the compressor and the mechanical pump. One way to test this would be to only glue one side of the sample to the ring as opposed to what we initially did which was glue both sides to the metal ring. Allowing one side to hang freely should help reduce strain induced by thermal compression but unfortunately we had destroyed our remaining samples before this could be tested. If the damage is being caused by vibrations, then there is not much we can do other than by simply purchasing a new cryostat that has better vibration control.

A linear transmission measurement between the wavelengths of 700 nm and 3 μm is performed on the sample using a Carry 500 Spectrometer. The linear transmission of 4 μm GaAs on sapphire and free standing are shown in figure 27. The band gap is approximately 870 nm (1.425 eV) at 300 K where, on the graph, the transmission spikes which agrees with Sturge [52] in figure 28.

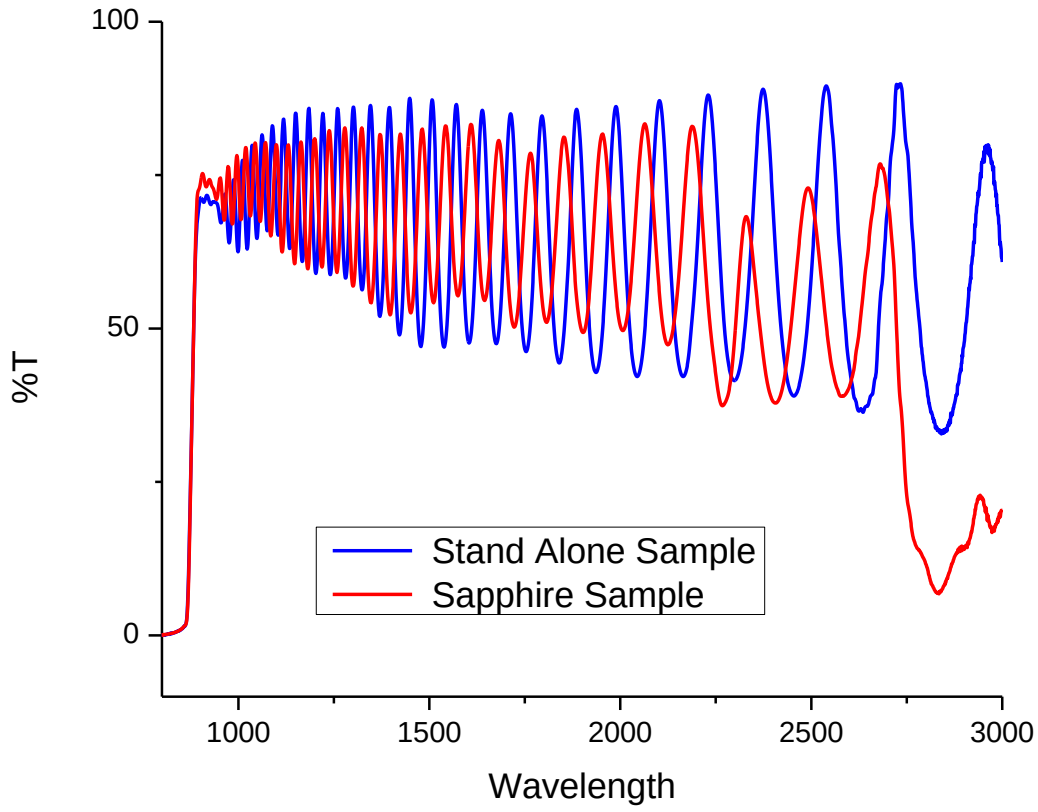

Figure 27 - Linear transmission spectrum of 4 μm standalone GaAs (Blue) and GaAs on a sapphire substrate (Red)

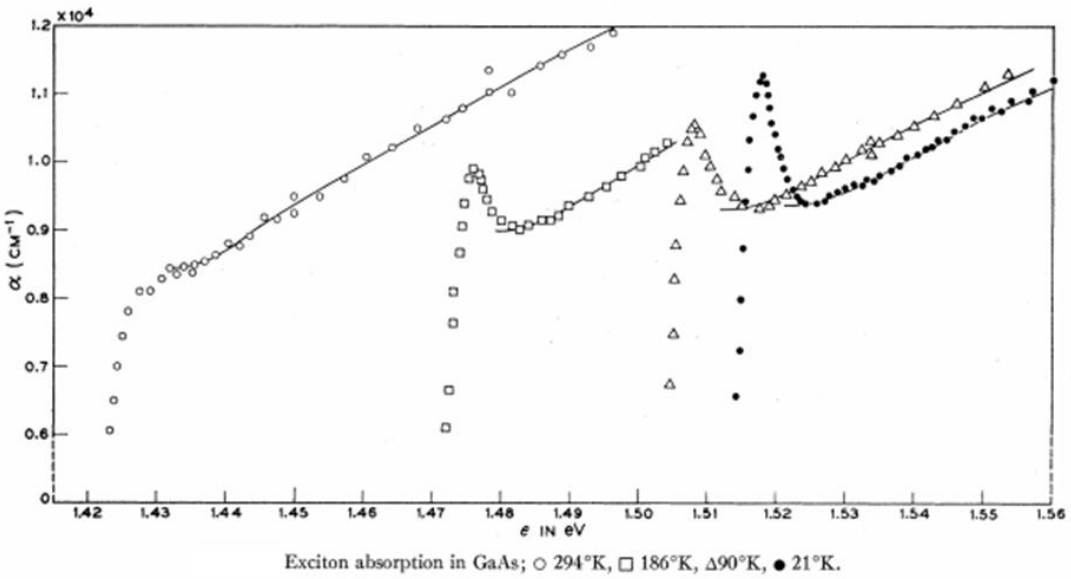

Figure 28 – Absorption spectrum of GaAs at different temperatures demonstrating the band gap energy [52]

From the graph it can be seen that the sapphire sample has a reduction in transmission at a wavelength of approximately 2250 nm with another large drop in transmission at about 2850 nm. These reductions are from the optical adhesive which starts absorbing [50] around a wavelength of 2200 nm. Once the spectrum is taken we model the oscillations to determine the thickness calculated.

The oscillations are a result of the GaAs sample acting like a Fabry-Perot resonator, with certain wavelengths able to resonate within the structure leading to peaks in transmission. Using a thin film stacking model, the transmission spectrum can be calculated and the thickness can be determined. The thin film stacking model is described as the product of the transmission matrixes for each of the individual layers in the sample, such as those shown in the figure below.

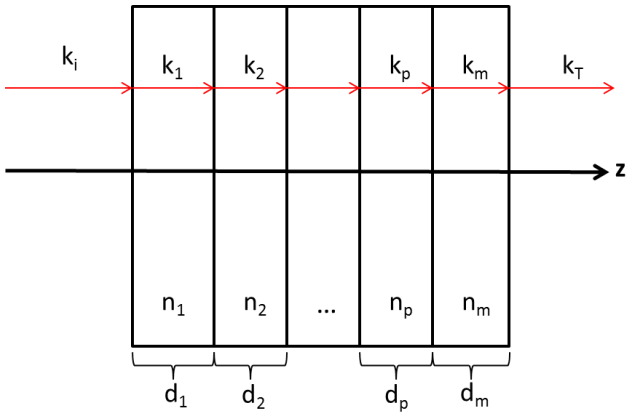

Figure 29 – Thin film stacking diagram

$$[T_p] = \prod_{p=1}^{M} \begin{bmatrix} cos(\delta_p) & isin(\delta_p) \\ ik_p sin(\delta_p) & cos(\delta_p) \end{bmatrix} \tag{3.5}$$

Where p represents the pth layer in the material, k_p is the wavevector in the pth layer normal to the sample, and $\delta_p = k_p d_p$ where d_p is the thickness. We use these matrices to describe the possible five layers in the GaAs sample: a layer of bulk GaAs, then a layer of AlGaAs, then the 4 μm GaAs layer, the second layer of AlGaAs and the cap layer of GaAs (see figure 22). The thicknesses can then be tweaked to match up the peaks and valleys between the calculated transmission spectrum with the measured transmission spectrum. Below is the transmission data of our stand alone GaAs sample (blue curve in figure 27) acquired by the Carry 500 spectrometer and is the green curve, and the thin film stacking model is the blue curve.

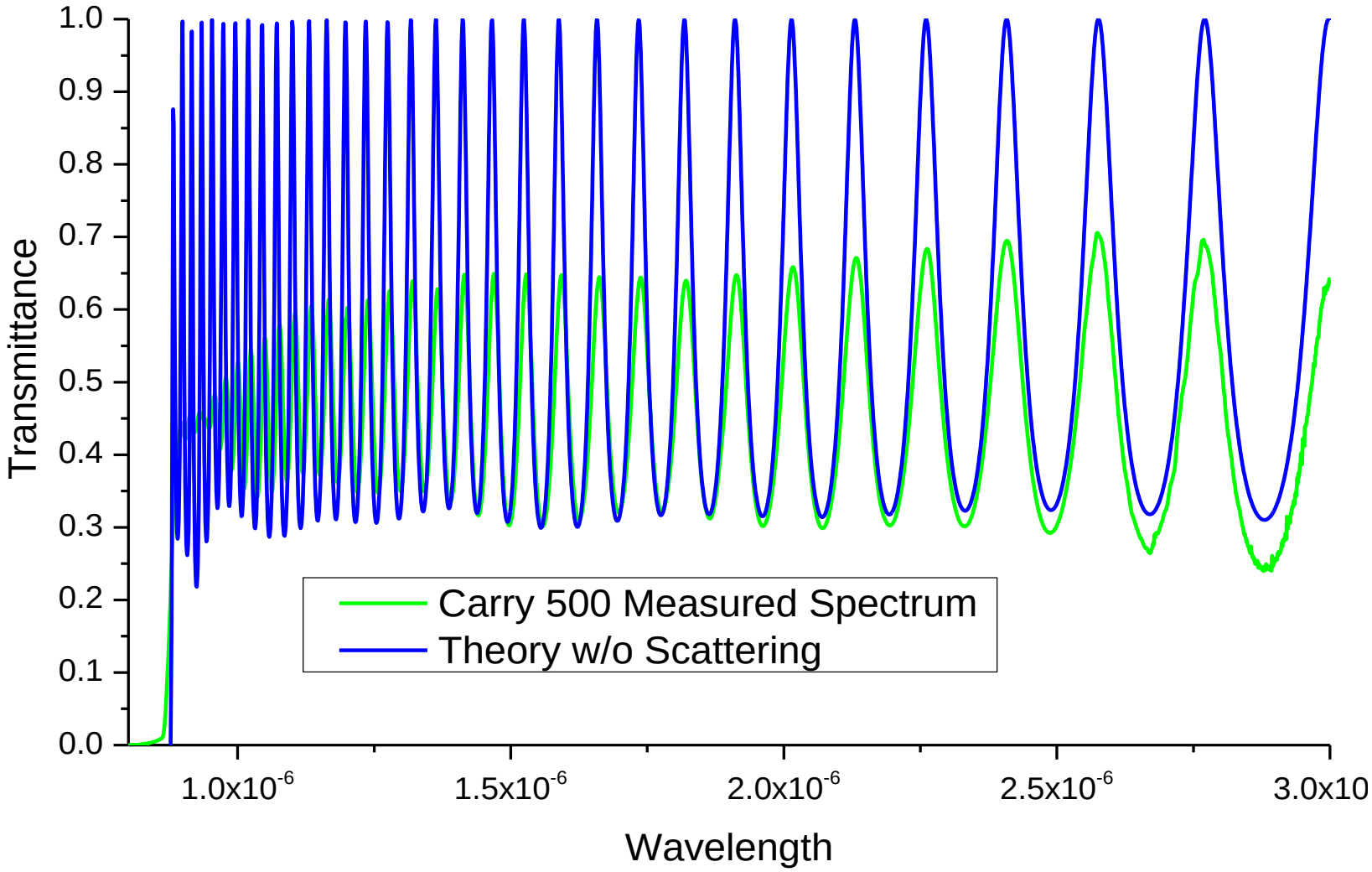

Figure 30 –Transmission as a function of wavelength for the thin film stacking model (Blue) and the spectrum of the GaAs sample measured by the Carry 500 (Green)

We only get the calculated transmission curve to match up with the measured transmission curve when the associated thicknesses of the layers are as follows: no bulk GaAs, followed by 960 nm of AlGaAs, 4 μm of GaAs, 500 nm of AlGaAs and then the 2.5 nm GaAs cap layer. These results seem completely reasonable since it is entirely possible that in the process of etching the bulk GaAs we also etch off 40 nm of the AlGaAs layer. The amplitudes of each the peaks, however, do not match up. We attribute this to the fact that when we put this in the spectrometer we measured a spatial average of the transmission leading to reduced peaks but similar valleys since our sample is not perfectly smooth like the thin film model assumes. We can see that the sample is in fact not smooth in pictures we have taken using a microscope at different magnifications.

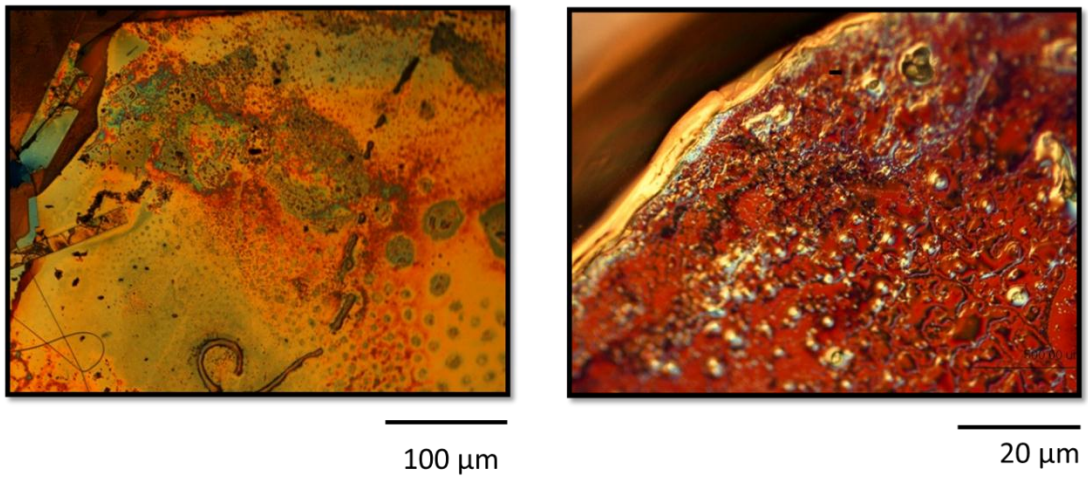

Figure 31 – Photographs of the GaAs sample at 5x (right) and 20x magnification (left)

We see from the photographs, particularly the left, that there are different colors which indicate that there are different thicknesses of the AlGaAs layer which would lead to a spatial dependence on the transmission of a particular wavelength. The photograph on the right shows a closer view of the rough AlGaAs surface.

CHAPTER 4: 2PG EXPERIMENTAL RESULTS

4.1 Experiment Introduction

As mentioned at the beginning of this paper there are three types of 2PE: spontaneous, singly-stimulated and doubly-stimulated. Spontaneous 2PE has been studied in hydrogen [53] and deuterium atoms [15], and singly-stimulated 2PE was studied in vapors such as potassium [17], and recently in semiconductors [24]. Doubly-stimulated 2PE has been the most elusive of the three types and has only been observed by a few groups Loy [20], Pfister [54], Mossberg [14, 55], and Nevet et al. [25] and in those experiments, the stimulating beams were either nearly or completely degenerate. In this experiment we have set out to see ND-2PE in GaAs in the hopes that, similar to the orders of magnitude enhancement ND-2PA exhibits compared to D-2PA, 2PE will also have enhancement due to the non-degeneracy of the stimulating beams. In this regard, we have chosen to use the pump-probe technique with the addition of a third beam to optically excite the GaAs sample.

4.2 Determining the Pump and Probe Wavelengths

This pump-probe technique, discussed in chapter 3, uses a non-collinear geometry between the three beams in order to more easily overlap the beams and adjust the spot sizes with several different frequencies. The first beam in this experiment is the excitation, with a wavelength of 780 nm and a pulse width of 200 ps. It is a fixed excitation, meaning it cannot be tuned to different wavelengths. It arrives at the sample approximately 200 ps before the pulses of the other two beams in these experiments. This is done in order to provide the excited carriers enough time to relax down to the bottom of the conduction band. How we determined this delay value will be discussed momentarily.

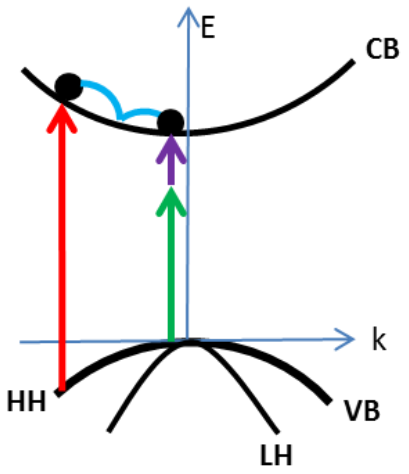

Figure 32- Excitation beam pumping carriers to the conduction where the carriers relax to the bottom of the conduction band after which the probe and infrared pump arrive.

The second beam in this experiment is the infrared pump. In determining the wavelengths of the pump two criterions needed to be satisfied, first, it has to be substantially less than the band gap in energy and secondly, in order to enhance the 2PG, we want it to be out as far into the infrared so the pump and probe can be as non-degenerate as possible. Based on the transmittance curves of the optical glue and sapphire substrate we determine that the pump wavelength to be 4.4 μm. Furthermore, the 4.4 μm pump beam is also at a minima in the FCA contribution due to holes in the model by Krishnamurthy [39], see figure 15. Later in the experiment we change the pump wavelength to 1.9 μm due to energy considerations since we only have 500 nJ at 4.4 μm pump beam but this will be discussed later.

The probe is the third beam in this experiment and is purposely kept weak, around 860 pJ. As mentioned previously, this is to prevent the probe from having any effect on the material. Here the probe is chosen so that the sum of the probe and pump would be close to the wavelength where we would see the largest change in transmittance due to the carriers generated by the

excitation beam. We find this wavelength by pumping the 4 μm thick GaAs sample with 183.5 nJ of 780 nm and probing it with wavelengths around the band gap of GaAs, in 5 nm increments from 800 nm to 885 nm, figure 33 shows the plots of 820 nm, 860 nm and 875 nm. Figure 33 shows that before zero delay the probe is linearly absorbed by the material. At zero delay the probe and pump arrive at the front face of the GaAs sample at the same time, and we see the change of transmittance of the probe rise sharply indicating more probe energy is making it through the sample due to the change induced by the excitation beam. The probe transmittance increases for some time giving us the peak in delay. We attribute this slow rise in transmittance after zero delay to carrier relaxation, see figure 32, as well as carrier diffusion in the 4 μm thick GaAs sample which should take on the order of a 100 ps. As carriers relax to the bottom of the conduction band and fill the states, the probe becomes more transparent because the density of electrons at the bottom of the conduction band increases, decreasing the probability of linear absorption. As the delay becomes longer, beyond the peak, the carriers recombine and the probe begins to be linearly absorbed again.

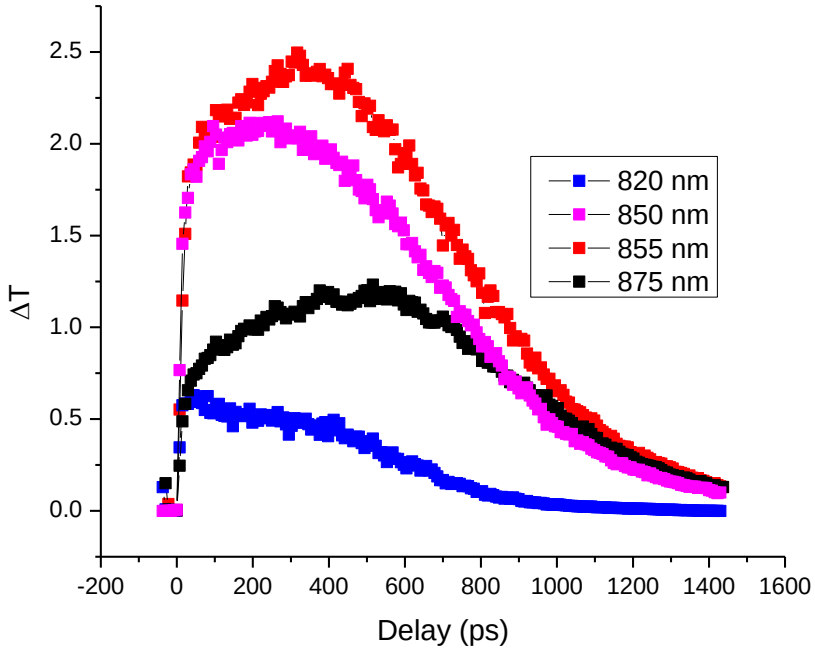

Figure 33 - Change in the linear transmittance of different probe wavelengths due to the excitation beam with respect to the delay of the probe

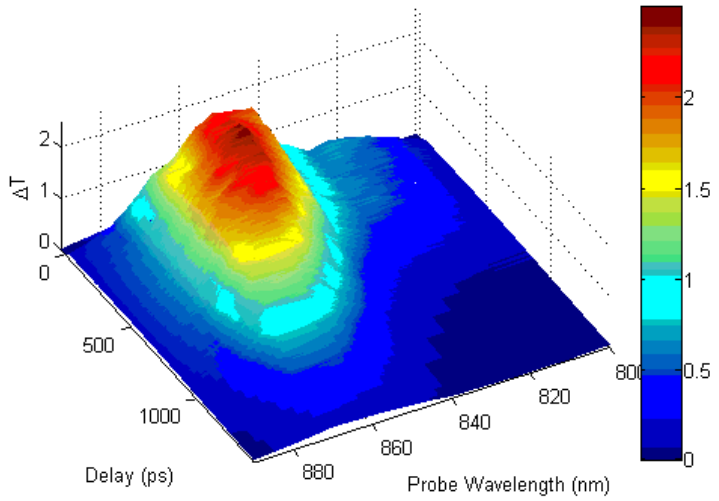

Figure 34 - 3D plot of the change of transmittance as a function of delay of the probe and probe wavelength

From figure 33 we measure the peak in the change of transmittance of the probe to occur around 855 nm at a delay of 316 ps. With this information we determine the probe to be 1060 nm such that the sum of the probe and 4.4 μm is approximately 855 nm. However, 1060 nm is really close to the tuning curve of the TOPAS 800 so to reduce noise and increase stability we reduce the probe to 1050 nm which along with the 4.4 μm pump is about the photon energy of 850 nm. There is minimal change in the results between 850 nm and 855 nm as shown in figure 33 however; the peak delay is now 200 ps which is why we set the excitation pulse to arrive 200 ps before the pump and probe.

Along with this preliminary experiment, there were some FCA measurements that were performed by Himansu Pattanaik and Dmitry Fishman using a 780 nm pump and a 4.4 μm probe in a 4 μm thick GaAs sample.

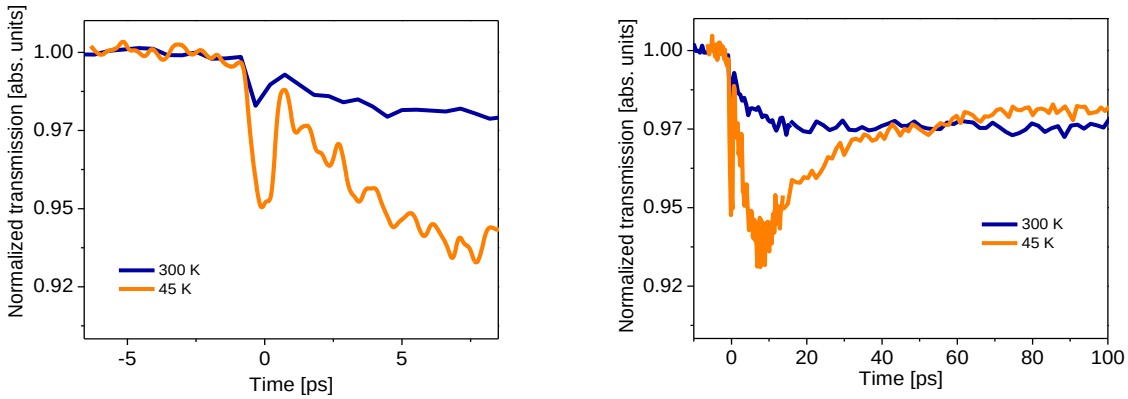

Figure 35 – FCA measurements of 4.4 μm probe with a 780 nm pump at 300 K and 45 K in GaAs at two different time scales

In the plots shown above in figure 35, FCA was measured at two different temperatures, 300 K and 45 K. The two graphs are of the same data set; the right is just a longer time scale. At room

temperature it was found that the transmittance of the 4.4 μm infrared probe decays on the time scale of ~20 ps due to carriers generated by the 780 nm pump. The lack of instantaneous absorption feature we once again attribute to carrier relaxation. This reduction in the transmittance levels off and is maintained for over 100 ps. At cold temperatures, at a delay of 10 ps, we observe a much larger dip in the transmittance of the 4.4 μm due to a larger concentration of free carriers near the band edges. The peak then decays in about 50 ps to a steady state level of transmittance comparable to the steady state transmittance produced at room temperatures. Both plots in figure 35 display a dip in the transmittance of the probe at zero delay. This at first was considered to be 2PA in the AlGaAs layer of the sample since the band gap of the AlGaAs with a 40% concentration of aluminum at 45 K is 2.035 eV [56-58], however the sum of the pump and probe wavelengths is 1.87 eV which probably is not close enough to expect any 2PA.

4.3 Doubly-stimulated 2PG Experiments

With the pump (4.4 μm) and probe (1050 nm) wavelengths decided, we begin the three beam pump-probe experiment. Starting at room temperature using a 4 μm thick sample of GaAs, we measure the reduction of the probe transmittance with and without the excitation. Furthermore, in this measurement we are modulating the pump with the chopper thus we are sensitive to the changes induced by the pump. It should be noted here that the reduction in transmission of the probe due to ND-2PA will be referred to as the 2PA signal.

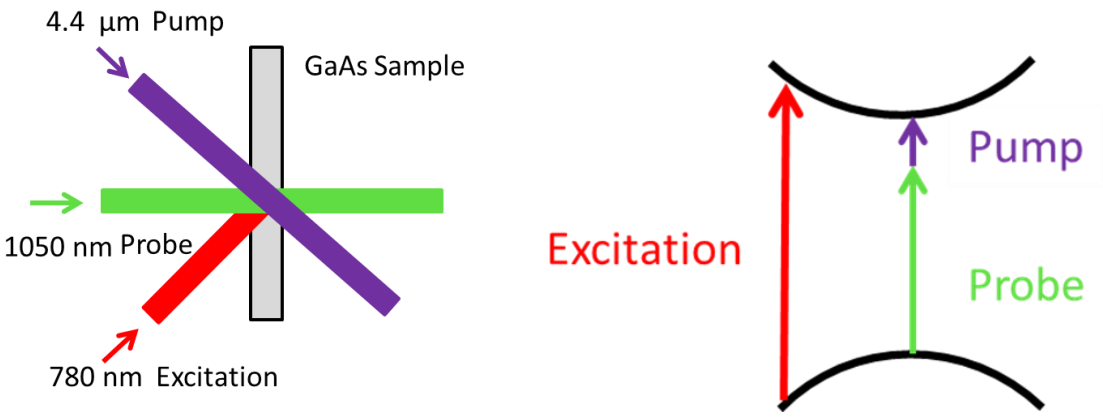

Figure 36 – Excitation beam 780 nm, infrared pump at a wavelength of 4.4 µm and the probe wavelength of 1050 nm

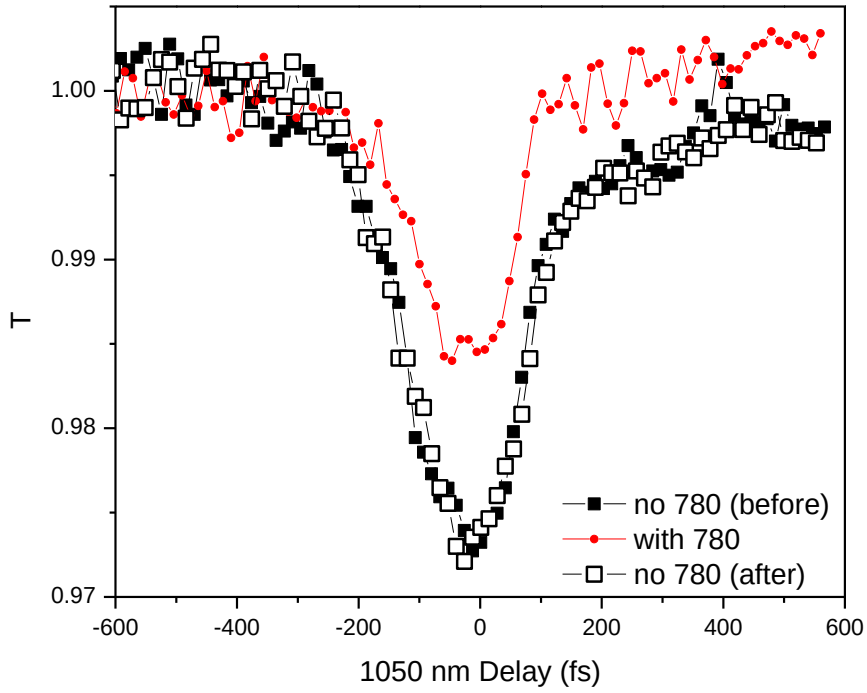

Figure 37 – 2PA signal of the pump and probe (black), reduction in the 2PA signal due to the 780 nm beam (red) in a 4 µm thick GaAs Sample

In figure 37, without the 780 nm excitation, the black curves show reduction in the probe transmission of about 3% due to ND-2PA when the pump and probe are overlapped. When the excitation is incident on the sample we see a change in the 2PA signal of about 45%. This is the type of result we have been hoping for, because if we see a reduction of the 2PA signal due to fewer electrons in the valence band we could possibly reduce the 2PA to the point of bleaching the material meaning two-photon transparency and eventually increase the excited carrier density even more to observe more than 100% transmission, meaning 2PE. We measured the signal without the excitation beam again to make sure the sample was not being damaged by the excitation beam.

We then do the same experiment on a 365 μm thick sample of bulk GaAs while modulating the pump yielding the curves shown in the following figure.

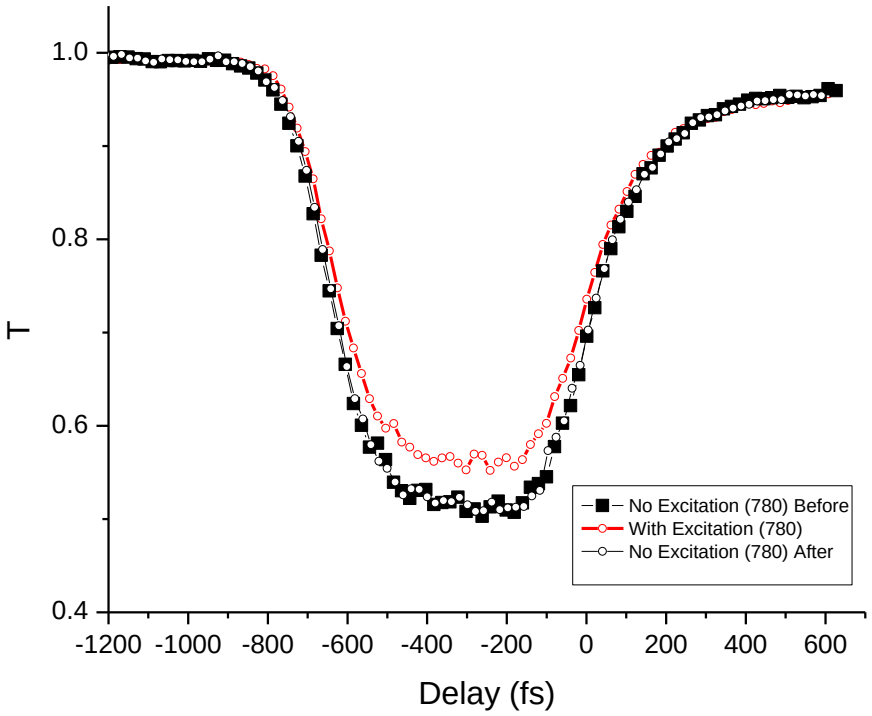

Figure 38 – 2PA signal of the pump and probe (black), reduction in the 2PA signal due to the 780 nm beam (red) in a 365 μm thick GaAs Sample

In figure 38, without the excitation beam there is a 50% reduction in the transmission of the probe due to ND-2PA with the pump. With the excitation beam irradiating the sample, we see approximately a 10% change of the 2PA signal. The flat top 2PA signal is a result of GVM, therefore at about -875 fs delay; the pump pulse begins to overlap the probe pulse at the back of the sample since the pump beam travels faster through the sample due to smaller dispersion. At zero delay, the pulses begin to overlap in the front of the sample. In the 4 μm thick sample we do not see effects of GVM, only a cross-correlation of the pump and probe at zero delay since the spatial widths of the infrared pump and probe are approximately 45 μm which is far larger than our 4 μm thick sample. This also explains why we see a much larger change in the transmittance

because in the 4 μm thick sample only a small portion of each of the pulses is overlapped in the sample so the reduction in the transmittance is less in the thinner sample.

It is worth noting here that the spot size of the 780 nm excitation beam at the sample is approximately 274 μm which is about four times larger than the probe (≈ 70 μm) and 2.5 times larger than the pump (≈ 100 μm). The reason for this is to make sure both the pump and probe can be overlapped on the sample where there is population inversion. Secondly, the energy of this excitation pulse is on the order of 10's of μJ which will damage the sample if it is focused enough. We find this damage threshold to be about 6 μJ at a spot size of 274 μm which gives approximately a peak irradiance of $22.6\ \mathrm{MW/cm^2}$ and peak fluence of $3.1\ \mathrm{mJ/cm^2}$. Our excitation beam is really three pulses separated in time by 10 ns instead of one pulse so the ratio of the peaks is used to determine the peak irradiance from the last pulse which is the pulse we use to excite the carriers.

Figure 38 indicates that 2PA is being reduced throughout the entirety of the sample which is odd. We are not entirely sure whether this reduction in the 2PA signal in figure 38 is a result of a change of α_2 due to a diffusion of carriers throughout the sample or FCA of the infrared pump at the front of the sample, so to determine which was the dominant effect, we decided to irradiate the back of the sample. Irradiating the back of the sample should isolate the depletion of our pump from FCA only to the region where carriers existed which would appear only in the area that was irradiated, thereby reducing the FCA effect on the 2PA signal throughout the entirety of the 365 μm GaAs sample. If the reduction is due to carrier redistribution through the sample,

which is unlikely given the thickness, we should see the same type of reduction of the 2PA signal.

We test this idea on the 365 μm sample, except this time we do not modulate any of the beams so that our probe is sensitive to all the effects on its transmittance particularly FCA and 2PA. Looking at figure 39, the results show, what at first glance appears as, a slight reduction of the probe signal independent of delay due the addition of the excitation pulse (red curve) compared to without the excitation beam (black curve). We attribute this to FCA of the probe since it is a small reduction and FCA due to the excitation pulse would be independent of delay as is shown in figure 39. However, after closer inspection of figure 39, at the back of the sample, corresponding to a -875 fs delay, there seems to be a higher voltage associated with the data points taken with the 780 nm excitation pulse compared to the corresponding data points taken without the excitation pulse. This indicates that at the back when the pump and probe are overlapped, more energy of the probe is falling on the detector with the excitation beam (red) than without (black).

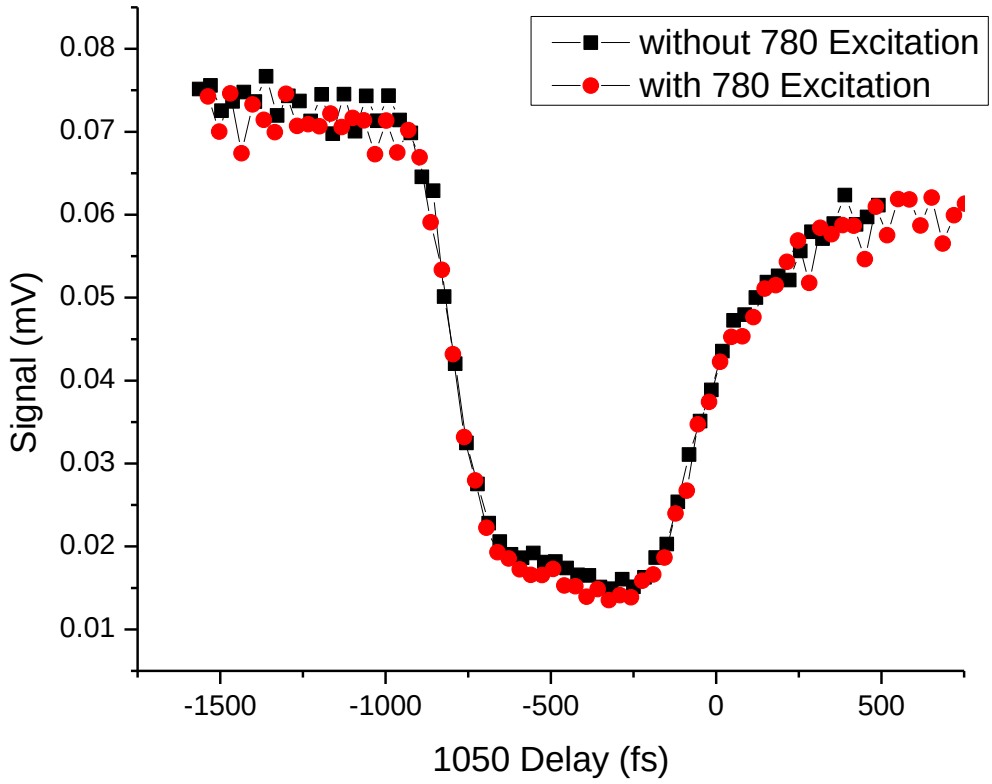

Figure 39 – 2PA signal of the pump and probe (black), reduction in the 2PA signal due to the 780 nm beam (red) in a 365 μm thick GaAs Sample, excitation irradiates the back of the sample

In order to determine if there is something happening at the back of the sample, we take the difference between the signal without excitation (black) and the signal with the excitation (red). Experimentally, we do this by putting the chopper in the path the excitation beam and detecting the probe. This makes us directly susceptible to changes to the probe due to the excitation beam.

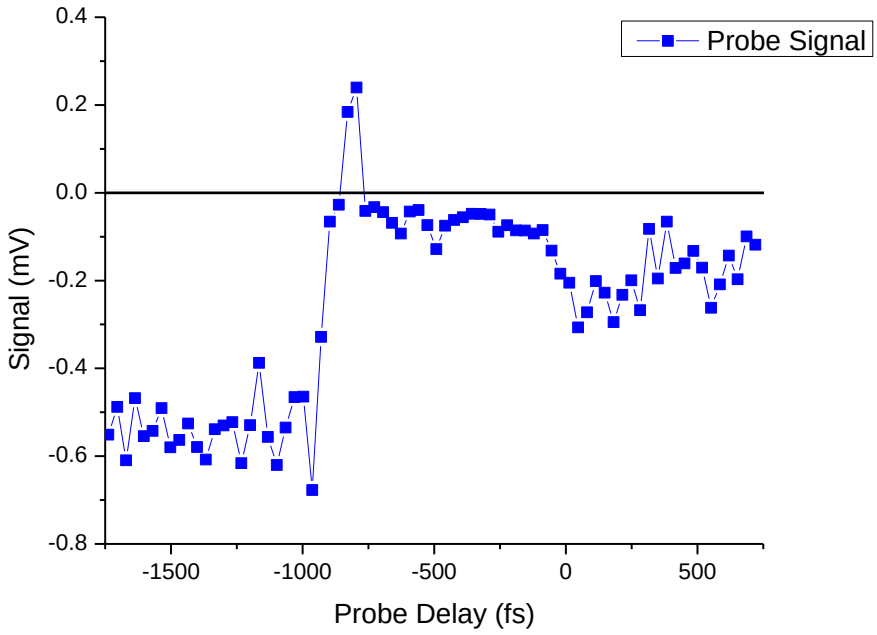

Figure 40-The difference between 2PA signals of the probe and pump with and without the 780 nm excitation beam on the back of the 365 μm GaAs sample (figure 39), measured by chopping the 780 nm and detecting the 1050 nm probe

In figure 40, at long negative delays we detect a negative signal meaning the transmission of the probe is being reduced and since we are modulating the excitation we only observe changes in the probe due to the carriers generated by the excitation, thus the negative signal of the probe is due to FCA. At shorter negative delays, between – 800 fs and -100 fs, we see a small, negative signal. Since we are only sensitive to changes of the probe due to the excitation beam, this near zero value indicates that the change is small. The change is small because the probe is depleted by about 60% at these delays (see figure 39) due to 2PA with the infrared pump and therefore there is less probe energy to be absorbed by free carriers generated by the excitation beam. At -875 fs delay we record a reproducible peak that changes sign. This positive voltage indicates

that there is an increase in the probe energy falling on the detector when the probe is overlapped with the infrared pump at the back of the sample where the carriers are concentrated. Hoping to see a comparable effect in the thin sample, we irradiate the 4 μm thick sample from the back as well. It should be noted here that at his point we were using a different sample of 4 μm thick GaAs since we damaged the previous sample, however, it was cut from the same wafer.

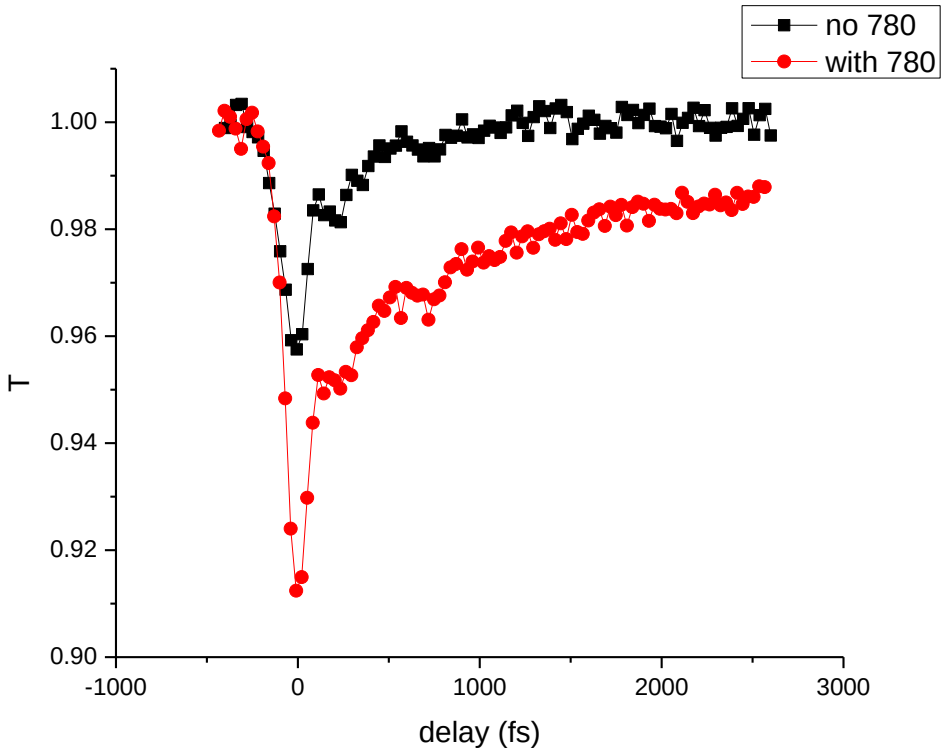

Figure 41 – 2PA signal of the pump and the probe with (red) and without (black) the 780 nm excitation beam

To our dismay what we see is an increase in the 2PA signal in figure 41. At this point we have no explanation for the cause of this. Presumably, the only difference between the 4 μm and the 365 μm sample is the addition of the AlGaAs layers, the sapphire and the optical glue. Unfortunately, at this point we had not yet successfully fabricated standalone 4 μm thick GaAs

samples to see if this was indeed a result of some interaction with the optical glue and or sapphire substrate. From our previous data we expect that this new result is not due to the AlGaAs layers since we previously saw (see figure 37) reduced 2PA when the sample was irradiated from the front with the 780 nm beam.

After considerable thought we now believe that the reduction in the 2PA signal in the 365 μm (figure 38) thick sample is due FCA of the infrared pump beam. We believe the pump is immediately depleted when it arrives at the sample due to the free carriers generated by the excitation, resulting in a reduction of the 2PA throughout the entirety of the sample. This can be seen in the following equations

$$\frac{dI(z)}{dz} = -2\alpha_2(\omega;\omega_p)I(z)I_p(z) \tag{4.0}$$

$$\frac{dI_p(z)}{dz} = -\sigma_{ESA}(\omega_p)NI_p(z) \tag{4.1}$$

Assuming that the probe is primarily depleted due to the ND-2PA and the pump is primarily depleted by FCA, we can obtain the change of irradiances of the pump and probe, equation 4.0 for the probe and 4.1 for the pump, where the subscript p refers to the pump and no subscript refers to the probe. Looking at the change of irradiance equation for the probe, we will see a change of the irradiance of the probe if either $\alpha_2$is changed or if pump irradiance is changed, for instance by FCA. From this we decided to look at what we might expect FCA to be in GaAs at a wavelength of 4.4 μm.

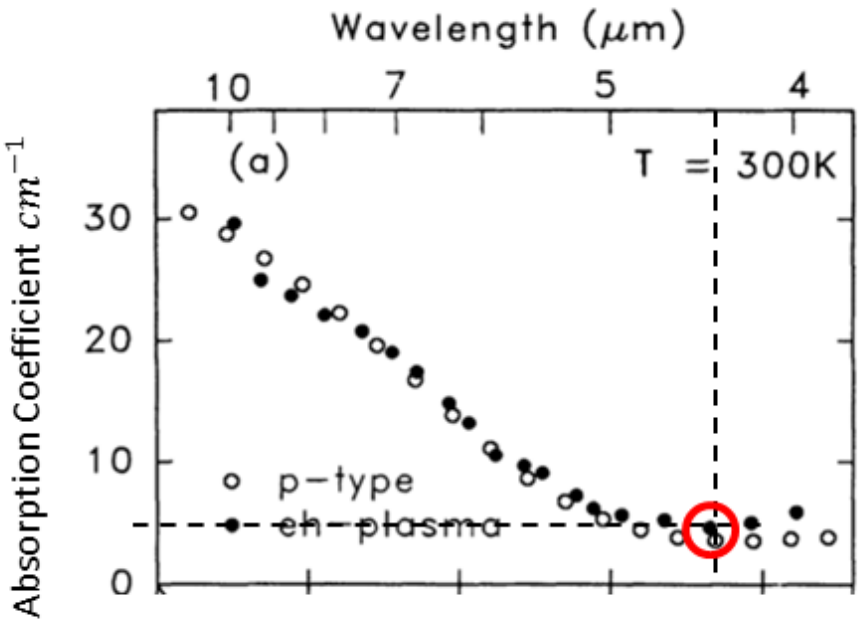

Figure 42 – Free carrier absorption coefficient with 10^{17} cm^{-3} carrier concentration measured by Mayer [59]

Mayer [59] obtained an absorption coefficient of α_{FCA} of 5 cm^{-1} , see figure 42, with a carrier concentration of about 10^{17} cm^{-3}. From our energy of the excitation, 6 μJ, we assume that we have a $1.5 \times 10^{18} cm^{-3}$ carrier concentration where, from the equation $\alpha_{FCA} = \sigma_{FCA} N$, we would presume that our free carrier absorption coefficient would be approximately $\alpha_{FCA} = 75$ cm^{-1}.

Looking back at Krishnamurthy's calculations [39] and the measurements made by Peceli [40] we see that the calculations and the measurements differ by a factor of four. Now if the 10% reduction in the ND-2PA signal in figure 38 is strictly due to the depletion of our infrared pump then we would expect that $\alpha_{FCA} = 200$ cm^{-1}. $\alpha_{FCA} = 75$ cm^{-1} is within the factor of four difference, so the 10% reduction in the ND-2PA signal in the 365 μm sample when the excitation was irradiating the front (figure 38) may entirely be due to FCA.

Since FCA is a linear process, see equation 4.1, then we expect that we would see the same change of our signal in the 4 μm thick GaAs sample. This assumes we are generating the same number of carriers in the 4 μm thick GaAs sample as the 365 μm thick GaAs sample which is reasonable given the skin depth and that we cannot detect our excitation beam behind the sample. However, what we see in the 4 μm thick GaAs sample is a 45 % change in our ND-2PA signal in figure 37. Since the change of the 2PA signal varies so dramatically between the 4 μm thick GaAs sample as the 365 μm thick GaAs sample we may be observing a change of α_2 in the 4 μm thick sample where we have much more population inversion than in the thick sample. Unfortunately, due to minimal energy in infrared pump (500 nJ) we cannot experimentally resolve this change and determine if it is indeed due to a change of α_2.

From this we expect that the change of sign in figure 40, that indicates an increase of transmittance of the probe, could also potentially be due to a change of α_2 since this corresponds to the back of the sample where the carriers are concentrated. Although, it could also be due to FCA of our pump which would increase the transmitted energy of the probe since there is simply less ND-2PA at the back of the sample. Nevertheless, at this point we do not have enough data to conclusively say that is what indeed is happening.

In the next experiment we decid to measure the change of transmission of different wavelengths around the band gap as a function the energy of the 780 nm excitation beam in a 4 μm thick GaAs sample. We did this to see if we could induce 1PG. The results are shown in the following figure.

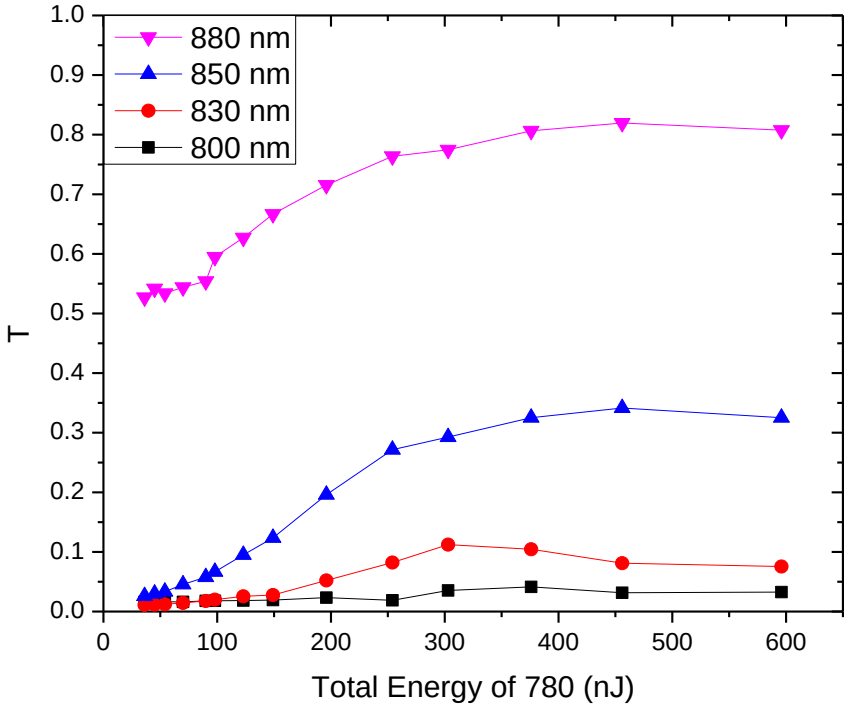

Figure 43 – Saturation of the linear transmission of 800 nm, 830 nm, 850 nm and 880 nm due to increasing energy of the 780 nm excitation beam.

For the wavelengths of 800 nm and 830 nm we see small increases in the transmission, however, for wavelengths of 850 nm and 880 nm we see close to 30% increases in the transmission. From the energies, we use the spot size (≈ 360 μm) and the thickness of the sample to generate the 780 nm photon densities. Using equation 2.33 with the photon densities as ΔN, we can solve for the difference between the quasi-Fermi levels ($E_{F_c} - E_{F_v}$) at different energies of the excitation beam.

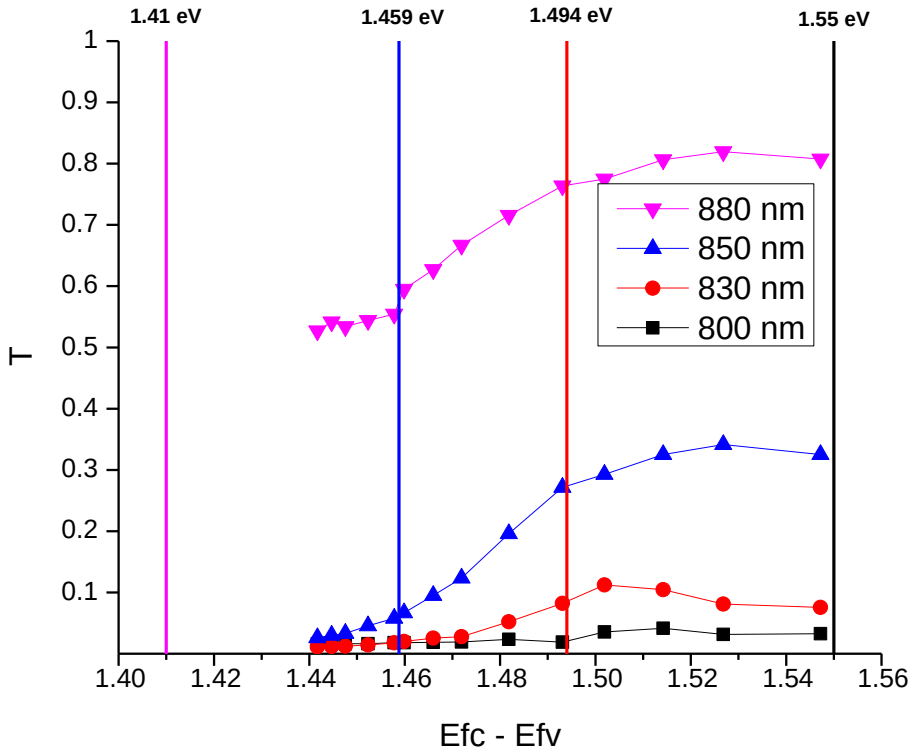

Figure 44 – Transmission of various probe wavelengths as a function of the difference in the quasi-Fermi levels, $E_{F_c} - E_{F_v}$

Figure 44 shows the transmission of each of the probe wavelengths as a function of $E_{F_c} - E_{F_v}$. As the excitation beam increases more carriers are produced filling the bands, therefore, the difference between the quasi-Fermi levels increases. Once the difference reaches the energy of the probe we expect that there should be an increase in the transmission, which is what we see. The vertical lines represent the photon energy of the each of the wavelengths. For 800 nm (1.55 eV) probe, we do not generate enough carriers to really see an increase in transmission, for the 830 nm (1.494 eV) probe we begin to see an increase about where the difference between the Fermi levels is equal to the photon energy. The 850 nm (1.459 eV) probe, shows a large increase

once the difference between the Fermi levels reaches the photon energy, and the 880 nm (1.41 eV) probe is just below the band gap at room temperature, so the difference between the Fermi levels is already larger than the photon energy for even the smallest of energies of the excitation beam that were used. Since the transmission of the 880 nm is high we think we might be seeing gain, so we use our thin film model to determine what the transmission at 880 nm would be without absorption, which we found to be 0.7. The plot clearly goes above 0.7 in transmission which indicates one-photon gain. Furthermore, the model assumes a perfectly flat surface, however, the sample is far from smooth so there should be even more loss. To account for scattering losses we multiply the reflection coefficient, calculated from the thin film matrices, by a factor of 0.7 to match up the theoretical plot with our own transmission data. This gives us a transmission of about 50%. From this we expect that we are seeing either saturation or possibly 1PG at 880 nm.

4.4 2PG at Cryogenic Temperatures

Following these experiments we decide it was time to move to cryogenic temperatures in hopes that with a larger concentration of electrons at the bottom of the conduction band we will improve our chances of witnessing 2PE, or at the very least seeing a reduction in the 2PA signal. First, we measure the change the 2PA signal in the 4 μm GaAs sample as temperature is reduced, once at 300 K (red) and once at 20 K (black). The results are shown in figure 45.

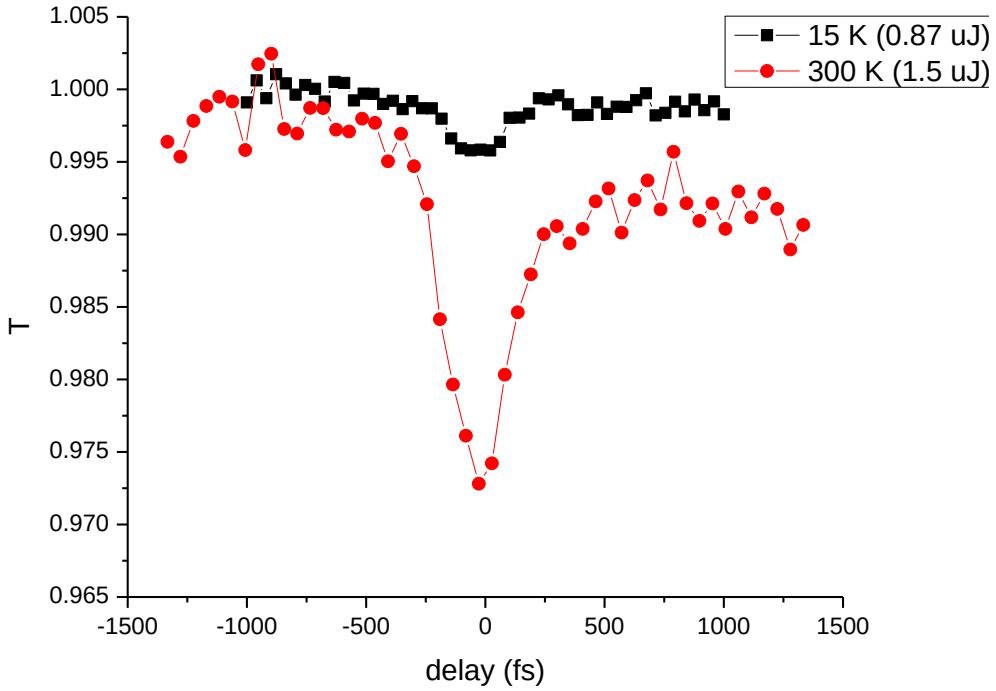

Figure 45 - 2PA signal of the pump and probe at 300 K and 20 K

The 2PA signal at room temperature is about 3%, as the temperature is reduced the band gap increases reducing the 2PA signal to approximately 0.5%. In order to even measure this small of a signal we have to increase the integration time on the SR 830 Lock-In Amplifier to ten seconds. The signal is simply too small to take measurements with since we want to measure the changes of this signal. Therefore, based on what we have learned thus far, which is the dominance of FCA on our infrared pump and the lack of energy of our pump we decide to change wavelengths in hope of increasing the 2PA signal. Thus, we move to an infrared pump wavelength of 1.9 μm and a probe wavelength of 1378 nm, the energy sum corresponds to 850 nm. Our energy increases by over an order of magnitude from 500 nJ to 10 μJ. We figure that

the increase in energy would offset any loss of enhancement by bringing the wavelengths of the pump and probe closer to degeneracy. We also decide, since we have lots of energy at 780 nm, we should split the beam and irradiate both sides of the sample in order to saturate even more of the 4 μm thick GaAs sample.

However, before we move to cryogenic temperatures we measure the 2PA signal of the 1378 nm probe and 1.9 μm infrared pump at different pump energies in the 365 μm thick bulk GaAs sample to find out how much energy we can put on the sample before we induce other effects. There was no 780 nm excitation beam in this experiment. The results are shown below

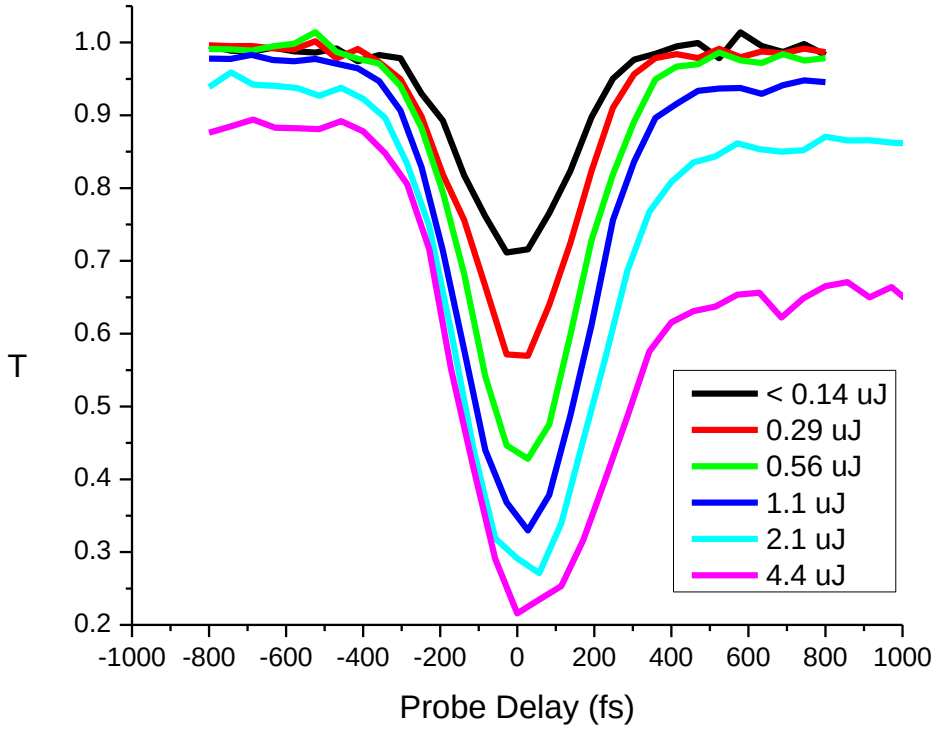

Figure 46 – Reduction of the 1378 nm probe transmission from 2PA of the probe and 1.9 μm pump at different pump energies

As we increase the energy of the 1.9 μm pump the probe transmission is reduced more and more due to increasing 2PA. However, what we also see, though unexpectedly, at energies greater than 0.56 μJ of the 1.9 μm beam, is a tail in the 2PA signal which we presume to be FCA of the probe from three photon absorption of our pump. This, while interesting, is actually a large inhibitor for this experiment since the pump energies we want to use induce FCA. This puts a limit on the irradiance of the pump; a maximum at $39.3\ \mathrm{GW/cm^2}$ with an energy of 560 nJ and a spot size of 78 μm which isn't much better than our 4.4 μm pump which had 500 nJ at a 100 μm spot size for an irradiance of about $21.4\ \mathrm{GW/cm^2}$. After about 2.1 μJ we see a tail at

negative delays indicative of damage. However, since we are setup to run the experiment at 1378 nm and 1.9 μm at cryogenic temperatures we proceed anyway.

With the pump and probe aligned, we align the excitation beam on both the front and back of the 4 μm thick sample. We do this by looking for the reduction of the infrared pump due to FCA induced by the excitation pulse. Once the beams are aligned we measure the change in the 2PA signal due to the excitation beam irradiating the front, back and both sides of the sample at 20 K. The results are shown below.

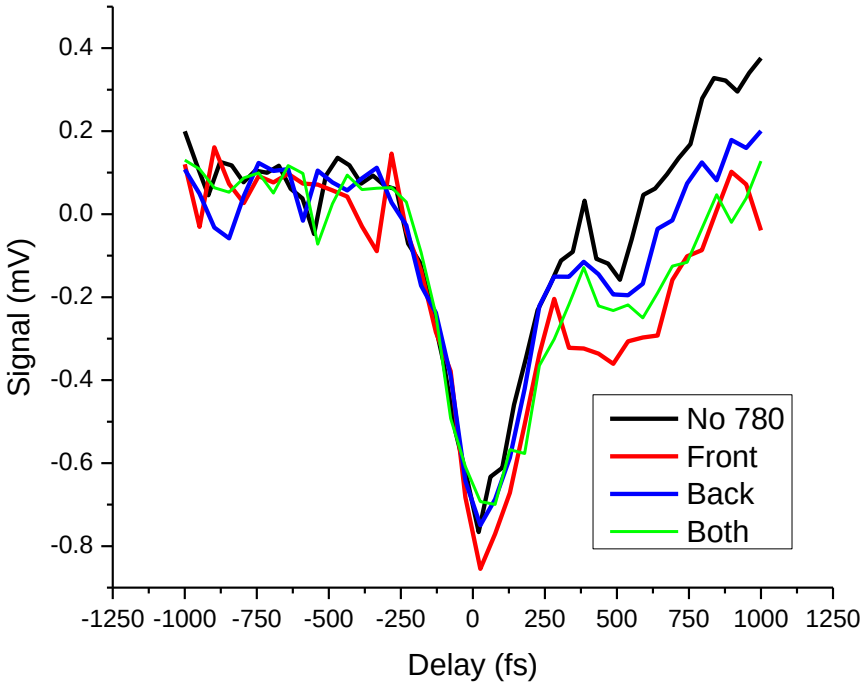

Figure 47 – 2PA signals from a 4 μm sample at 20 K irradiated from front, back and both sides by the excitation beam

The results in figure 47 show there does not appear to be any significant change in the 2PA signal regardless of which face of the sample is irradiated by the excitation pulse. If anything we may be seeing a slight increase in the 2PA signal when the front of the sample is irradiated by the excitation beam. However, since the signal is small, hundreds of μV, what appears to be a small reduction could simply be noise.

CHAPTER 5: CONCLUSIONS AND FUTURE WORK

5.1 Conclusions

The purpose of this work was to observe ND-2PE in GaAs; unfortunately this endeavor has not yet been accomplished. However, this should not detract from the amount that was learned by attempting these experiments particularly when it comes to future attempts at observing 2PE.

We to some degree learned the art of sample preparation, for instance, learning how too effectively polish and wet etch hundreds of microns of a GaAs. Once the sample was etched we learned how to handle these thin samples and mount them to substrates and eventually how to make the GaAs samples free standing. We used thin film stacking matrices to model these thin GaAs samples so that the transmission data could be used to determine the thickness of the sample after etching. The results of this model seem well within reason showing that oscillations in the transmission spectrum match up with the theoretical transmission spectrum when there is no bulk GaAs substrate left and only 40 nm of AlGaAs etched off which is reasonable given the amount of wet etching that is performed.

With these samples we performed non-degenerate pump-probe experiments with the addition of a third beam used to excite carriers. We observed the reduction of 2PA in various experiments and achieve a 45% change of the 2PA signal due to excited carriers in the 4 μm thick GaAs sample. This is much larger than the 10% change due to excited carriers observed in the 365 μm thick GaAs sample which we believe to be due to depletion of the pump due to FCA. This seems to suggest that α_2 could be changing with the addition of excited carriers in the thinner sample but more data is required to confirm that this is indeed a change in α_2.

In the advent of these results we attempted to see 1PE from GaAs which we believe we achieved at 880 nm when excited by the 780 nm pulse though we cannot say for certain. We then reattempted the 2PE experiment at cryogenic temperatures where we achieved more perplexing results that showed little change in the 2PA signal when the sample was irradiated from the back, front or from both sides by the 780 nm excitation beam. The results also display a shoulder at positive delays which has yet to be accounted for.

5.2 Future Work

What we learned from these experiments were two primary necessities that we would need to increase our chances of observing 2PE. These necessities are, one, a sample that is approximately the skin depth of our excitation beam, which is 674 nm. We need this so that population inversion can occur throughout the entirety of the sample increasing the probability of observing 2PE. Secondly, we need more infrared pump energy to help offset the depletion of our infrared pump caused by FCA. Thanks to Dr. Greg Salamo we were recently provided with 1 μm thick GaAs samples. We also recently acquired a 12 mJ laser system from Coherent that should provide enough energy at a wavelength of 4.4 μm to satisfy our energy requirements. So it is well within reach to continue these experiments.

After some calculations we have also come to realize that in subsequent experiments we may have more potential for seeing 2PE at room temperature as opposed to cryogenic temperatures. This is a result of our fixed excitation beam at 780 nm. Previously we had shown that at cryogenic temperatures the 2PG coefficient was higher than at room temperature (see figure 13), however, this was determined by assuming a fixed carrier concentration. This is not the case

though because the band gap changes as a function of temperature. With a fixed excitation beam we generate less carriers at 20 K (dashed curves) and more at 300 K (solid curves) and therefore the 2PG coefficient changes since it is dependent on the carrier concentrations, see Eq. 2.33. Figure 48 shows the 2PG coefficient at 300 K and 20 K for $\hbar\omega_b = 0.2E_{gap}$ and $\hbar\omega_b = \hbar\omega_a$ for a fixed excitation energy of 1.6 eV.

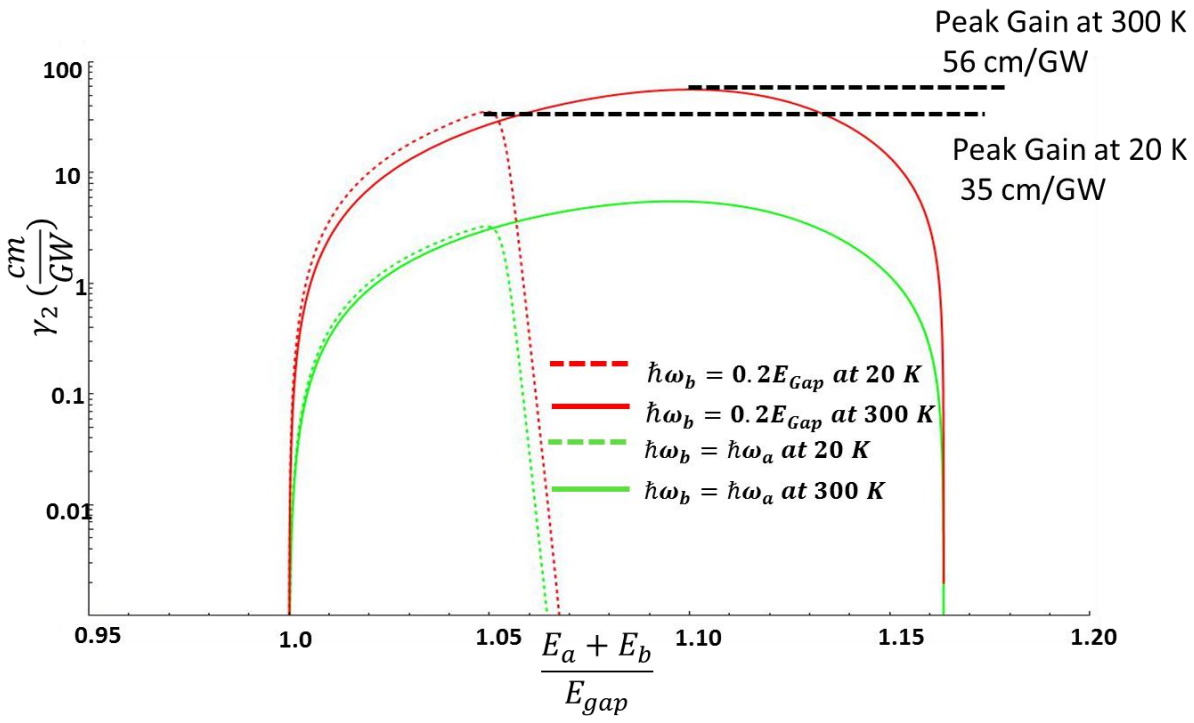

Figure 48 – Plot of the 2PG coefficient as a function of signal energy for different $\hbar\omega_b$ energies, 0.2 E_{Gap} and $\hbar\omega_b = \hbar\omega_a$ at 300 K and 20 K for a fixed excitation energy

As figure 48 shows, that with a fixed excitation beam, we actually see more gain at room temperature at a maximum value of 56 cm/GW with $\hbar\omega_b = 0.2\ E_{Gap}$. The maximum value at cryogenic temperatures is 35 cm/GW for $\hbar\omega_b = 0.2\ E_{Gap}$, which is nearly a factor of two less

than that at room temperature. This could help reduce some of the complexity of the experiment by eliminating the need for a cryostat.

Another issue for this experiment that has recently come to light is the possibility of amplified spontaneous emission (ASE) depleting our population inversion. Calculating ASE is a complex problem to solve because one has to account for a random distribution of emitters radiating in random directions, the pump geometry, surface shape, temperature and several other factors [60]. Barnes [60] developed an analytic solution for ASE in thin disk lasers from the rate equation

$$\frac{dN_2}{dt} = -\frac{N_2}{\tau_2} + R_2 \tag{5.0}$$

Where N_2 is the upper state population density, τ_2 is the radiative lifetime and R_2 is the pump rate per volume.

Barnes used several assumptions to develop a rate equation when ASE is not negligible. He first assumes that the radiation is from a point source in free space, which allows for the solid angle integrations to simply be replaced by 4π. Furthermore, he assumes that the emission spectrum has a Lorentzian linewidth and that the prorogation of emitted photons is independent of wavelength which is somewhat reasonable. The emission spectrum of a GaAs laser amplifier measured by Kosonocky [61] shown in figure 49 has a bandwidth of about 10 nm between 840 nm and 850 nm. Aspnes [47] shows that the index between 840 nm and 850 nm varies by 0.002 which leads to a critical angle difference of 0.01 degrees which can be assumed to be negligible.

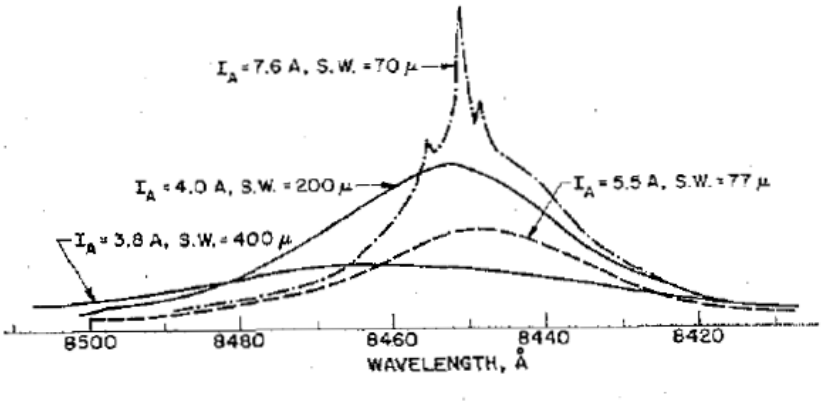

Figure 49 – Spontaneous emission spectrum from GaAs [61]

If the distribution of carriers is uniform, a rate equation can be developed when ASE is not negligible [60].

$$\frac{dN_2}{dt} \approx -\frac{N_2}{\tau_2} - \frac{\sigma_{ea} l_a}{\tau_2} {N_2}^2 + R_2 \tag{5.0}$$

Where σ_{ea} is the average emission cross section and l_a is the average path length of a spontaneously emitted photon. l_a is very much dependent on the pumping scheme and surface quality so it is recommended that this be measured to determine its value, however, it was reported by Peterson [62], that l_a should be on the order of the 50% of the pump spot size. From the differential equation, assuming $R_2 = 0$, the initial upper state population density as a function of time when ASE is not negligible can be calculated by [60]

$$N_2(t) = \frac{N_{2_o} e^{\frac{-t}{\tau_2}}}{1 + \sigma_{ea} l_a N_{2_o} \left(1 - e^{\frac{-t}{\tau_2}}\right)} \tag{5.1}$$

Applying this model to GaAs we assume $N_{2_o} = 5 \times 10^{18}\text{cm}^{-3}$, $\sigma_{ea}N_{2_o} = 14830\ \text{cm}^{-1}$ [47], $l_a = 150 \times 10^{-4}\text{cm}$ [62] and $\tau_2 =$ 70 ns [63] we see 80% reduction in the carrier density on the order of 1 ns so the gain would also decay by 80% since $\gamma \propto N_2(t)$

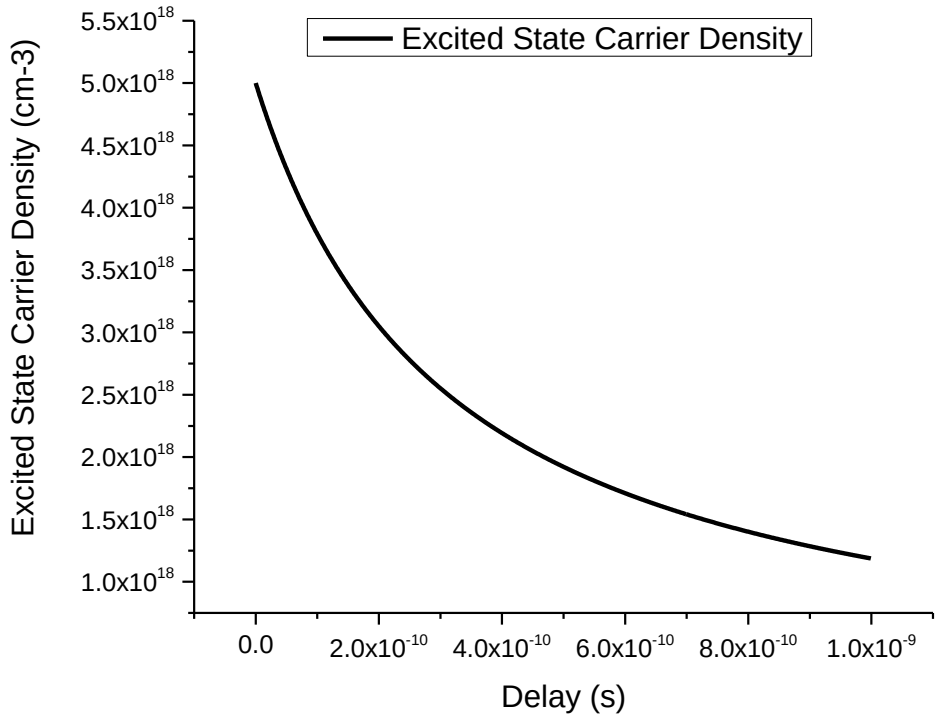

Figure 50 – Carrier population density in GaAs as a function of time if ASE is not negligible

In the experiments we probe our sample 200 ps after the peak of the excitation beam arrives, which based on the assumed l_a we lose 40% of our gain before the infrared pump and probe arrive. However, this model is not representative of our system at all and only meant to show that ASE could potentially be a problem. Therefore, another experiment that should be performed in the future would be to monitor the carrier lifetime as a function of the excitation energy [62]. If ASE is affecting the experiments, the carrier lifetime should decrease as the excitation energy is

increased. Should ASE be an issue, we could mitigate ASE's effect by making the spot size of the excitation beam smaller. This would reduce l_a thereby decreasing the rate of change of $N_2(t)$, and we could use a shorter excitation pulsewidth on the order of femtoseconds compared to picoseconds. Using a femtosecond excitation beam would allow us virtually instantaneously excite the carriers and should allow us to probe the sample with the infrared pump and probe before ASE became substantial.

We still trust we can see a reduction of 2PA due to excited carriers and maybe with a little luck, bleach the material and observe 2PE. If we manage to observe 2PE it would be useful to measure the magnitude of 2PE at varying degrees of non-degeneracy and as a function of the excitation energy and excitation wavelength. 2PE from semiconductors could one day yield unique opportunities in endeavors that require large ranges of tunability or quantum entangled photons such as quantum information and communication technologies [64].

APPENDIX: DETECTORS

Perhaps one of the most crucial parts when it comes to optics is the detection system since it is the primary measurement system. The detection system is largely dependent on the wavelengths in the experiment, as this will determine the type of diode that is used. However, there are other considerations that must be made including response time, linearity and noise when determining not only the photodiode material but the construction of that particular photodiode.

When selecting a photodiode, wavelength is the first consideration, as such in the following figures show various four common photodiode materials and the wavelength ranges where these diodes are sensitive.

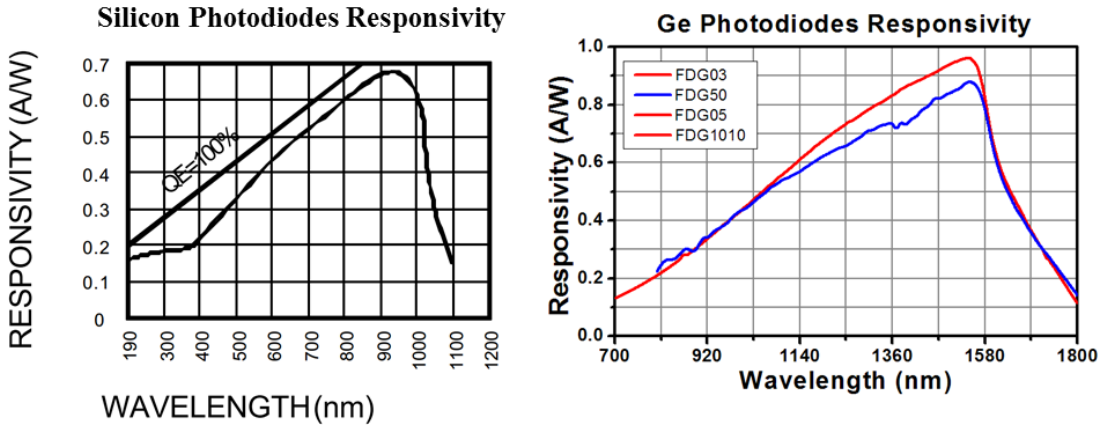

Figure 51 – Responsivity of a silicon photodiode [65] (left) and germanium diode [66] (right)

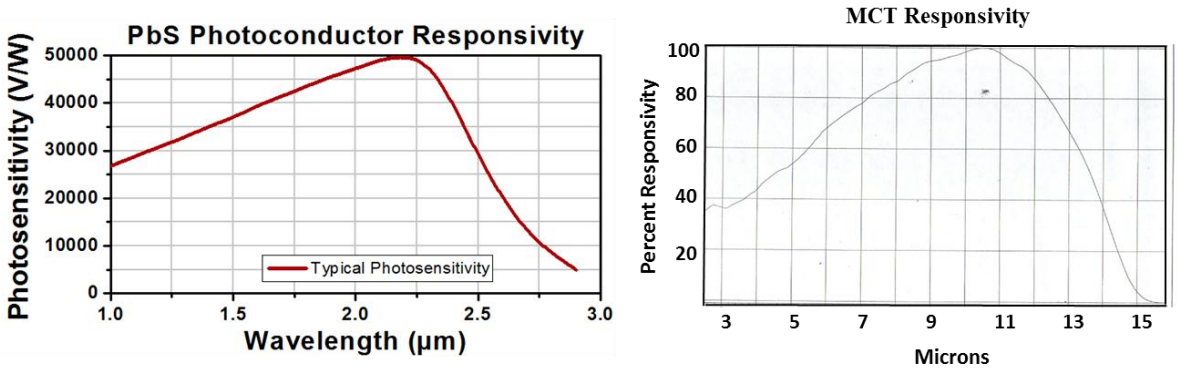

Figure 52 – Photodiode responsivity for lead sulfide [67] (left), MCT [68] (right)

As the graphs in figure 51 and 52 show, for wavelengths in the visible and UV, silicon is the best choice, for near infrared (IR) detection, lead sulfide and germanium are the best choices and for longer IR wavelengths, 3 – 15 µm, MCT's are the best. It is worthwhile to mention that just because two diodes have the same active material does not mean they will exhibit the same responsivity at a given wavelength. For instance, the germanium responsivity curve in figure 51 displays the responsivity for two different manufactured diodes and as we can see, the response between the two is different. Once a wavelength is chosen one must look at the system in which the diode will be operating to determine parameters such linearity, noise requirements and response time.

Linearity is an important aspect of detectors because in a variety of experiments, particularly those performed by the nonlinear optics (NLO) group at CREOL, it is the change of the signal that is measured as opposed to the magnitude of the signal. If the diode is linear we can calculate the energy change based on the change of voltage. The figure below shows the linear regime of a particular Hamatsu silicon photodiode output current as a function of incident radiation.

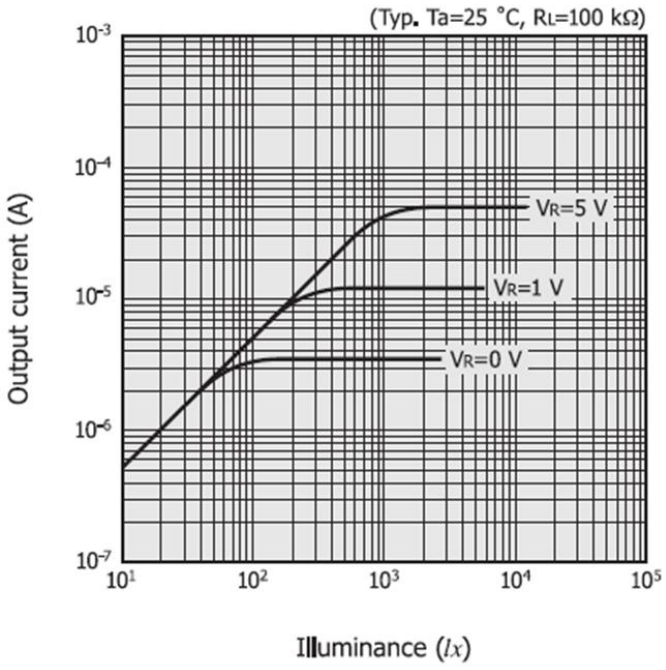

Figure 53 – Linear response of a silicon diode at various reverse bias voltages [69]

One will notice from figure 53, that the linear range increases depending on the amount of reverse bias voltage on the photodiode, in fact the linear range increases by an order of magnitude in incident radiation, from 10^2 to 10^3 with the application of a 5 V reverse bias. The application of a reverse bias voltage will increase the dynamic range of photodiodes, however, it will also increase the dark current of a photodiode and noise levels [69]. If a reverse bias needs to be applied to a diode in order to increase either the response time or dynamic range, it would be best to use a battery to supply the necessary voltage as opposed to a power supply. Power supplies will add unnecessary noise to a system particularly if the signals are small. We have recorded the addition of $\pm$ 40 mV of noise to small signals with the addition of a power supply for reverse biasing, whereas batteries add minimal noise. Another aspect that will affect linearity is the amplifier of the circuit, but this will be discussed later.

If low noise is a requirement of an experiment, which is usually the case for measuring small signals, but response time and a large linear range are not required, then it is best to avoid the application of a reverse bias voltage entirely. The NLO group in fact uses silicon photodiodes that are built specifically for running in photovoltaic mode, i.e. with no reverse bias, in order to reduce noise levels.

Response time, defined as the time it takes to change from 10% to 90% of the maximum output level [69], is perhaps the final major consideration required when determining the type of photodiode required for an experiment. In the case of the NLO group, due to our rather slow repetition rates of the laser sources, 1 kHz or 10 Hz, response time is not a concern for us since the longest diode response times are on the order of a few microseconds depending on the photodiode, which corresponds to greater than a 100 kHz repetition rates. However, for systems that have higher repetition rates the response time must begin to be taken into consideration since the photodiode will fail to respond if the pulse train from some source falls on the detector in a shorter time period than the response time of the diode. The reason being is diodes have a response time anywhere from several hundred picoseconds to hundreds of microseconds. The response time is determined, largely, by three factors: the RC time constant associated with the sum of the package capacitance, junction capacitance and the load resistance (t_1), the diffusion time of carriers generated outside the depletion region (t_2), and the carrier transit time in the depletion region (t_3) [69]. The response time, t_r, is

$$t_r = \sqrt{{t_1}^2 + {t_2}^2 + {t_3}^2}$$

The carrier transit time, t_3 is inversely proportional to the reverse bias voltage [70] which is why photodiodes that require a reverse biasing voltage, operate at higher speeds and consequently used for high speed detection. Other aspects that help improve the response time are smaller active areas and using PIN photodiodes as opposed to PN photodiodes.

However the total response time of a detector is also largely dependent on the amplifying circuit used to amplify the signal generated by the photodiode, since many amplifying systems are built to elongate the signal received from a photodiode based on the amplifier decay time. In the NLO group there are two types of general circuits that are used; one designed by Morgan Monroe and another by CREMAT Inc. Monroe's design is shown below.

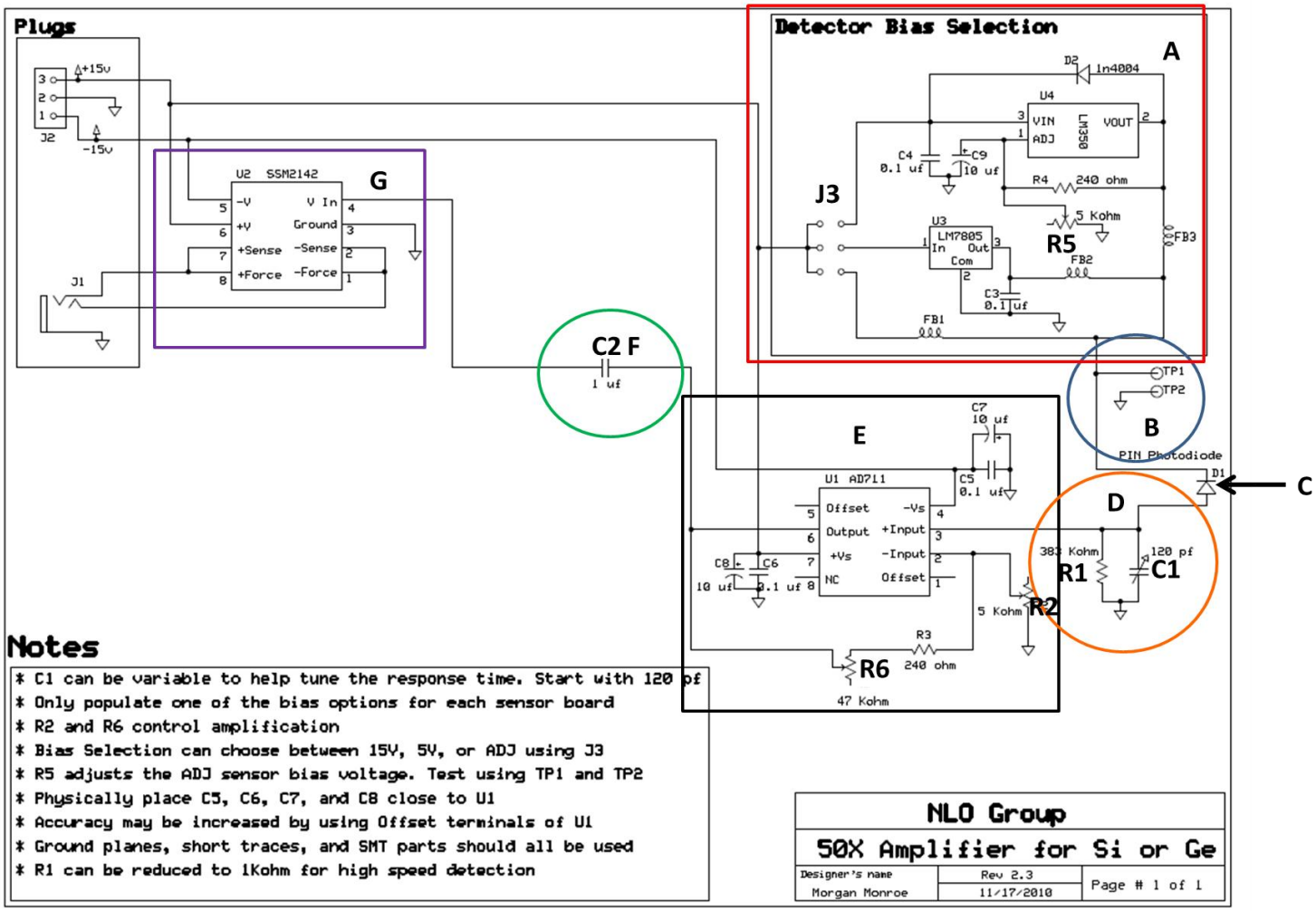

Figure 54-Detector circuit design by Morgan Monroe

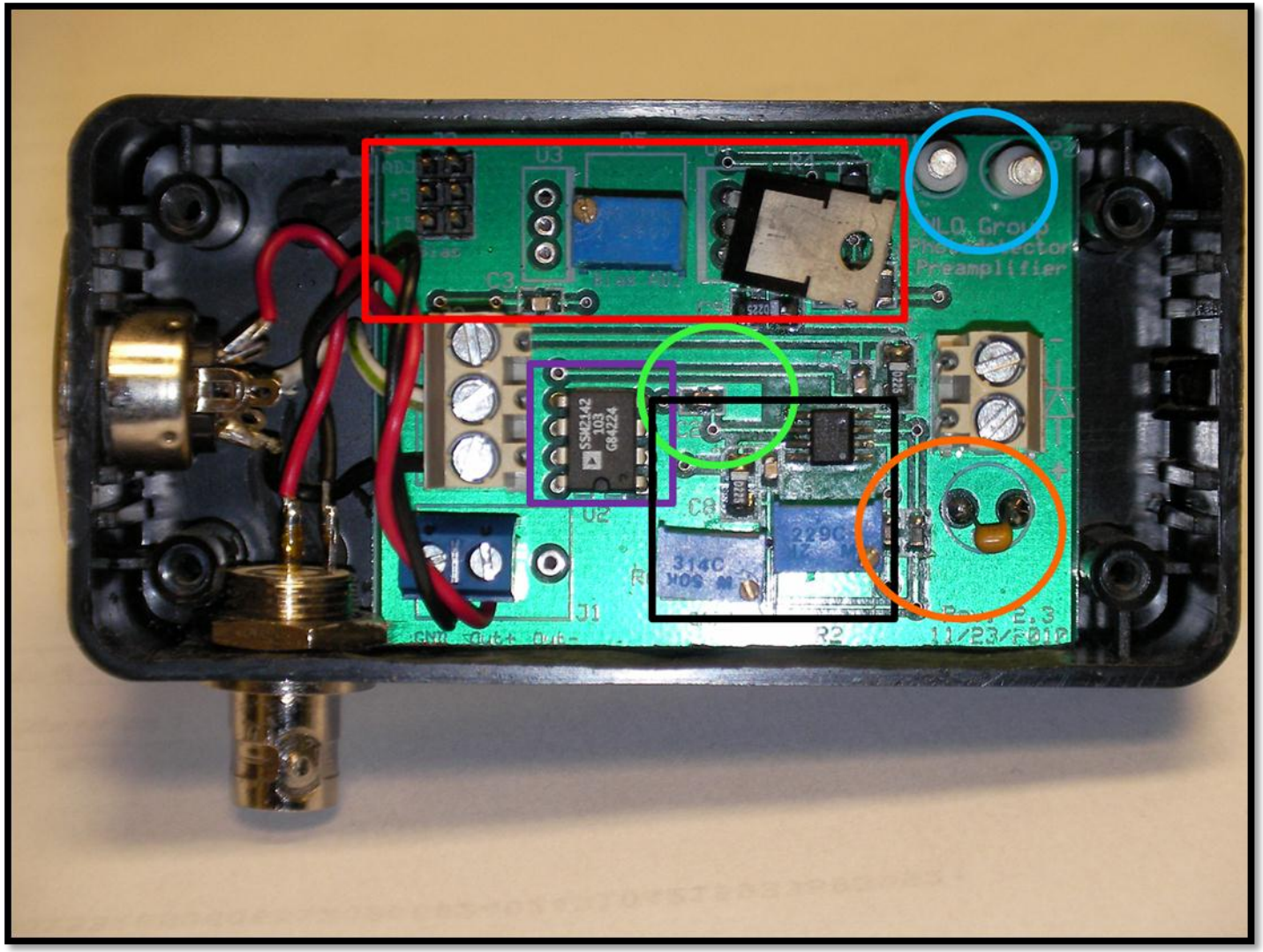

Figure 55- Detector circuit design by Morgan Monroe

To give a brief description of Morgan's circuit (figure 54 and 55) we begin with the section highlighted by the red square labeled A. This portion of the circuit applies a reverse bias voltage to the photodiode in part C. There are hard options such as 15 V or 5 V which can be selected using the bottom or middle junction respectively in J3, but there is also an option for an adjustable reverse bias if the top junction is selected. If the adjustable bias option is selected the potentiometer, R5, can be changed by using a screw driver thereby increasing or decreasing the reverse bias on the photodiode. In order to measure the reverse bias one must measure the voltage using a voltmeter across the test pins labeled TP1 and TP2 in part B, highlighted by the blue circle. The photodiode must be mounted so that the anode sees a positive voltage from the biasing circuit in part A to put it into reverse bias. Part D can be used to change the response time of the circuit. One can either increase or decrease the response time of the circuit by increasing or decreasing, respectively, the capacitance of C1. The resistor, R1, can also be changed; however, the amount of change is small in comparison to the amount of change the capacitor will induce. This is due to the fact the capacitor can be increased by six orders of magnitude easily whereas the resistance cannot be increased so dramatically without affecting other aspects of the circuit. The resistor R1 is more apt to be changed should there be a possible problem with the reverse bias voltage such as a high leakage current from the diode that could create a large voltage drop across R1. This aspect will be discussed in more depth later.

Part E, represented by the black square, is a transimpedance amplifier that converts the current generated by the photodiode into a voltage and amplifies said voltage. The amplification of this portion is controlled by potentiometers R2 and R6 through the use of a screw driver. Part F is the AC coupling capacitor, C2, which is used to block any DC components that are amplified by the

transimpedance amplifier. Lastly part G is a dual analog switch that is used to help pass the signal over a transmission line, in our case, BNC cable. This circuit design is still currently in use in the NLO group for specific photodiodes, particularly gallium nitride photodiodes, and it is also very similar to other old detectors in the NLO group.

Recently, however, we have begun transitioning from the above circuit design, to one manufactured by CREMAT Inc. The biggest reasons for this transition was primarily for ease of use and because we have few working detectors supporting Morgan Monroe's design. CREMAT offers four different charge amplifiers: CR-110, CR-111, CR-112 and CR-113. Each of the amplifiers performs virtually the same function with the only differences coming in the amount of gain associated with the amplifier and the length of the decay time. Beginning with the CR-110 and ending with the CR-113, each subsequent amplifier has about one tenth of the gain factor as the previous, so the gain of the CR-110 has a 1000 times more gain than the CR-113. The CR-113 and CR-112 amplifiers have shorter decay times at about 50 μs whereas the CR-110 and CR-111 have decay times of about 150 μs. One may wonder what would be the purpose of using a CR-113 or CR-112 since the gain is low. The answer depends on the signals that need to be amplified or if the decay time is important. For large signals it may be better to use lower gain so that when the signal is amplified it does not saturate the amplifier, which can happen if the input signal is too large. To get an idea of this saturation point for both a silicon and germanium photodiode, we measure the voltage as a function of input power. This is done by detecting a chopped continuous wave 632 nm or 950 nm using a silicon or germanium photodiode respectively and measuring the output peak to peak voltage, from the CREMAT

amplifier chip, on an oscilloscope. We measure the response from each of the different CREMAT amplifier chips for each photodiode as shown in the following results.

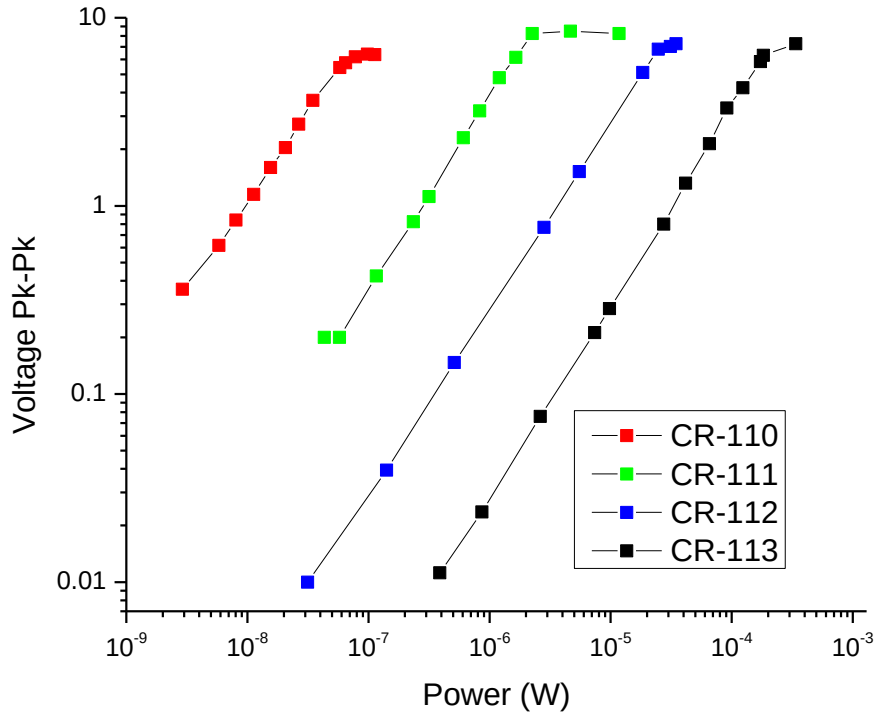

Figure 56 – Response of silicon photodiodes for each of the CREMAT charge amplifiers

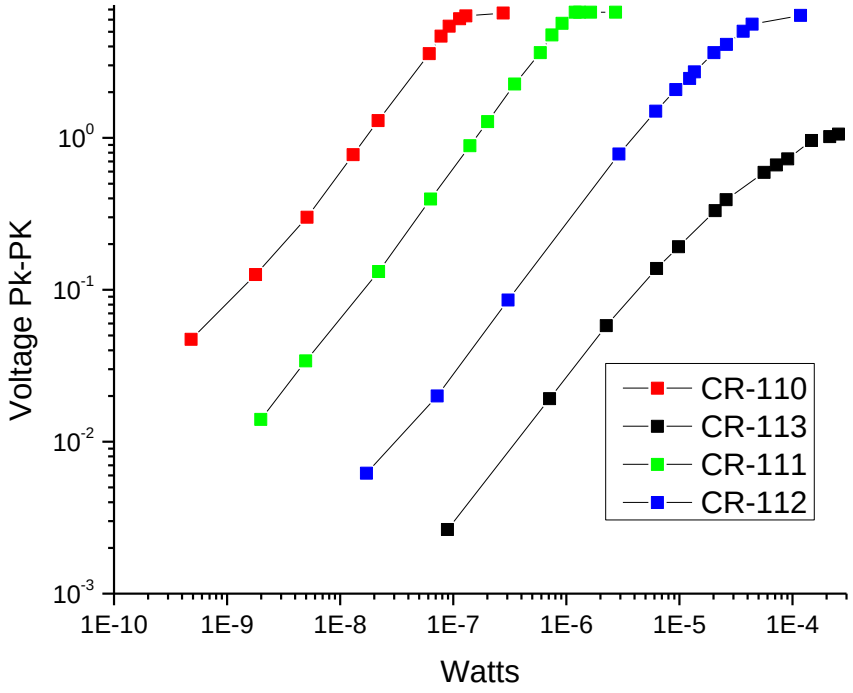

Figure 57 – Response of germanium photodiodes for each of the CREMAT charge amplifiers

The data displays the linearity and dynamic range of the silicon and germanium photodiodes for a given charge sensitive amplifier chip. In figure 56, the silicon diode shows sensitivity down to nW's with the CR-110 amplifier and nice linearity for each of the chips particularly around 1 volt. At about 8 V the amplifiers saturate, which is why the voltage stops increasing as the energy increases. In the case of the germanium photodiodes, figure 57, we are sensitive down to hundreds of pW's using the CR-110 amplifier. At low energies the diodes are not perfectly linear, however, the CR-110, CR-111 and CR-112 are linear from about a tenth of a volt to about 4 volts and saturate at about 7 volts, which is fine for most applications. The CR-113 amplifier is linear from about a couple thousandths of a volt to a few tenths of a volt after which the data

begins to curve, which we believe to be due to a combination of saturation of the amplifier as well as the diode. These voltages were measured using a Tektronix TDS 2022 digital oscilloscope and the power was measured using an Ophir D 300-UV-SH power meter. These curves, as mentioned previously, give us a nice dynamic range of operation for both the silicon and germanium photodiodes in the CREMAT detection system.

The last part of the CREMAT detection system is the CR-150 circuit board used to power and operate the charge sensitive amplifiers. The circuit is shown below.

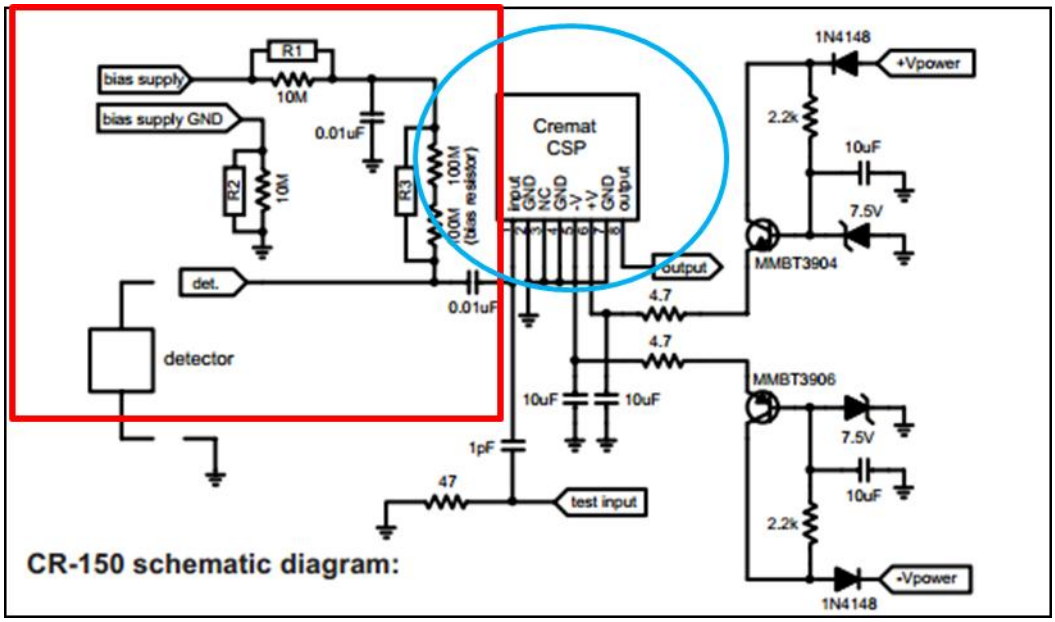

Figure 58-CR-150 evaluation board schematic [71], red is the biasing circuit and the blue circle refers to the charge sensitive amplifier

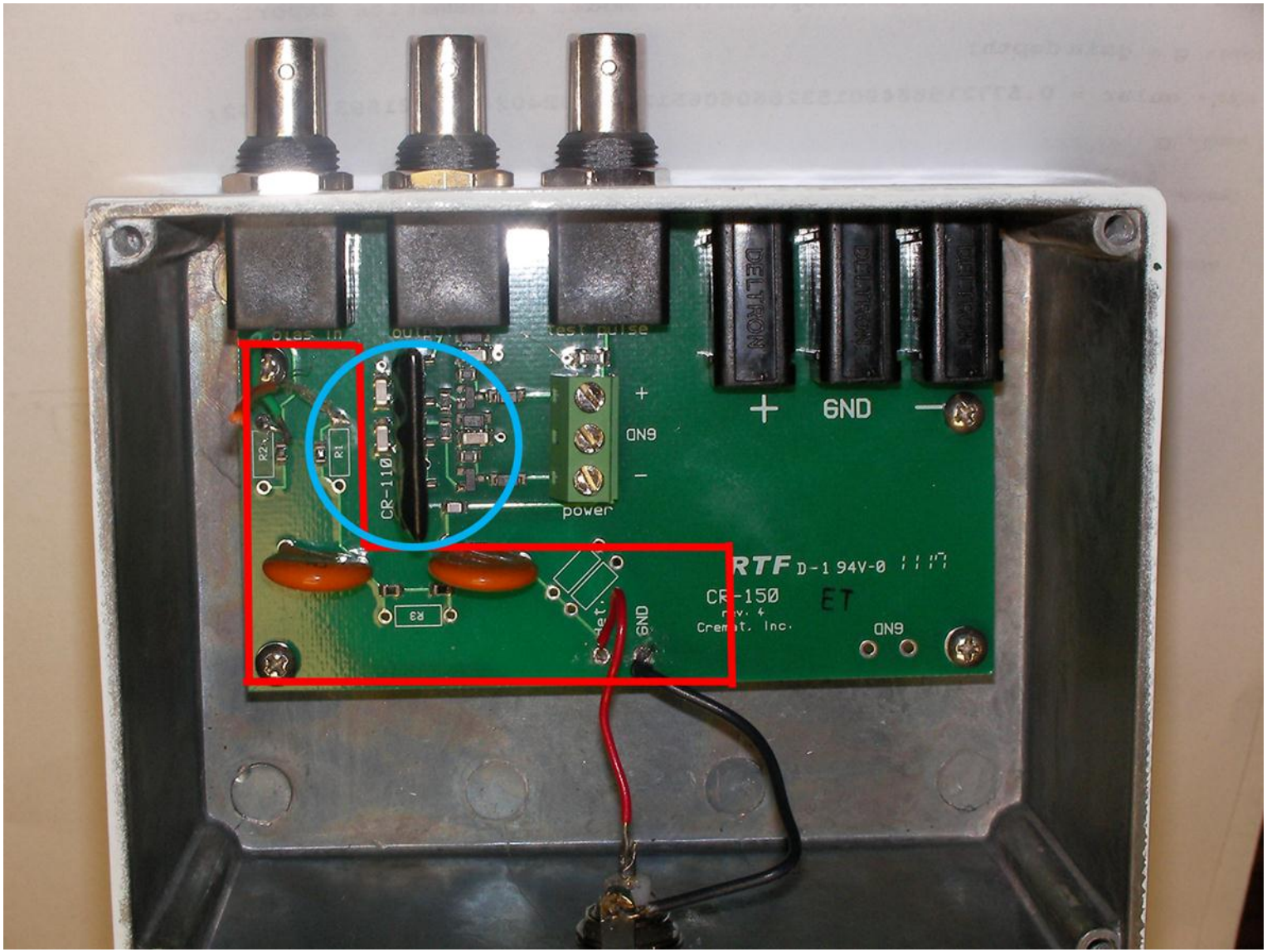

Figure 59-CR-150 evaluation board [71], red is the biasing circuit and the blue circle refers to the charge amplifier

The diagram shows the detector is AC coupled to the charge sensitive amplifier through a 0.01 μF capacitor. Once again this is to block out DC signals, particularly those from the biasing circuitry. Perhaps the important aspect to take from this diagram is the biasing circuit which is highlighted by the red box. The biasing circuit contains two 100 MΩ resistors and one 10 MΩ resistor leading to a total resistance of 210 MΩ [71]. In order to determine how to bias a photodiode in the CREMAT detection system, the reverse leakage current for the particular photodiode must be known and would be found on the photodiode spec sheet. Once the leakage current is known, one can calculate the voltage drop across the biasing resistors using Ohm's Law, $V = IR$ where V is the voltage, I is the current and R is the resistance. For example, if I apply a 15 volt reverse bias across a silicon photodiode with 200 pA of leakage current, the voltage drop across the biasing resistors is consequently 0.042 volts so the photodiode would "see" 14.958 volts which is completely acceptable. For most diodes this is the case, however, for avalanche photodiodes that can have 100 nA of leakage current, the voltage drop turns into 21 volts across the resistors which is unacceptable. In the case that the voltage drop is large, one can reduce the resistance of the biasing resistors by shunting them with the appropriate resistance. The appropriate shunting resistance can be determined from table 1 shown below.

Table 1 – Shunting resistances for various photodiode leakage currents [71]

Leakage Current Range	R1	R2	R3
0 to 10 nA	Open	Open	Open
10 nA to 30 nA	Open	Open	22 MΩ
30 nA to 100 nA	Open	Open	10 MΩ
100 nA to 300 nA	3.3 MΩ	3.3 MΩ	3.3 MΩ
300 nA to 1 µA	1 MΩ	1 MΩ	1 MΩ
1 µA to 3 µA	330 kΩ	330 kΩ	330 kΩ
3 µA to 10 µA	100 kΩ	100 kΩ	100 kΩ
10 µA to 30 µA	33 kΩ	33 kΩ	33 kΩ

Currently our CREMAT detectors do not have any shunting resistances since the leakage current for our silicon and germanium diodes are on the order of hundreds of picoamps so the voltage drop across the biasing resistors are negligible.

Our current CREMAT detection system, shown in figures 58 and 59, has the photodiodes connected directly to the circuit board. A hole is drilled into the outside of the box and a rubber grommet is used to stabilize the diode and prevent it from moving. However, the disadvantage to this is that each CREMAT box is specifically built for one diode.

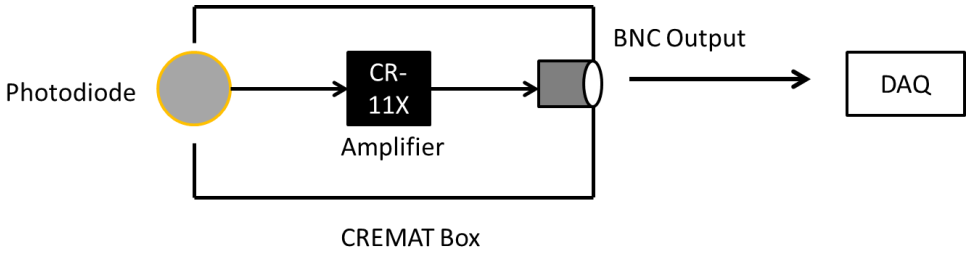

Figure 60 – Current CREMAT detection system, DAQ – Data Acquisition

However, we would like to change this setup by making a separate box to house the photodiode and connecting this new "diode box" to the CREMAT circuit via BNC cable. These CREMAT circuit boards and amplifiers could be used on any setup and be easily swapped out since they would not be housing the photodiode. These diode boxes would have a smaller foot print on the optical table and are far cheaper than buying individual CREMAT CR-150 circuit boards, amplifiers and boxes for each of the diodes. Figure 61 shows this new design.

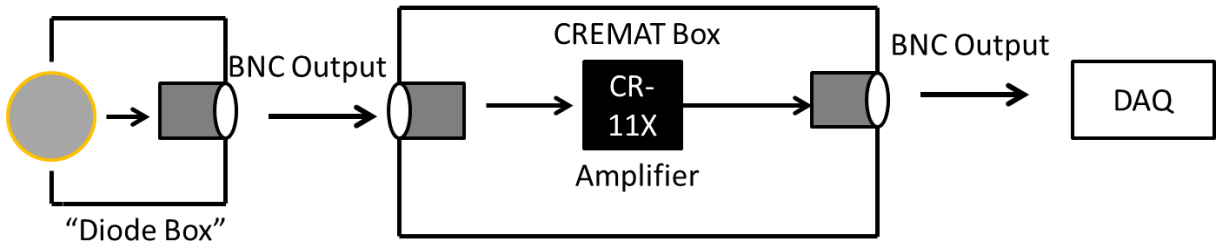

Figure 61 – New CREMAT detection system design, DAQ – Data Acquisition

There are two downsides however; the first and most pertinent is noise. With the addition of another BNC connector and cable, noise will be more likely to be picked up, and any noise that may be picked up could be amplified by the CR-11X amplifier chip. So to test to see if this design would induce substantially more noise we ran single arm Z-Scans and compared the noise between both detection systems. We also measured the noise of the new design based on a 3 ft

BNC cable and a 25 ft BNC cable with a BNC T-Junction between the diode box and the CREMAT amplifier. The noise results are shown in the following table.

Table 2 – Noise analysis of the current CREMAT system and the new CREMAT system

Run	Current CREMAT Design	New CREMAT Design /w 3ft BNC Cable	New Design /w 25ft BNC Cable and T-Junction
Run 1 (σ)	0.004413	0.004538	0.0179
Run 2 (σ)	0.003671	0.004872	0.008086
Run 3 (σ)	0.004251	0.003924	0.007726
Mean (σ)	0.004112	0.004445	0.01124

These measurements were made by taking the measured signal from a Z-Scan measurement and applying a high pass filter in Origin 8.6 to eliminate the 2PA signal. We then take the ratio of the mean and standard deviation of the data points which gives us the normalized deviation from the mean, σ, which in this case is defined as our noise. What these measurements show is that there is no real difference between the current system and the new system with a 3 ft BNC cable between the diode box and amplifier box. The three millionths difference in the average normalized deviation between each design is well within the measurement error. However, there is a change of about seven thousandths in the average deviation when a 25 ft BNC with a BNC T-Junction is added which is significant enough to be detrimental. Should this new system be implemented, care should be taken to make sure that the cable between the diode and the amplifier is not excessively long.

Another aspect that would need to be addressed for this new system to be realized would be to acquire zero bias germanium photodiodes. Since most of our silicon photodiodes require zero bias, building a system that could easily handle both germanium and silicon would require that the germaniums require no bias as well. If biasing is required then each detector would have to be made for silicon or germanium specifically since the reverse bias voltage between the two is usually different. Luckily, zero bias, low noise, high response germanium photodiodes exist and are made by GPD Optoelectronics Corp with the part number of GM8VHR. We will soon be acquiring a few of these to test and should the results be favorable this new design should soon be implemented.

REFERENCES

1. Göppert-Mayer, M., *Über Elementarakte mit zwei Quantensprüngen.* Annalen der Physik, 1931. **401**(3): p. 273-294.
2. Prokhorov, A.M., *Quantum Electronics.* Science, 1965. **149**: p. 828.
3. Gauthier, D., ed. *Two-Photon Lasers*. Progress in Optics, ed. E. Wolf. Vol. 45. 2003, Elsevier Science: Rochester. 411.
4. Stegeman, G.I. and R.H. Stolen, *Waveguides and fibers for nonlinear optics.* J. Opt. Soc. Am. B, 1989. **6**(4): p. 652-662.
5. Shensky, W., III, et al. *Broadband optical limiter using carbon-black suspensions in CS₂*. in *Lasers and Electro-Optics, 2002. CLEO '02. Technical Digest. Summaries of Papers Presented at the*. 2002.
6. Yariv, A. and W. Louisell, *5A2 - Theory of the optical parametric oscillator.* Quantum Electronics, IEEE Journal of, 1966. **2**(9): p. 418-424.
7. Giordmaine, J.A. and R.C. Miller, *Tunable Coherent Parametric Oscillation in LiNbO_{3} at Optical Frequencies.* Physical Review Letters, 1965. **14**(24): p. 973-976.
8. Breit, G. and H. Teller, *Metastability of Hydrogen and Helium Levels.* Astrophysical Journal, 1940. **91**: p. 215.

9. Maiman, T.H., *Stimulated Optical Radiation in Ruby.* Nature, 1960. **187**(4736): p. 493-494.

10. Sorokin, P.P. and N. Braslau, *Some theoretical aspects of a proposed double quantum stimulated emission device.* IBM J. Res. Dev., 1964. **8**(2): p. 177-181.

11. Kaminski, N., et al., *Numerical Study of Few-Cycle Pulses by Nonlinear Compression in Two-Photon Semiconductor Amplifiers.* Photonics Technology Letters, IEEE, 2009. **21**(3): p. 173-175.

12. Nevet, A., A. Hayat, and M. Orenstein, *Ultrafast pulse compression by semiconductor two-photon gain.* Opt. Lett., 2010. **35**(23): p. 3877-3879.

13. Hayat, A., et al., *Hyperentanglement source by intersubband two-photon emission from semiconductor quantum wells.* Opt. Lett., 2008. **33**(11): p. 1168-1170.

14. Gauthier, D.J., et al., *Realization of a continuous-wave, two-photon optical laser.* Physical Review Letters, 1992. **68**(4): p. 464-467.

15. Bräunlich, P. and P. Lambropoulos, *Detection of Singly-stimulated Two-Photon Emission from Metastable Deuterium Atoms.* Physical Review Letters, 1970. **25**(3): p. 135-138.

16. Bräunlich, P., R. Hall, and P. Lambropoulos, *Laser-Induced Quenching of Metastable Deuterium Atoms. Singly-stimulated Two-Photon Emission and Anti-Stokes Raman Scattering.* Physical Review A, 1972. **5**(3): p. 1013-1025.

17. Yatsiv, S., M. Rokni, and S. Barak, *Enhanced Two-Proton Emission.* Physical Review Letters, 1968. **20**(23): p. 1282-1284.

18. Ironside, C.N., *Two-photon gain semiconductor amplifier.* Quantum Electronics, IEEE Journal of, 1992. **28**(4): p. 842-847.

19. Page, T.L., *The continuous spectra of certain planetary nebulae : a photometric study.* Monthly Notices of the Royal Astronomical Society, 1936. **96**: p. 604.

20. Loy, M.M.T., *Two-Photon Adiabatic Inversion.* Physical Review Letters, 1978. **41**(7): p. 473-476.

21. Selby, J.E.A. and R.A. McClatchey, *Atmospheric Transmittance, 7-30 Micrometers: Attenuation of CO2 Laser Radiation.* NTIS, 1972: p. 77.

22. Gauthier, D., ed. *Two-Photon Lasers*. Progress in Optics, ed. E. Wolf. Vol. 45. 2003.

23. Pidgeon C. R. , W.B.S., Johnston A. M., Dempsey J., Miller A. , *Two-Photon Absorption in Zinc-Blende Semiconductors.* Physics Review Letters, 1979. **42**(26): p. 3.

24. Hayat, A., P. Ginzburg, and M. Orenstein, *Observation of two-photon emission from semiconductors.* Nat Photon, 2008. **2**(4): p. 238-241.

25. Nevet, A., A. Hayat, and M. Orenstein, *Measurement of Optical Two-Photon Gain in Electrically Pumped AlGaAs at Room Temperature.* Physical Review Letters, 2010. **104**(20): p. 207404.

26. Sheik-Bahae, M., et al., *Sensitive measurement of optical nonlinearities using a single beam.* Quantum Electronics, IEEE Journal of, 1990. **26**(4): p. 760-769.

27. Boyd, R.W., *Nonlinear Optics, Third Edition*. 2008: Academic Press. 640.

28. Bass, M., et al., *Optical Rectification.* Physical Review Letters, 1962. **9**(11): p. 446-448.

29. Franken, P.A., et al., *Generation of Optical Harmonics.* Physical Review Letters, 1961. **7**(4): p. 118-119.

30. Stegeman, G.I., *Nonlinear Optics Phenomena, Materials and Devices*. 1st ed, ed. G. Boreman. 2012, Hoboken: John Wiley & Sons. 472.

31. Hales, J.M., et al., *Resonant enhancement of two-photon absorption in substituted fluorene molecules.* The Journal of Chemical Physics, 2004. **121**(7): p. 3152-3160.

32. Sheik-Bahae, M., et al., *Dispersion of bound electron nonlinear refraction in solids.* Quantum Electronics, IEEE Journal of, 1991. **27**(6): p. 1296-1309.

33. Fishman, D.A., et al., *Sensitive mid-infrared detection in wide-bandgap semiconductors using extreme non-degenerate two-photon absorption.* Nat Photon, 2011. **5**(9): p. 561-565.

34. Hutchings, D.C. and E.W.V. Stryland, *Nondegenerate two-photon absorption in zinc blende semiconductors.* J. Opt. Soc. Am. B, 1992. **9**(11): p. 2065-2074.

35. Wherrett, B.S., *Scaling rules for multiphoton interband absorption in semiconductors.* J. Opt. Soc. Am. B, 1984. **1**(1): p. 67-72.

36. Cirloganu, C.M., et al., *Extremely nondegenerate two-photon absorption in direct-gap semiconductors [Invited]*. Opt. Express, 2011. **19**(23): p. 22951-22960.

37. Pattanaik, H., et al. *Two-photon emission in direct-gap semiconductors*. 2011: Optical Society of America.

38. Fox, M., *Optical Properties of Solids*. 2nd ed. 2010, Great Britain: Oxford University Press. 15.

39. Krishnamurthy, S., et al., *Temperature- and wavelength-dependent two-photon and free-carrier absorption in GaAs, InP, GaInAs, and InAsP.* Journal of Applied Physics, 2011. **109**(3): p. 033102-9.

40. Peceli, D., *Soon to be published.* 2013.

41. Ruzicka, B.A., et al., *Spatially resolved pump-probe study of single-layer graphene produced by chemical vapor deposition [Invited]*. Opt. Mater. Express, 2012. **2**(6): p. 708-716.

42. Cho, G.C., W. Kütt, and H. Kurz, *Subpicosecond time-resolved coherent-phonon oscillations in GaAs.* Physical Review Letters, 1990. **65**(6): p. 764-766.

43. Negres, R.A., et al., *Experiment and analysis of two-photon absorption spectroscopy using a white-light continuum probe.* Quantum Electronics, IEEE Journal of, 2002. **38**(9): p. 1205-1216.

44. Tamura, K., et al., *Technique for obtaining high-energy ultrashort pulses from an additive-pulse mode-locked erbium-doped fiber ring laser.* Opt. Lett., 1994. **19**(1): p. 46-48.

45. Maine, P., et al., *Generation of ultrahigh peak power pulses by chirped pulse amplification.* Quantum Electronics, IEEE Journal of, 1988. **24**(2): p. 398-403.

46. Clark-MXR, I., *CPA 2010 Users Manual Version 1.4*. 2001, Clark-MXR, Inc.

47. Aspnes, D.E. and A.A. Studna, *Dielectric functions and optical parameters of Si, Ge, GaP, GaAs, GaSb, InP, InAs, and InSb from 1.5 to 6.0 eV.* Physical Review B, 1983. **27**(2): p. 985-1009.

48. Gannon, J.J. and C.J. Nuese, *A Chemical Etchant for the Selective Removal of GaAs Through SiO2 Masks.* Journal of The Electrochemical Society, 1974. **121**(9): p. 1215-1219.

49. Uenishi, Y., H. Tanaka, and H. Ukita, *Characterization of AlGaAs microstructure fabricated by AlGaAs/GaAs micromachining.* Electron Devices, IEEE Transactions on, 1994. **41**(10): p. 1778-1783.

50. Norland Products, I. *Norland Optical Adhesive 81*. [cited 2012 December 16th]; Available from: http://www.norlandproducts.com/adhesives/noa%2081.html.

51. Thorlabs, I. *Sapphire Windows*. 2013 Jun 29, 2012 [cited 2013 Feb, 03]; Available from: http://www.thorlabs.com/newgrouppage9.cfm?objectgroup_id=3982.

52. Sturge, M.D., *Optical Absorption of Gallium Arsenide between 0.6 and 2.75 eV*. Physical Review, 1962. **127**(3): p. 768-773.

53. O'Connell, D., et al., *The two-photon decay of metastable atomic hydrogen.* Journal of Physics B: Atomic and Molecular Physics, 1975. **8**(11): p. L214.

54. Pfister, O., et al., *Two-photon stimulated emission in laser-driven alkali-metal atoms using an orthogonal pump-probe geometry.* Physical Review A, 1999. **60**(6): p. R4249-R4252.

55. Zhu, Y., et al., *Observation of a two-photon gain feature in the strong-probe absorption spectrum of driven two-level atoms.* Physical Review Letters, 1990. **65**(10): p. 1200-1203.

56. Adachi, S., *GaAs, AlAs, and Al[sub x]Ga[sub 1 - x]As@B: Material parameters for use in research and device applications.* Journal of Applied Physics, 1985. **58**(3): p. R1-R29.

57. Sadao, A., ed. *The Handbook on Optical Constants of Semiconductors*. Sadao, Adachi, ed. A.A. Said. 2012, World Scientific Publishing Co: Toh Tuck Link. 619.

58. Aspnes, D.E., *GaAs lower conduction-band minima: Ordering and properties.* Physical Review B, 1976. **14**(12): p. 5331-5343.

59. Mayer, E.J., et al., *Infrared absorption spectra of photoexcited holes in undoped GaAs.* Physical Review B, 1992. **46**(3): p. 1878-1881.

60. Barnes, N.P. and B.M. Walsh, *Amplified spontaneous emission-application to Nd: YAG lasers.* Quantum Electronics, IEEE Journal of, 1999. **35**(1): p. 101-109.

61. Kosonocky, W.F. and R.H. Cornely, *GaAs laser amplifiers.* Quantum Electronics, IEEE Journal of, 1968. **4**(4): p. 125-131.

62. Peterson, P., et al., *ASE in thin disk lasers: theory and experiment.* Opt. Express, 2011. **19**(25): p. 25672-25684.

63. Varshni, Y.P., *Band-to-Band Radiative Recombination in Groups IV, VI, and III-V Semiconductors (I).* physica status solidi (b), 1967. **19**(2): p. 459-514.

64. Edamatsu, K., *Entangled Photons: Generation, Observation, and Characterization.* Japanese Journal of Applied Physics, 2007. **46**: p. 7175.

65. Photonic Detectors, I., *Silicon Photodiode, U.V. Enhanced Photovoltaic*, P.D. Inc., Editor. p. 1.

66. Thorlabs, I. *Photodiodes*. 2013 Feb 6, 2013 [cited 2013 February 16th]; Available from: http://www.thorlabs.us/NewGroupPage9.cfm?ObjectGroup_ID=285.

67. Thorlabs, I. *IR Photoconductive Detectors*. 2013 January 25, 2013 [cited 2013 February 16th]; Available from: http://www.thorlabs.us/NewGroupPage9.cfm?ObjectGroup_ID=6479.

68. Infrared Associates, I., *Detector Test Report*, I.A. Inc., Editor. 2005: Stuart.

69. Hamatasu, *Si Photodiodes*, Hamatsu, Editor. 2013. p. 1-45.

70. Bhattacharya, P., *Semiconductor Optoelectronic Devices*. 2nd ed, ed. R. Kernan. 1997, Upper Saddle River: Prentice-Hall Inc. 614.

71. CREMAT, I., *CR-150 Evaluation Board: Application Guide*. 2013: West Newton. p. 1-2.